NUMERICAL SIMULATION OF COMPLEX SOFT MATTER SYSTEMS

by
ROOZBEH SAGHATCHI

Submitted to the Graduate Faculty of Engineering and Natural Sciences
in partial fulfilment of
the requirements for the degree of Doctor of Philosophy

Sabancı University
July 2022

ABSTRACT

NUMERICAL SIMULATION OF COMPLEX SOFT MATTER SYSTEMS

ROOZBEH SAGHATCHI

MANUFACTURING ENGINEERING Ph.D DISSERTATION, JULY 2022

Dissertation Supervisor: Prof. Mehmet Yildiz

Keywords: soft matter, emulsion, active nematics, smoothed particle hydrodynamics, finite volume

Soft matters are the branch of materials that can be deformed or structurally altered under mechanical stress. These materials have contributed to many engineering applications, including microfluidics, 3D printing, and tissue engineering, among others. Of particular interest, two essential and highly desirable in many applications are being considered, including emulsions and active matters. Emulsions consist of a dispersed fluid suspended in an ambient fluid leading to the multiphase system. The water-oil emulsion is one of the well-known examples of these systems, which can be either a single emulsion (W/O or O/W) or the double emulsion (W/O/W or O/W/O), which are the indispensable parts of the microfluidic systems. Active matters describe systems, such as cellular tissue or bacterial suspensions that actively consume their internal or surrounding energy and convert it into motion leading to the collective chaotic motion known as active turbulence.

Using numerical simulations based on two different mesh-free and mesh-based schemes, namely smoothed particle hydrodynamics and finite volume methods, we investigate the hydrodynamics of these complex systems, allowing us to control these systems and gain a better understanding of their behavior. First, an electrohydrodynamics simulation of the emulsion is performed. The confinement effects are investigated by placing a single emulsion in a highly confined domain and applying an external electric field. It is shown that the deformation is highly dependent on the ratios of electrical permittivity, electrical conductivity, and confinement ratio. Effects of combined shear and electric forces on the double emulsion are also studied. It is shown that the deformation and orientation angle of droplets are highly dependent on the capillary and electrical capillary numbers, and core to shell radius ratio. It is demonstrated that in some systems, a breakup occurs, which can be circumvented by changing the capillary and electrical capillary numbers as well as the core to shell droplet radius ratio.

Next, the active nematic is simulated by using the continuum model for the nematodynamic equation. Flow behavior, nematic ordering, topological defects, vorticity correlation, and spectrum of the kinetic energy are calculated and discussed in detail. Furthermore, the active nematics' mixing behavior is calculated and described qualitatively. The effects of two important parameters, namely, activity and elastic constant, are investigated. It is shown that the activity intensifies the chaotic nature of the active nematic by increasing the pathline and mixing efficiency while the elastic constant behaves oppositely. Additionally, the Impact of fluid inertia on the collective pattern formation in active nematics is investigated. It is shown that an incremental increase in inertial effects results in gradual melting of nematic order with an increase in topological defect density before a discontinuous transition to a vortex-condensate state. The emergent vortex-condensate state at low enough viscosities coincides with nematic order condensation within the giant vortices and the drop in the density of topological defects. It is further shown that the flow field around topological defects is substantially affected by inertial effects. Moreover, the strong dependence of the kinetic energy spectrum on the inertial effects is demonstrated, which recovers the Kolmogorov scaling within the vortex-condensate phase, but no evidence of universal scaling at higher viscosities is found. Finally, the vibrational motion of a cantilever beam placed in active nematics is investigated. It is indicated that the small-scale vortices are the primary mechanism for the energy transfer between the fluid and beam, thereby imposing the oscillatory motion. It is also shown that the intensification of the activity increases peak frequency, and there is a linear correlation between the peak frequency and activity. The reciprocal relationship between viscosity and peak frequency is demonstrated as well.

ÖZET

KOMPLEKS YUMUŞAK MADDE SISTEMLERININ SAYISAL SIMÜLASYONU

ROOZBEH SAGHATCHI

ÜRETIM MÜHENDISLIĞI DOKTORA TEZİ, MAYIS 2022

Tez Danışmanı: Prof. Dr. MEHMET YILDIZ

Anahtar Kelimeler: yumuşak madde, emülsiyon, aktif nematik, interpolasyonlu parçacık hidrodinamiği, sonlu hacimler

Yumuşak maddeler, mekanik stres altında deforme olabilen veya yapısal olarak değişebilen malzemelerin dalıdır. Bu malzemeler, mikroakışkanlar, 3D baskı ve doku mühendisliği dahil olmak üzere çeşitli mühendislik uygulamalarına katkıda bulunmaktadır. Emülsiyonlar ve aktif maddeler, birçok uygulamada karşılaşılan ve yumuşak maddeler alanının oldukça ilgi gören iki kategorisidir. Emülsiyonlar, bir ortam sıvısında süspanse edilen dağılmış bir sıvıdan oluşan çok fazlı sistemlerdir. Suyağ emülsiyonu, bu sistemlerin en iyi bilinen örneklerinden biridir ve mikroakışkan sistemlerin vazgeçilmez bileşenleri olan tek bir emülsiyon (S/Y veya Y/S) veya çift emülsiyon (S/Y/S veya Y/S/Y) şeklinde meydana gelebilmektedir.Aktif maddeler, iç enerji veya çevrelerindeki enerjiyi aktif olarak tüketerek, sonucunda aktif türbülans olarak bilinen toplu kaotik harekete dönüştüren hücresel doku veya bakteri süspansiyonları gibi sistemlerdir.

Bu çalışma, interpolasyonlu parçacık hidrodinamiği ve sonlu hacimler yöntemleri olmak üzere, ağsız ve ağ tabanlı iki farklı sayısal yöntem kullanılarak gerçekleştirilen simülasyonlar aracılığıyla, söz konusu karmaşık sistemlerin hidrodinamiğini araştırarak bu sistemlerin kontrol edilmesine ve davranışlarına dair kavrayışımızı artırmaya olanak sağlamaktadır.Bu doğrultuda ilk olarak, emülsiyonun bir elektrohidrodinamik simülasyonu gerçekleştirilmiştir. Son derece sınırlı bir alana tek bir emülsiyon yerleştirilerek ve bir dış elektrik alanı uygulanarak sınırlama etkileri araştırılmıştır. Deformasyonun büyük ölçüde elektriksel geçirgenlik, elektriksel iletkenlik ve hapsetme oranı oranlarına bağlı olduğu gösterilmiştir. Ayrıca, çift emülsiyon üzerindeki kombine kesme ve elektrik kuvvetlerinin etkileri de incelenmiştir.

Damlacıkların deformasyon ve yönlenme açısının, kılcal ve elektrik kılcal sayılarına ve çekirdek-kabuk yarıçap oranına büyük ölçüde bağlı olduğu gösterilmiştir. Bazı sistemlerde, kılcal ve elektrik kılcal sayılarının yanı sıra çekirdek-kabuk damlacık yarıçapı oranının değiştirilmesiyle önlenebilecek bir kırılma meydana geldiği gösterilmiştir.

Daha sonra, nematodinamik denklem için süreklilik modeli kullanılarak aktif nematik simüle edilmiştir. Akış davranışı, nematik düzen, topolojik kusurlar, girdap korelasyonu ve kinetik enerji spektrumu hesaplanmış ve ayrıntılı olarak tartışılmıştır. Ayrıca, aktif nematiklerin karışma davranışı hesaplanmış ve niteliksel olarak tanımlanmıştır. İki önemli parametre olan aktivite ve elastik sabitin etkileri incelenmiştir. Aktivitenin, katedilen mesafe ve karıştırma verimini artırarak aktif nematiğin kaotik yapısını yoğunlaştırırken, elastik sabitin zıt şekilde davrandığı gösterilmiştir. Ayrıca, sıvı ataletinin aktif nematikte kolektif model oluşumu üzerindeki etkisi araştırılmıştır. Eylemsizlik etkilerindeki kademeli bir artışın, bir girdap-yoğuşma durumuna süreksiz bir geçişten önce topolojik kusur yoğunluğunda bir artışla nematik düzenin kademeli olarak erimesine neden olduğu gösterilmiştir. Yeterince düşük viskozitelerde ortaya çıkan girdap-yoğuşma durumu, dev girdaplar içindeki nematik düzen yoğunlaşması ve topolojik kusurların yoğunluğundaki düşüş ile çakışmaktadır. Bununla birlikte, topolojik kusurların etrafındaki akış alanının atalet etkilerinden önemli ölçüde etkilendiği gösterilmiştir. Ayrıca, kinetik enerji spektrumunun atalet etkilerine güçlü bağımlılığı gösterilmiştir. Bu da girdap-yoğunlaştırma fazı içinde Kolmogorov ölçeklemesini geri getirmekte, fakat daha yüksek viskozitelerde evrensel ölçeklemeye kanıt sağlamamaktadır. Son olarak, aktif nematik içine yerleştirilmiş bir konsol kirişin titreşim hareketi incelenmiştir. Küçük ölçekli girdapların, akışkan ve kiriş arasındaki enerji transferi için birincil mekanizma olduğu, dolayısıyla salınım hareketinin sorumlusu olduğu gösterilmiştir. Ayrıca, aktivitenin yoğunlaşmasının tepe frekansını arttırdığı ve tepe frekansı ile aktivite arasında doğrusal bir korelasyon olduğu gösterilmiştir. Viskozite ve tepe frekansı arasındaki karşılıklı ilişki de gösterilmiştir.

ACKNOWLEDGEMENTS

In the first place, I would like to thank my supervisor Professor Mehmet Yildiz for welcoming me into his research group, and for his continued support, guidance, and constructive criticism during all this time. I am grateful for all the opportunities he offered me, which allowed me to explore and develop my own research interests and for allowing me to grow as a researcher.

Very special thanks are also due to Dr. Amin Doostmohammadi for his vital support, invaluable insights, and countless ideas. I am also indebted to Dr. Deniz Can Kolukisa, Dr. Murat Ozbulut, and Dr. Amin Rahmat for their support and helpful discussions on the SPH and CUDA.

Furthermore, I would like to acknowledge Sabanci University and SU-IMC team for providing an excellent research environment and financial support.

My thanks also go to friends in Sabanci and SU-IMC, and my family for their support and motivation.

Last but not least, I would like to thank my lovely wife and my son for their patience, emotional support, and passionate love.

To my wife Golchehreh
and my son Arman

TABLE OF CONTENTS

Appendix A

Appendix B

LIST OF TABLES

LIST OF FIGURES

LIST OF ABBREVIATONS

AMF	Average Moving Filter	108
APD	Artificial Particle Displacement	31
ATP	Adenosine triphosphate	24, 103, 113
BD	Blended Differencing	34
CD	Central Differencing	34
CFD	Computational Fluid Dynamics	7, 9
CFL	Courant-Friedrichs-Lewy	30, 34, 56
CPU	Central Processing Unit	9, 72
CSF	Continuum Surface Force	12
CUDA	Compute Unified Device Architecture	xiii, xvii, 10, 72, 73, 75, 76, 113
EHD	Electrohydrodynamics	2, 3, 4, 10
FDM	Finite Difference Method	8
FEM	Finite Element Method	3
FFT	Fast Fourier Transform	107, 108, 113
FSI	Fluid-Structure Interaction	8, 112, 114, 118
FVM	Finite Volume Method	xi, xv, 3, 7, 8, 25, 32, 33, 118
GPU	Graphics Processing Unit	9, 72, 73, 75, 76, 114
HPC	High Performance Computing	7, 9
ISPH	Incompressible Smoothed Particle Hydrodynamics	29, 30, 37, 53
LBM	Lattice Boltzmann Method	3, 71

LOC Lab-on-a-Chip 2, 4

MPI Message Passing Interface 9

MT Microtubule 6

OpenCL Open Computing Language 10

OpenFOAM Open source Field Operation And Manipulation . xvi, xvii, xviii, 8, 9, 10, 32, 34, 35, 56, 57, 75, 76, 80, 81, 91, 113, 118

OpenMP Open Multi-Processing 9, 113

PDE Partial Differential Equation 8, 32, 33

SPH Smoothed Particle Hydrodynamics . . xiv, xv, xvi, xvii, xviii, 7, 8, 10, 25, 26, 27, 28, 29, 30, 32, 38, 43, 44, 48, 56, 57, 71, 72, 75, 76, 77, 80, 81, 84, 113, 114

UD Upwind Differencing 34

VoF Volume of Fluid . . . . xi, 32, 35

WAM Weighted Arithmetic Mean 29

WCSPH Weakly Compressible Smoothed Particle Hydrodynamics 29, 30

WHM Weighted Harmonic Mean 28

1. INTRODUCTION

1.1 Soft matter systems

Soft matters are the branch of materials that can be deformed or structurally altered under mechanical stress. Liquids, foams, gels, emulsions, and liquid crystals, and biological matters are examples of these materials. Soft matters have made an outstanding contribution to many engineering applications, including microfluidics (Bartolo & Aarts, 2012), 3D printing (Chen, Tan, Bin Juhari, Shi, Cheng, Chan & Song, 2020), tissue engineering (Dhariwala, Hunt & Boland, 2004), robotics (Majidi, 2019), amongst others. Of particular interest, two essential and highly desirable in many applications are being considered, including emulsions and active matters.

1.1.1 Emulsions

Emulsions are one of the important types of soft matter, which is the mixture of two or more immiscible fluids forming a multiphase system. These systems consist of a dispersed fluid suspended in an ambient fluid. Water- oil emulsion is a famous example of a single emulsion system where oil droplets are dispersed in the water (Fig. 1.1-a). In some cases, more than two fluids participate in the dispersed phase such that one fluid surrounds the other. In such conditions, one emulsion has core and shell fluids both dispersed in the third ambient fluid, which is known as double emulsion (Fig. 1.1-b). The emulsion properties will be very different from those of the component liquids, making it desirable in a vast number of applications, such as wastewater treatment (Raghuraman, Tirmizi & Wiencek, 1994), food production (Paximada, Howarth & Dubey, 2021), cosmetic industry (Tarnowska,

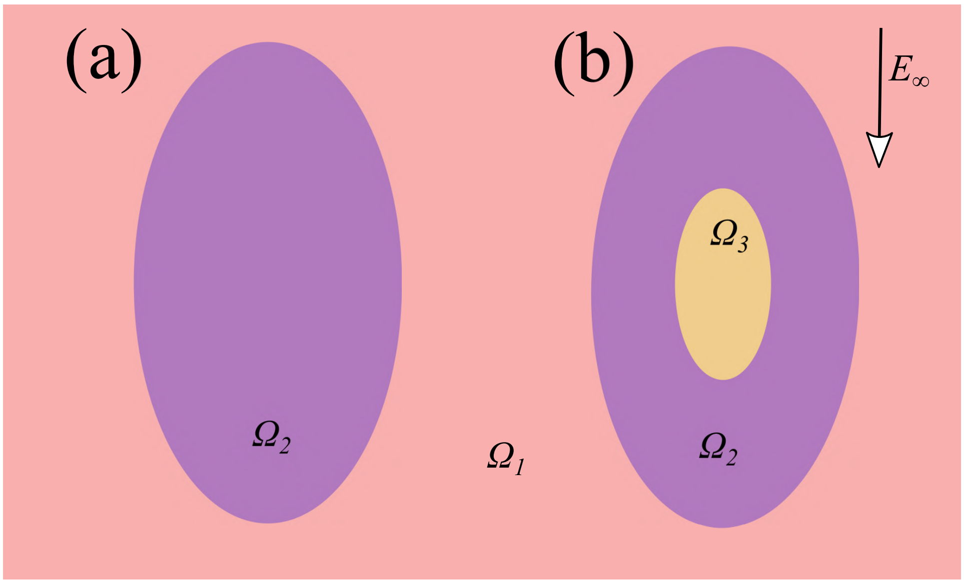

Figure 1.1 **Schematic representation of an emulsion deformed under the effect of external electric field.** (a) single emulsion. (b) double emulsion.

Briançon, Resende de Azevedo, Chevalier, Arquier, Barratier & Bolzinger, 2020), drug delivery (Pontrelli, Carr, Tiribocchi & Succi, 2020), and LOC[1] (Zanini, Zaltron, Turato, Zamboni & Sada, 2022).

One of the essential concerns of emulsions, particularly in microfluidic systems, is their manipulation and control. For instance, these process are necessary for droplet transportation and droplet sampling in biological LOCs (Feng, Shirani & Inglis, 2019) and mixing (Lee, Chang, Wang & Fu, 2011). Various manipulation methods can be utilized in microfluidics, including hydrodynamic manipulation, EHD[2] manipulation, thermocapillary, magnetic actuation, and acoustic radiation (Yang, Xu & Wang, 2010). In hydrodynamic manipulation, an external hydrodynamic force is exerted on the system. Consequently, this force creates stress on the interface, thus reshaping/moving the droplet in the desired direction. This hydrodynamic stress can be supplied by imposing pressure or shear force (Hudson, 2010), or designing a specific channel geometry (T-junction (Pang, Zhou, Wang, Lei, Ren, Li, Wang & Liu, 2020) and Flow-focusing geometry (Funfschilling, Debas, Li & Mason, 2009), for example).

In this thesis, the main focus will be on the EHD deformation of the emulsions. Since EHD-based control is relatively complex compared to the hydrodynamic means, the following section will mainly introduce this method.

---

[1] Lab-on-a-Chip

[2] Electrohydrodynamics

1.1.1.1 Electrohydrodynamics

EHD is the science of studying the electrically charged fluid under the applied high voltage. The applied electric field creates pressure in dielectric media, leading to the fluid flow in the physical domain. Therefore, EHD has become a widely used method to manipulate emulsions and droplets in various applications such as 3D printing (Mohammadi, Movahhedy & Khodaygan, 2019), electrocoalescence (Xia, 2019), and bioengineering (Altun, Ekren, Kuruca & Gunduz, 2019).

Investigation of EHD effect on the suspended droplet has a long history. Initially, a very rough assumption was made for the emulsion, where the droplet and the medium fluids were considered either perfect dielectrics or perfect conductors. However, such an assumption resulted in a unidirectional elongation of the droplet. Concretely, the droplet was deformed in the direction of the applied electric field only, which is known as prolate deformation (Taylor, 1964). Later, Allan et al. (1962) showed that it is possible for the droplet to deform in the perpendicular direction to the applied electric field (oblate elongation). This critical observation led to a reconsideration of the simplified EHD model. Concretely, Taylor, McEwan & de Jong (1966) revised Taylor's earlier idea and introduced an improved model, namely the leaky dielectric model. In the leaky dielectric model, fluid is considered slightly conductive, allowing the free electric charge to accumulate on the interface of the emulsion. The leaky dielectric model is one of the successful models in the field of EHD and has been used by many researchers who want to numerically study the different behaviors of droplets under the effect of an electric field. These studies utilized various numerical methods including FVM[3] (Roghair, Musterd, van den Ende, Kleijn, Kreutzer & Mugele, 2015), FEM[4] (Santra, Mandal & Chakraborty, 2018), LBM[5] (Kupershtokh & Medvedev, 2006; Lauricella, Melchionna, Montessori, Pisignano, Pontrelli & Succi, 2018).

1.1.1.2 Confinement effect

The manipulation of fluids in geometrically constrained microchannels is of interest in microfluidics. When the fluid consists of droplets, it becomes an important

---

[3] Finite Volume Method

[4] Finite Element Method

[5] Lattice Boltzmann Method

subdivision of microfluidics called droplet-based microfluidics. Droplet-based microfluidics offers potential application in many areas, such as droplet-based LOC devices (Fink, Hamidović, Springer, Wille & Haselmayr, 2020), microreactors (Liu, Tian, Qiao, Zhou, Patil, Wang, Li & Mann, 2020), etc. In all droplet-based microfluidic devices, the dimensions of both the channel and the emulsion are comparable. The effect of this confinement on the leaky dielectric droplet under the applied electric field is considered by Behjatian & Esmaeeli (2013) and Esmaeeli & Behjatian (2012) for 2D and 3D geometries, respectively. In these studies, analytical procedures are used to solve the governing equations, and the small droplet deformation assumption is made. This assumption does not give an accurate result for the high amounts of the applied electric field. Santra et al. (2018) used COMSOL Multiphysics to simulate the droplet behavior under the confined geometry numerically. In this study, a single droplet and two separate droplets are located between two parallel electrodes to investigate their EHD dynamics. All of the above studies relate droplet deformation to two factors. The first factor is the magnitude of the normal hydrodynamics and electric stress, and the second one is the sign of the normal hydrodynamic stress. The authors then claimed that the confinement ratio affects these two factors.

1.1.1.3 Double emulsions

So far, it was concentrated on the dynamics of the single emulsion under different conditions. As mentioned earlier, double emulsions also play an essential role in many engineering applications. Double emulsions have a doubled-layer liquid droplet structure where the inner droplet (core) is covered by an emulsifier (shell) and further dispersed in another medium phase (Fig. 1.1-b). Double emulsions are either oil-in-water-in-oil (O/W/O) or water-in-oil-in-water (W/O/W). These systems have been exploited in many applications, specifically in food sciences (Paximada et al., 2021), cosmetics (Tarnowska et al., 2020), pharmacology (drug delivery, for instance) (Pontrelli et al., 2020), and wastewater treatment (Raghuraman et al., 1994).

Unlike a single emulsion, relatively few investigations have been performed on manipulating double emulsions considering the influence of an external electric field (Abbasi, Song, Kim & Lee, 2019; Santra, Das & Chakraborty, 2020; Spasic, Jovanovic, Manojlovic & Jovanovic, 2016; Tsukada, Mayama, Sato & Hozawa, 1997), or shear force (Chen, Liu & Shi, 2013; Hua, Shin & Kim, 2014; Luo, He & Bai, 2015), or the combination of these two forces (Borthakur, Nath & Biswas, 2021; Santra, Jana & Chakraborty, 2020) and needs further study to understand the behavior of double emulsions comprehensively.

1.1.2 Active matter

The other vital subdivisions of soft matter systems are active matters. The world is filled with living organisms whose scales extend from microscopic cells such as bacteria (Meacock, Doostmohammadi, Foster, Yeomans & Durham, 2021) to more giant creatures, including bird flocks (Bialek, Cavagna, Giardina, Mora, Silvestri, Viale & Walczak, 2012) and fish schools (Becco, Vandewalle, Delcourt & Poncin, 2006). These living organisms are categorized as active matters since they actively consume their internal or surrounding energy and convert it into motion.

Each entity of these materials tends to move disorderly in the system. However, when these elements are packed together, their collective motion is no longer disordered, described as an orientationally ordered phase of active matters by soft matter science. The collective chaotic motion is known as active turbulence (Alert, Casademunt & Joanny, 2022; Bratanov, Jenko & Frey, 2015; Doostmohammadi, Shendruk, Thijssen & Yeomans, 2017; Shendruk, Doostmohammadi, Thijssen & Yeomans, 2017; Urzay, Doostmohammadi & Yeomans, 2017; Wensink, Dunkel, Heidenreich, Drescher, Goldstein, Löwen & Yeomans, 2012), and in contrast to classical turbulence, it emerges in the absence of any external forces. Such chaotic flow represents a length scale larger than the constituent elements of active matter Martínez-Prat, Ignés-Mullol, Casademunt & Sagués (2019); Simha & Ramaswamy (2002), and the resultant velocity and jets are much larger than the individual element speeds Klotsa (2019); Marchetti, Joanny, Ramaswamy, Liverpool, Prost, Rao & Simha (2013). The study of active turbulence was the subject of many experimental and numerical studies, each of which tried to imitate the collective motion of active matters to gain a better understanding of the mechanisms and control their behavior in various fields such as biological, medical, and food science Doostmohammadi, Thampi, Saw, Lim, Ladoux & Yeomans (2015); Duclos, Adkins, Banerjee, Peterson, Varghese, Kolvin, Baskaran, Pelcovits, Powers, Baskaran, Toschi, Hagan, Streichan, Vitelli, Beller & Dogic (2020); Martínez-Prat et al. (2019); Urzay et al. (2017); Wensink et al. (2012).

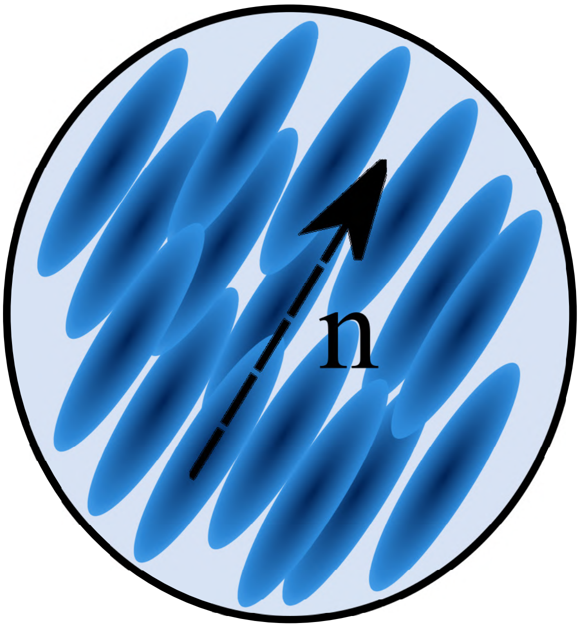

Figure 1.2 **Schematic representation of active nematics.** Rod-shaped nematic particles are aligned in the same direction but are free to drift around randomly.

1.1.2.1 Active nematics

Active nematic is one class of active matter which consists of a group of rod-shaped particles exhibiting head-tail symmetry (Fig. 1.2) which includes systems such as MT[6]-motor protein mixtures (Gao, Blackwell, Glaser, Betterton & Shelley, 2015), bacterial suspensions (Meacock et al., 2021), and cell assemblies (Doostmohammadi & Ladoux, 2022). The Greek term *nematic* is given to this category because they bear some resemblance to nematic liquid crystals. Nematic liquid crystals are made of elongated molecules characterized by long-range orientational order. However, the main difference between nematic liquid crystals and active nematics is the active nature of the constituent particles in active nematics. Due to this characteristic of the active nematics, topological defects generate and annihilate continuously yet randomly. Such behavior destroys the long-range orientational order in active nematics and leads to the emergence of active turbulence (Doostmohammadi, Ignés-Mullol, Yeomans & Sagués, 2018).

Topological defects are the points in the active nematics where there are director (**n** in Fig. 1.2) mismatches between the neighboring particles. These points are the singular points, and in 2D active nematics, the predominant defects are comet-like ($+1/2$) or trefoil-like ($-1/2$) defects where these numbers represent their charge (Doostmohammadi & Ladoux, 2022). In order to calculate the defect charge,

---

[6] Microtubule

one needs to perform a full ($+2\pi$) rotation around a defect point and calculate the changes in the orientation of particles on the rotation path (Doostmohammadi et al., 2018). In the active nematic systems, $+1/2$ defects are motile, and their movement direction is toward their comet head and their comet tail in extensile and contractile systems, respectively. This movement direction is significant as it determines the direction of imposed force by the nematic particles (Doostmohammadi & Ladoux, 2022).

1.2 Numerical prospective

Generally, three main approaches are available to study fluid flow, including experimental, analytical, and numerical methods. The experimental procedure gives the desired results; however, it is a pretty expensive method, and in some cases, it is impossible to perform a suitable setup. The analytical method is accurate, but it is limited to elementary geometries and models. On the other hand, numerical methods give rise to the field of CFD[7]. These methods are promising as they can solve any complex equation. However, the accuracy of the model affects the outcomes of this method. Moreover, the large domains or complex physics such as turbulence physics require very fine resolution, which is computationally expensive. HPC[8] can alleviate the computational cost problem and will be discussed in the next section.

In the macro-scale CFD, two general approaches exist for solving the interest equations, namely mash-free and mesh-based methods. Each of these methods has its pros and cons. Mesh-based methods need an Eulerian grid for discretizing the physical domain. The grid makes these methods challenging to implement into geometrically complex problems and physics with moving boundaries. Mesh-free methods, however, do not need a grid and can effortlessly model these complex problems. Computationally expensive cost is the flip side of the mesh-free methods. In this thesis, both methods are used to simulate soft matter physics. For this purpose, SPH[9] method and FVM are used. The SPH method represents the mesh-free approach, while theFVM is typical of the mesh-based class. To implement the FVM,

---

[7] Computational Fluid Dynamics

[8] High Performance Computing

[9] Smoothed Particle Hydrodynamics

an open source package, namely OpenFOAM[10], is utilized.

1.2.1 Smoothed Particle Hydrodynamics

SPH is a mesh-free particle-based Lagrangian method invented to simulate astrophysical problems (Gingold & Monaghan, 1977; Lucy, 1977). In SPH, macroelements of the fluid are replaced with a set of particles, and they are used to calculate and store the fluid properties. These properties are determined by interpolation variables from the particles taking advantage of kernel approximation. SPH has several attractive features that make this method a powerful tool to deal with complicated physics. For instance, it can effortlessly handle the moving boundaries as in free surface flow (Ozbulut, Tofighi, Goren & Yildiz, 2017; Ozbulut, Yildiz & Goren, 2014a), multiphase flow (Zainali, Tofighi, Shadloo & Yildiz, 2013a), and FSI[11] (Ghazanfarian, Saghatchi & Gorji-Bandpy, 2015,1; Saghatchi, Ghazanfarian & Gorji-Bandpy, 2014).

1.2.2 OpenFOAM

OpenFOAM is an open-source package based on C++ programming language that is capable of solving complex PDEs[12]. OF contains various solvers and utilities to deal with the different physical problems. OpenFOAM discretizes the PDEs based on FVM in space and FDM[13] in time (Weller, Tabor, Jasak & Fureby, 1998). It offers pre- and postprocessing environment and can deal with 2D and 3D problems.

Due to the object-oriented nature of Openfoam, any PDE can be introduced into the package simply. For example, the following transport equation:

$$\frac{\partial T}{\partial t} + \boldsymbol{\nabla} \cdot (\vec{u}T) - \boldsymbol{\nabla} \cdot (\nu \boldsymbol{\nabla} T) = 0 \tag{1.1}$$

---

[10] Open source Field Operation And Manipulation

[11] Fluid-Structure Interaction

[12] Partial Differential Equation

[13] Finite Difference Method

is implemented in OpenFOAM as (Weller et al., 1998):

```
solve
(
fvm::ddt(T)
+ fvm::div(phi, T)
- fvm::laplacian(nu, T)
);
```

which makes the code easier to write, validate, and maintain.

1.2.3 High Performance Computing

As mentioned before, the downside of the CFD techniques is their high computational costs in some physics. HPCs are developed to alleviate such difficulty by executing parallel operations. The drawback of parallel processing is its implementation and coding, which requires the user to become familiar with the parallelization algorithms.

Parallel computing can be applied with either shared memory hardware or distributed memory. In the former approach computational machine uses the same memory space for the multiple processors. One famous example of shared memory parallel computation is OpenMP[14] (Chandra, Dagum, Kohr, Menon, Maydan & McDonald, 2001). However, in the distributed memory approach, each processor has its own memory space and can not directly access the memory associated with other processors. This system uses an explicit message passing model to perform data exchange between processors. One of the typical examples of distributed memory systems is MPI[15] (Gropp, Lusk & Skjellum, 1999; Pacheco, 1997).

GPUs[16] are also used for computation purposes in recent years, and their application in the CFD field is getting popular. Although the original duty of GPU is graphics rendering, their computing capability has grown, which makes GPUs faster than CPUs[17] for CFD computations. Various platforms are being used to utilize

---

[14] Open Multi-Processing

[15] Message Passing Interface

[16] Graphics Processing Unit

[17] Central Processing Unit

GPU's computational capabilities, such as OpenCL[18] (Group & others, 2008) and CUDA[19] (Sanders & Kandrot, 2010). CUDA attracts more attention among researchers mainly because of its enormous documentation and utilities available on the CUDA website (https://developer.nvidia.com/cuda-zone). Furthermore, a performance comparison between these two platforms reveals that CUDA performs 30% better (Fang, Varbanescu & Sips, 2011).

1.3 Aims and scope

This thesis aims to develop an SPH method for describing two important subclasses of soft matters, including emulsions and active nematics. The computational code is parallelized using the CUDA platform to hasten the computational speed. Effects of domain confinement and applied external electric fields are investigated on the dynamics of single and double emulsions. Then, the SPH code is used to simulate the continuum model of active nematics for the first time. At the same time, EHD and active nematic solver is developed based on the OpenFOAM package to verify the results obtained by SPH. It is also used to simulate the problems where SPH encountered multiple difficulties.

This thesis is structured into nine chapters, including the introduction (current chapter. 1), mathematical formulation of emulsions and active nematics (chapter. 2), numerical implementation (chapter. 3), and five peer-reviewed journal articles (three in press, two under review), one peer-reviewed conference contributions (chapters. 4 through. 8), and finally the conclusion and suggestion for the future studies (chapter. 9).

---

[18] Open Computing Language

[19] Compute Unified Device Architecture

2. MATHEMATICAL FORMULATION

This chapter gives the theoretical framework for the rest of this thesis. As discussed in the introduction, the goal is to study the soft matter system, including emulsions and active nematics. As such, we provide a theoretical framework and the formulation for each of these systems separately. It should be noted that throughout this thesis, the fluids are assumed to be incompressible, Newtonian, immiscible, and isothermal, flowing in a two-dimensional domain.

We start this chapter by introducing the necessary equations for describing emulsion dynamics under the effect of the electric field. Thus, we formulate the surface tension and the electric forces and express them as volumetric local forces that can readily be used in the governing equation. Then, active nematics are presented by introducing the nematic orientation field and order parameter tensor. Then we explain the active stress that introduces the instability into the system.

2.1 Emulsions

The equations describing the evolution of emulsion include conservation of mass and linear momentum as follows (Eringen, 1980):

$$\boldsymbol{\nabla} \cdot \vec{u} = 0, \tag{2.1}$$

$$\rho \frac{\mathrm{D}\vec{u}}{\mathrm{D}t} = \boldsymbol{\nabla} \cdot \boldsymbol{\Pi} + \vec{f}, \tag{2.2}$$

where ρ, $\vec{u}$, and t, are density, the velocity vector, and time, in the given order. $\boldsymbol{\Pi}$ denotes the stress tensor which includes the pressure term ($-p\mathbf{I}$) with $\mathbf{I}$ representing the identity tensor, and the viscous term $\mathbf{\Pi}_{\text{viscous}} = 2\rho\nu\mathbf{E}$ where ν is the kinematic viscosity, and $\mathbf{E} = \frac{1}{2}\left[\boldsymbol{\nabla}\vec{u} + (\boldsymbol{\nabla}\vec{u})^{\dagger}\right]$ represents the rate of strain tensor. D/Dt operator is the material time derivative which is defined as $\mathrm{D}/\mathrm{D}t = \partial/\partial t + \vec{u}\cdot\boldsymbol{\nabla}$. The last term $\vec{f}$ includes the surface tension ($\vec{f_s}$) and electric forces ($\vec{f_e}$). It should be noted that the gravitational force is neglected throughout this study. In the following sections, we aim to formulate these two forces.

2.1.1 Surface tension

Each phase tends to shrink into the minimum surface area possible in a system containing two or more immiscible liquids. This tendency initiates from the cohesive nature of liquid molecules known as surface tension, allowing the liquids to resist the external forces applied to their surface.

In this study, CSF[1] scheme is used to model the surface tension force (Brackbill, Kothe & Zemach, 1992). This method expresses the surface force on the interface as a volumetric local force (i.e., a body force) while explicitly replacing the infinitely thin interface between two liquids with a finite thickness transition region. As such, interface curvature is calculated as follows (Zainali, Tofighi, Shadloo & Yildiz, 2013b):

$$\vec{f_s} = \gamma\kappa\vec{n}\delta, \tag{2.3}$$

where γ and δ, respectively represent the surface tension coefficient and the Dirac delta function. $\kappa = -\boldsymbol{\nabla}\cdot\vec{n}$ is the local interface curvature with $\vec{n}$ denoting the unit surface normal vector.

2.1.2 Electric force

In this part, we focus on the derivation of electrostatic forces that are used in combination with the hydrodynamic equations to explain the electrohydrodynamics behavior of the system. We start by making some essential assumptions that allow

---

[1] Continuum Surface Force

us to write the relevant governing equations for the electrostatic field within the fluids and across the liquid interfaces:

- The system containing the multiphase flow is non-polarizable and non-magnetizable.
- A quasi-static electric field model is applicable to the system.

The latter assumption is the consequence of the insignificant dynamic current, hence the negligible influence of magnetic induction. With such an assumption, one can ignore the magnetic induction, leading to the elimination of Ampere's law of the list of governing equations. In the absence of an external magnetic field, Faraday's law can be simplified to the following equation:

$$\nabla \times \vec{E} = 0, \tag{2.4}$$

where $\vec{E}$ denotes the electric field vector. From (2.4), it can be inferred that the gradient of the electric field vector is symmetric (i.e., $\nabla\vec{E} = (\nabla\vec{E})^{\dagger}$). Using the fact that the curl of a gradient of any scalar/vector-valued function is is zero (i.e., $\nabla \times (\nabla\phi) = 0$), we can express the electric field as (Castellanos, 1998):

$$\vec{E} = -\boldsymbol{\nabla}\phi, \tag{2.5}$$

where scalar ϕ designated the electric potential.

To account for the free electric charges in the domain, the total volume current ($\vec{J}$) is introduced as (Eringen & Maugin, 2012):

$$\vec{J} = q_v\vec{u} + \vec{j}, \tag{2.6}$$

where q_v is the volume-charge density of free charges, $\vec{j}$ is the volume conduction current density. The first term on the right-hand side of (2.6) accounts for the convection induced by the fluid motion, and the last term denotes the ohmic current which is related to the electric field through the following relation (Eringen &

Maugin, 2012):

$$\vec{j} = \sigma \vec{E}, \tag{2.7}$$

where σ is the physical property of material known as the electrical conductivity.

To relate the electric field with free electric charges, Gauss's law is solved which can be written as (Eringen & Maugin, 2012):

$$\nabla \cdot \vec{D} = q_v, \tag{2.8}$$

where the electric permitivity ε determines the degree of this coupling. The term $\varepsilon \vec{E}$ is known as electric displacement and is represented by $\vec{D}$.

In order to obtain the conservation charge, we begin with the differential form of Ampere's law (Eringen & Maugin, 2012):

$$\nabla \times \vec{B} = \frac{1}{c}[\frac{\partial \vec{D}}{\partial t} + \vec{J}], \tag{2.9}$$

where c is the speed of light in vacuum. Taking the divergence of (2.9) and noting that the divergence of the curl of any arbitrary vector field is equal to zero ($\nabla \cdot (\nabla \times \vec{B}) = 0$), yields:

$$\nabla \cdot [\frac{\partial \vec{D}}{\partial t} + \vec{J}] = 0. \tag{2.10}$$

Combining Eqs. 2.5, 2.8, and 2.10 results in the conservation of charge equation as follows (Castellanos, 1998):

$$\frac{Dq_v}{Dt} = -\nabla \cdot \vec{j}. \tag{2.11}$$

In the emulsion system containing the interface between two liquids, jump conditions are used for Maxwell's equations to relate interfacial and bulk properties of the emulsion. The jump conditions corresponding to Eqs. 2.4, 2.8, and 2.11 are written as (Eringen & Maugin, 2012; Saville, 1997):

$$\vec{n} \times \left\| \vec{E} \right\| = 0, \tag{2.12}$$

$$\vec{n} \cdot \left\| \vec{D} \right\| = q_s, \tag{2.13}$$

and

$$\bar{\delta} q_s / \delta t + \nabla_s \cdot \vec{K} + \vec{n} \cdot \left\| \vec{J} - q_v \vec{v} \right\| = 0, \tag{2.14}$$

in the given order. In these equations, the symbol $\| \quad \|$ represents the jump of the enclosed quantities across the interface ξ, q_s is the a surface density of free charge (charge per unit surface area), and ∇_s is the surface gradient operator. $\bar{\delta} q_s / \delta t = \partial / \partial t + (\vec{v} \cdot \vec{n})(\vec{n} \cdot \nabla)$ is the total time derivative in following the motion of ξ along its unit normal vector $\vec{n}$. The velocity of discontinuity surface is represented by $\vec{v}$, and $\vec{K} = \vec{k} + q_s \vec{v}$ is the total surface current where $\vec{k}$ and $q_s \vec{v}$, respectively are the surface conduction and convection currents.

Finally, the electrostatic field is coupled to the emulsion interface by taking the divergence of the Maxwell stress tensor $\mathbf{T}_e$ and the result is incorporated in the linear momentum balance equation (2.2) via volumetric electric force $\vec{f}_e = \nabla \cdot \mathbf{T}_e$. The Maxwell stress tensor can be written as (Saville, 1997; Shadloo, Rahmat & Yildiz, 2013):

$$\mathbf{T}_e = \vec{D} \otimes \vec{E} - 0.5 (\vec{D} \cdot \vec{E}), \tag{2.15}$$

It should be noted that the contribution of the induced magnetic field is neglected in the derivation of this equation. However, alternative forms of the Maxwell stress tensor may be found in the literature (see for example, Das & Saintillan (2021); Reich, Rickert & Müller (2018); Roghair et al. (2015)). Taking the divergence of (2.15) and combining (2.8) yields:

$$\vec{f_e} = q_v\vec{E} - \frac{1}{2}\vec{E}\cdot\vec{E}\boldsymbol{\nabla}\varepsilon. \tag{2.16}$$

The first and the second terms on the right-hand side of (2.16) are Coulomb and polarization forces, respectively, where the former force is the result of the interaction between free charges and the electric field and acts along the direction of the electric field, whereas the latter force acts along the normal direction to the interface due to the pairs of charges.

Considering a homogeneous fluid with uniform electrical conductivity σ, permittivity ε, and viscosity μ, where the system of interest is characterized by a length scale L, two primary time scales are generally involved (Saville, 1997): the viscous time scale $t_\mu = \rho L^2/\mu$, and the electrical relaxation time $t_e = \varepsilon/\sigma$. In this thesis, the emulsion system is considered as conducting-conducting (leaky dielectric), hence $t_\mu \gg t_e$. Consequently, both volume and surface charges can reach steady state, i.e., $Dq_v/Dt = 0$ and $\bar{\delta}q_s/\delta t = 0$. Additionally, if (2.11) is written in a non-dimensional form, recalling that $t_\mu \gg t_e$, the contribution of the surface current $\vec{k}$ to the physics of problem can be neglected and the total surface current reduces to $\vec{K} \approx q_s\vec{v}$. Moreover, assuming that the discontinuity surface is a material interface, then, $\vec{u} = \vec{v}$. Therefore, relying on the aforementioned assumption, the conservation of charge in (2.11) in the volume and on the discontinuity surface, respectively can be simplified to (Shadloo et al., 2013):

$$\nabla\cdot(\sigma\nabla\phi) = 0, \qquad \vec{n}\cdot\|\sigma\nabla\phi\| = 0. \tag{2.17}$$

Furthermore, the final version of the Gauss'law for electricity for the volume (i.e., (2.8)) and the discontinuity surface (i.e., (2.13)), respectively follows as (Shadloo et al., 2013);

$$\nabla\cdot(\varepsilon\nabla\phi) = q_v, \qquad \vec{n}\cdot\|\varepsilon\nabla\phi\| = 0. \tag{2.18}$$

Upon combining (2.2) with Eqs. 2.3 and 2.16, one can obtain the equation of motion including volumetric surface tension and electric field forces to describe the dynamics of emulsions under the applied electric field.

2.2 Active nematics

As mentioned in the previous chapter, active fluids are an important category of soft matter systems. This section focuses on continuum modeling of systems containing active microscopic particles. Despite the microscopic size of individual particles, their collective movement exhibits significantly larger scales. We focus on active nematics, i.e., systems where the collective dynamics manifest nematic flow symmetries. These systems exhibit chaotic flow in bulk due to the collective hydrodynamic stress generated by active constituent particles.

2.2.1 Nematic Liquid Crystals

Condensed matter physics categorizes the materials into three distinct phases; solid crystals, isotropic liquids, and liquid crystals (Fig. 2.1). Crystalline solid is a state of matter in which the constituents are arranged in a highly ordered manner, and they have little translational freedom. The isotropic liquid state, in contrast, has neither orientational nor positional order, and the components are free to move randomly. Liquid crystals fall in between, exhibiting many of the physical attributes of a liquid (e.g., cannot withstand the shear force), while their elements are sufficiently ordered to give rise to some anisotropy (De Gennes & Prost, 1995).

Journey in the Liquid crystal research began in 1888 when Friedrich Reinitzer, an Austrian botanist— or biochemist in modern terms, surprisingly noticed that cholesterol crystals had two unique melting points (Reinitzer, 1888). The crystalline solid melted into a hazy liquid at first, but eventually, the cloudiness vanished, leaving a clear, transparent liquid as one would expect after melting. In 1922, Friedel gave the first classification scheme for naming the different phases of liquid crystals, including nematic liquid crystals (Friedel, 1922). When he showed his daughter photographs of liquid crystals taken through a microscope, she proposed the name nematics, which originates from the Greek word “nêmatos” meanings thread (Mitov, 2014).

Nematic liquid crystals have long-range orientational order and are characterized

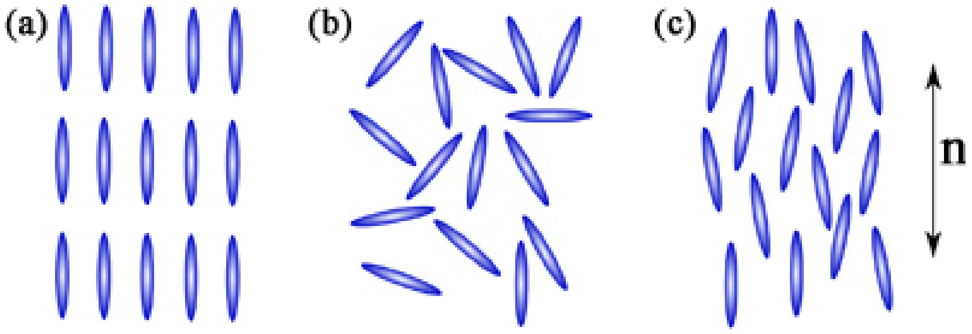

Figure 2.1 **Schematic representation of matter phase.** (a) Crystalline solid in which the atoms, ions, or molecules are arranged in a definite repeating pattern and exhibits long range periodic order. (b) Isotropic liquid with no orientational and positional order. (c) Nematic liquid crystal characterized by molecules that have no positional order but tend to point in the same direction (along the director $\hat{n}$). The director $\hat{n}$ denotes the local average orientation of the liquid crystal.

by a coarse-grain variable, i.e., an orientation field that describes the anisotropic structure of nematic liquid crystals. The average orientation of nematic particles is described by the nematic orientation $\hat{n}$ which is shown in Fig. 2.1c. Since nematic particles have a head-tail symmetry structure, $\hat{n}$ is an apolar quantity meaning that $\hat{n}$ and $-\hat{n}$ are equivalent, thereby leading to the same ordered state. In addition to $\hat{n}$, an order parameter q is necessary to evaluate the local particles' ordering and distinguish isotropic liquid (Fig. 2.1b) from nematic liquid (Fig. 2.1c) which define as follows (De Gennes & Prost, 1995):

$$q = \left\langle P_2\Big(cos^2(\theta_i)\Big)\right\rangle = \left\langle \frac{3}{2}cos^2(\theta_i) - \frac{1}{2}\right\rangle = \int f(\theta)\Big(\frac{3}{2}cos^2(\theta) - \frac{1}{2}\Big)\, d\Omega. \tag{2.19}$$

Here, P_2 denotes the second Legendre polynomial, θ_i is the angle between the local particles and the director $\hat{n}$ (Fig. 2.2). Function $f(\theta)d\Omega$ is the probability distribution function and describes the average local rod alignment. The symbol $\langle\quad\rangle = \frac{1}{N}\sum(\quad)$ represents the average of the enclosed quantities over the local number of particles N. The scalar quantity q measures the magnitude of alignment and varies between 0 and 1, where $q = 0$ corresponds to complete orientational disorder while for the perfect orientational order $q = 1$.

To define both the isotropic-nematic transition and the local orientation, we need a single parameter that describes both q and $\hat{n}$. Thus, we define a single traceless symmetric tensor order parameter $\mathbf{Q}$ using the quadrupole expansion as fol-

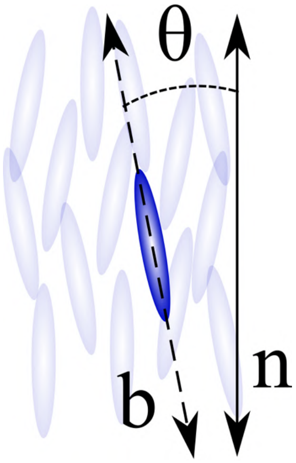

Figure 2.2 **Nematic particles' orientational parameters.** Each particle has its own orientation $\hat{b}$ and the average of all particles' orientation is described by the nematic orientation $\hat{n}$. Consequently, deviation of individual particle orientation from the mean value is represented by angle θ.

lows (De Gennes & Prost, 1995):

$$\mathbf{Q} = \left\langle \hat{b}\hat{b} - \frac{\mathbf{I}}{d} \right\rangle, \tag{2.20}$$

where, $\hat{b}$ is the orientation of individual particles (Fig. 2.2), and d denotes the dimension of space. $\mathbf{Q}$ can be rewritten in terms of $\hat{n}$ as (De Gennes & Prost, 1995):

$$\mathbf{Q} = \frac{d}{d-1} q \left(\hat{n}\hat{n} - \frac{\mathbf{I}}{d} \right). \tag{2.21}$$

This formulation for $\mathbf{Q}$ allows us to describe the evolution of $\hat{n}$ and q. Mathematically, $\hat{n}\hat{n}$ is a tensor product, and it is equivalent to $\vec{n}\vec{n}$. Consequently, in (2.21), one can treat $\hat{n}$ as a polar vectorial field, eliminating the additional concerns that arise when dealing with an apolar quantity. Inversely, director $\hat{n}$ and scalar order parameter q can be determined by calculating the eigenvectors of $\mathbf{Q}$. As such, $\hat{n}$ and q are the eigenvector with the largest eigenvalue and the corresponding eigenvalue, respectively.

2.2.2 Continuum model

After describing the director $\hat{n}$ and scalar order parameter q by tensor order parameter $\mathbf{Q}$, we can now study their evolution in time. In order to do that, we use the continuum approach to model the dynamics of active nematics (Doostmohammadi et al., 2018; Marchetti et al., 2013; Prost, Jülicher & Joanny, 2015; Ramaswamy, 2010a). We begin by introducing the equation for describing the evolution of Q, and then we move to the hydrodynamic equation of active nematics to fully describe the behavior of system.

2.2.2.1 Active nematodynamics

The dynamics of tensor order parameter $\mathbf{Q}$, is described by Beris- Edwards equation as (Beris & Edwards, 1994):

$$\frac{\mathrm{D}\mathbf{Q}}{\mathrm{D}t} - \mathbf{S} = \Gamma \mathbf{H}, \tag{2.22}$$

where $\mathbf{S}$ is the co-rotation term and accounts for the $\mathbf{Q}$ reorientations due to the rotational and extensional components of the flow gradient, characterized by the vorticity tensor $\mathbf{\Omega} = \frac{1}{2}\left[(\boldsymbol{\nabla}\vec{u})^{\dagger} - \boldsymbol{\nabla}\vec{u}\right]$ and the rate of strain tensor $\mathbf{E} = \frac{1}{2}\left[\boldsymbol{\nabla}\vec{u} + (\boldsymbol{\nabla}\vec{u})^{\dagger}\right]$. The derivation of these relation is given in a detailed manner in Appendix A. Concretely, in the 2D domain, the co-rotation term $\mathbf{S}$ has the following form:

$$\mathbf{S} = \lambda \mathbf{E} - (\mathbf{\Omega} \cdot \mathbf{Q} - \mathbf{Q} \cdot \mathbf{\Omega}). \tag{2.23}$$

Here, λ is the tumbling parameter and adjusts the degree of coupling between nematic alignment and the flow gradient (Marenduzzo, Orlandini, Cates & Yeomans, 2007a). Physically, $|\lambda| > 1$ and $|\lambda| < 1$ respectively correspond to flow alignment and flow tumbling of nematics under the shear effect (Carenza, Gonnella, Lamura, Negro & Tiribocchi, 2019; Thampi, Golestanian & Yeomans, 2014b).

The right-hand side of (2.22) accounts for the relaxation of $\mathbf{Q}$ to the minimum of the free energy $\mathcal{F}$, while this relaxation is controlled temporally by rotational diffusivity

Γ and determined by the molecular field **H** defined as:

$$\mathbf{H} = -\frac{\delta \mathcal{F}}{\delta \mathbf{Q}} + \frac{\mathbf{I}}{2}\mathrm{Tr}\left(\frac{\delta \mathcal{F}}{\delta \mathbf{Q}}\right), \tag{2.24}$$

where Tr() represents the trace operator.

Deformations in the orientation field occur at the cost of a free energy $\mathcal{F} = \mathcal{F}_e + \mathcal{F}_b$, which includes both the elastic free energy cost $\mathcal{F}_e$ and the bulk free energy $\mathcal{F}_b$. The elastic free energy $\mathcal{F}_e$ penalizes the gradients in the orientation, which can be approximated by using Frank elastic free energy as (De Gennes & Prost, 1995):

$$\mathcal{F}_e = \frac{1}{2}\Big[K_{splay}\big(\boldsymbol{\nabla}\cdot\hat{n}\big)^2 + K_{bend}\big(\hat{n}\times(\boldsymbol{\nabla}\times\hat{n})\big)^2 + K_{twist}\big(\hat{n}\cdot(\boldsymbol{\nabla}\times\hat{n})\big)^2\Big], \tag{2.25}$$

where ks are the Frank elastic constants, and the three terms in (2.25) correspond to splay, twist and bend deformation, respectively, as illustrated in Fig. 2.3. Note that additional terms associated with boundaries are ignored in (2.25). The elastic deformation free energy cost can be simplified into a single constant equation by assuming that all constants in (2.25) are equal (i.e., $K = K_{splay} = K_{bend} = K_{twist}$). Furthermore, since we are interested in expressing the equations in terms of **Q** rather than $\hat{n}$, we map $\mathcal{F}_e$ to derivatives in **Q** as follows:

$$\mathcal{F}_e = \frac{1}{2}K(\boldsymbol{\nabla}\mathbf{Q})^2, \tag{2.26}$$

with k denoting a single elastic constant.

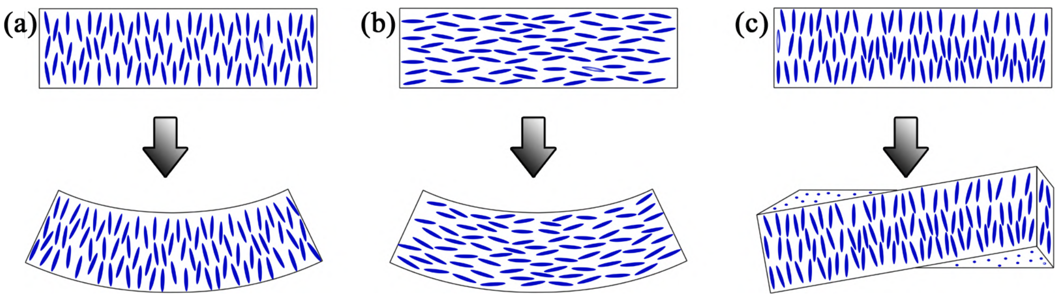

Figure 2.3 **The three types of bulk director deformations that occur in nematic liquid crystals:** (a) splay, (b) bend, and (c) twist.

Another term that contributes to the cost of a free energy is the bulk free energy $\mathcal{F}_b$

that insures a stable nematic ordering at the thermodynamic equilibrium. The only rotationally invariant function of $\mathbf{Q}$ are $\mathrm{Tr}[\mathbf{Q}]^2$) and $\mathrm{Tr}[\mathbf{Q}]^3$). To ensure thermodynamic stability, the isotropic to nematic phase transition is built around a power series expansion as (De Gennes & Prost, 1995):

$$\mathcal{F}_b = \frac{C_0}{2} + \frac{C_1}{2}\mathrm{Tr}[\mathbf{Q}]^2 + \frac{C_2}{3}\mathrm{Tr}[\mathbf{Q}]^3 + \frac{C_3}{4}(\mathrm{Tr}[\mathbf{Q}]^2)^2, \tag{2.27}$$

Where C_is are Landau-de Gennes coefficients, and by altering their values, one may set the isotropic or nematic state as the global ground state. C_3 should be taken as a positive value to ensure the system's stability against unbounded growth of the scalar order parameter q. Moreover, in a 2D domain, we can neglect the $\mathrm{Tr}[\mathbf{Q}]^3$ term due to symmetry (De Gennes & Prost, 1995), and this choice does not affect the continuous phase transition from isotropic to nematic (Vink, 2014). In this study we take $C_0 = A$, $C_1 = -A$, $C_2 = 0$, and $C_3 = A/2$ with A being the only positive coefficent that controls the bulk free energy as follows:

$$\mathcal{F}_b = \frac{A}{2}(1 - \frac{1}{2}\mathrm{Tr}[\mathbf{Q}]^2)^2, \tag{2.28}$$

which is the common form in the literature (Fielding, Marenduzzo & Cates, 2011; Marenduzzo, Orlandini, Cates & Yeomans, 2007b).

2.2.2.2 Hydrodynamics of active nematics

So far, we have introduced the equations to describe the evolution of the nematic order tensor $\mathbf{Q}$ in terms of both nematic order q and orientation field $\hat{n}$. In this section, we discuss the dynamics of the velocity field to be able to describe the active nematic systems completely.

The self-propelled active particles create flow as they move at very small Reynolds number in the system by slightly oscillating their shape (Lighthill, 1952). According to Newton's third law, the mutual forces of active swimmers and the surrounding fluid balance (Aditi Simha & Ramaswamy, 2002). Consequently, swimmers have no monopole moments (i.e., the integration of the total momentum density must be zero). A minimal model to describe the active particles and their farfield is, therefore, a model that simplifies the swimmers as points that generate dipole moment and subsequently induce flow field (Ramaswamy, 2010b). The swimming particles can either be pushers (extensile) or pullers (contractile). In the former type, fluid is sucked in along the swimmers' waist and pushed forward and backward, respectively, by their heads and their tails. Consequently, the corresponding dipoles' forces point outwards (Fig. 2.4a). In the second type, fluid is pulled in by the swimmers' flagella toward their bodies and pushed outward along the swimmers' waists. In contrast to the pusher type, the resultant dipoles' forces point inwards in the puller type swimmers (Fig. 2.4b). An example of pusher-type swimmers is the E. coli bacteria (Riley, Das & Lauga, 2018), and an example of a puller-type is the Chlamydomonas algae (Lauga & Powers, 2009).

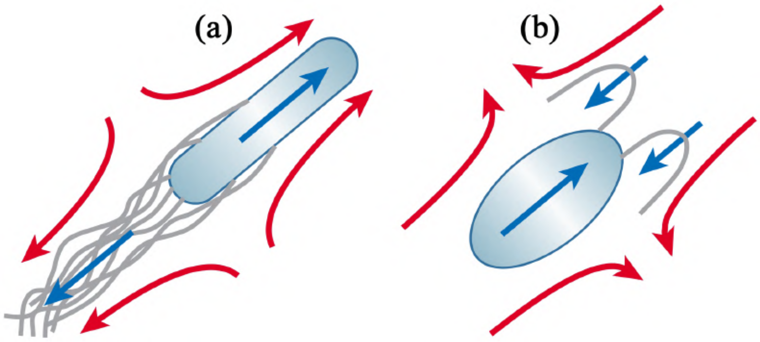

Figure 2.4 **Schematic of active swimmers.** (a) Pushers (extensile) system. (b) Pullers (contractile) system. Red arrows denote the induced flow direction and blue arrows represent the dipole forces. (Image taken from Saintillan (2018).)

Assuming Newtonian fluid, generalized incompressible Navier Stokes equations (i.e., Eqs. 2.1 and 2.2) are used for active nematics. Moreover, due to the absence of any external electric field and surface tension force, we assume that $\vec{f} = 0$.

For the active systems, apart from the pressure term $-pI$ and the viscous term $\mathbf{\Pi}_{\text{viscous}}$, the stress tensor $\mathbf{\Pi}$ includes an additional term, i.e., active stress tensor $\mathbf{\Pi}_{\text{active}} = -\zeta \mathbf{Q}$ which introduces the activity into the system. $\mathbf{\Pi}_{\text{active}}$ couples the velocity field to the orientation field, and the magnitude of the activity coefficient ζ controls the strength of active stress tensor. Furthermore, the sign of activity parameter determines whether the self-propelled particles are extensile ($\zeta > 0$) or contractile ($\zeta < 0$) (Simha & Ramaswamy, 2002). One may see an additional term in the literature on active fluids, namely elastic stress tensor. However, in studies of active nematics, this term is typically dominated by active contributions and is commonly neglected (Blanch-Mercader & Casademunt, 2017; Hardoüin, Hughes, Doostmohammadi, Laurent, Lopez-Leon, Yeomans, Ignés-Mullol & Sagués, 2019). Similarly, we disregard the passive elastic term and focus on the role of active stresses on the dynamics of nematic systems.

2.3 Agreement between computation and experiment

One of the crucial issues in the numerical simulation of active nematics is the calibration of the parameters such that the numerical results correctly resemble the actual behavior of the active fluid. In terms of qualitative results, the onset of active turbulence is one of the main characteristics of active fluids, which verifies the correctness of the used parameters in the numerical study. In terms of quantitative results, however, various characteristics might be considered and compared between the experimental and numerical results.

Thampi et al. (2013) performed a numerical simulation of a 2D, active nematic suspension based on the continuum scheme and compared the rms velocity variation with the experimental results of Sanchez, Chen, DeCamp, Heymann & Dogic (2012). Consequently, they demonstrated the similarity between activity coefficient ζ and ATP[2]. Turiv, Krieger, Babakhanova, Yu, Shiyanovskii, Wei, Kim & Lavrentovich (2020) performed an experimental study using the cell monolayers of human dermal fibroblasts with predesigned orientational patterns and topological defects using a photoaligned liquid crystal elastomer to estimate the elastic constant K and surface anchoring parameter of the tissue for a numerical study of active nematics formed by extensile units. Thijssen, Metselaar, Yeomans & Doostmohammadi (2020) conducted a study to estimate the flow aligning parameter λ and reproduce the experimental results on microtubule–kinesin motor mixtures.

These are examples of the ongoing studies which aim to perfectly estimate the different parameters of the various active agents in future numerical simulations.

---

[2] Adenosine triphosphate

3. NUMERICAL MODELS

Chapter 2 established the mathematical model to describe the complex soft matter systems, including the emulsions and active nematics. This chapter introduces the necessary tools to solve the governing equations numerically. This study uses two distinct numerical methods, including SPH and FVM, where both of them are introduced in the following sections.

3.1 Smoothed Particle Hydrodynamics

The SPH method was first developed in the 1970s by Lucy (1977) and Gingold & Monaghan (1977) independently for non-axisymmetric phenomena in astrophysical applications. The ease of implementing the SPH method for complex physics made it quite alluring to deal with complex physics with nonlinear behaviors. Engineering applications of SPH emerged in the 1990s and early 2000s. Since then, this method has developed rapidly in numerous fields, including energy, mass, and momentum transfers.

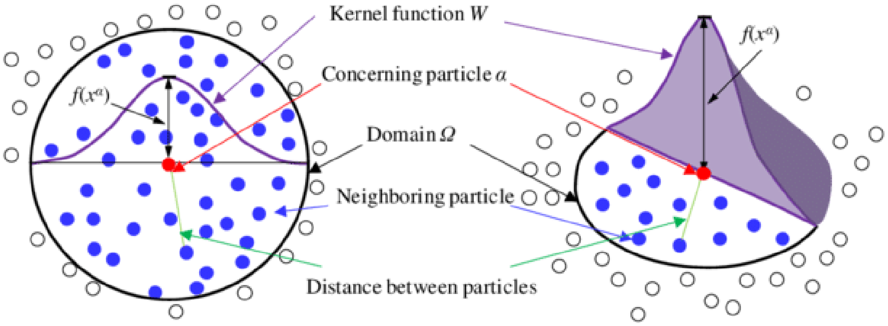

Figure 3.1 **The schematic concept behind the SPH method.** A red dot shows the particle of interest, and its neighboring particles inside the support domain are demonstrated in blue. (The image is adapted from Dai et al. (2016).)

To put it in a nutshell, SPH is simply an interpolation method that approximates any function with a set of particles (Fig. 3.1). These particles carry important information such as mass, energy, momentum, and other required properties. Mathematically, approximation of arbitrary function f on the spatial coordinate set denoted by the vector $\vec{r_\mathbf{i}} \in \mathbb{R}^3$ can be written as (Gingold & Monaghan, 1977):

$$f(\vec{r_\mathbf{i}}) \approx \langle f(\vec{r_\mathbf{i}}) \rangle \equiv \int_\Omega f(\vec{r_\mathbf{j}}) W(\vec{r_\mathbf{i}} - \vec{r_\mathbf{j}}, h) d^3\vec{r_\mathbf{j}}, \tag{3.1}$$

where i and j denote the particle of interest, and the neighboring particle, respectively. The integral is calculated on the domain Ω, and $d^3\vec{r_\mathbf{j}}$ is a differential volume element. $W(\vec{r_\mathbf{i}} - \vec{r_\mathbf{j}}, h)$ is the foundation of SPH algorithm, known as kernel function, which is an approximated form of Dirac delta function $\delta(\vec{r_\mathbf{i}} - \vec{r_\mathbf{j}})$ that has the properties as follows:

$$\delta(\vec{r_\mathbf{i}} - \vec{r_\mathbf{j}}) = \begin{cases} 0, & \vec{r_\mathbf{i}} - \vec{r_\mathbf{j}} \neq 0 \\ \infty, & \vec{r_\mathbf{i}} - \vec{r_\mathbf{j}} = 0 \end{cases}, \qquad \int_{-\infty}^{\infty} \delta(\vec{r_\mathbf{i}} - \vec{r_\mathbf{j}}) dr = 1, \qquad \delta(\vec{r_\mathbf{i}} - \vec{r_\mathbf{j}}) = \delta(\vec{r_\mathbf{j}} - \vec{r_\mathbf{i}}). \tag{3.2}$$

Equation 3.1 dictates an interpolation within a spherical neighborhood defined by the smoothing length parameter h, in which the kernel function acts as a weighting factor. Various kernel functions are available in the literature, while in this study, the quintic kernel function is used, which reads (Morris, Fox & Zhu, 1997):

$$W(b, \kappa h) = a_d \begin{cases} (3-b)^5 - 6(2-b)^5 + 15(1-b)^5, & 0 \leq b \leq 1 \\ (3-b)^5 - 6(2-b)^5, & 1 \leq b \leq 2 \\ (3-b)^5, & 2 \leq b \leq 3 \\ 0, & b \geq 3 \end{cases} \tag{3.3}$$

Here, a_d is the kernel normalization factor which equals $7/(478\pi h^2)$ and $3/(359\pi h^3)$ in 2D and 3D, respectively, $b = r_\mathbf{ij}/h$ and $r_\mathbf{ij} = |\vec{r_\mathbf{i}} - \vec{r_\mathbf{j}}|$, and κ is the coefficient that extends the smoothing length, where in this study we take $\kappa = 3$, and h as 4/3 times the initial distance between particles.

In a discrete form, one can simply replace integration in (3.1) with a summation over the particles of the domain as:

$$f_\mathbf{i} = \sum_{\mathbf{j}=1}^{J_n} \frac{1}{\psi_\mathbf{j}} f_\mathbf{j} W_\mathbf{ij}, \tag{3.4}$$

where, J_n is the number of neighbors in the support domain of particle $\mathbf{i}$, $f_\mathbf{i}$ could be either a scalar, vector or tensor value function. Furthermore, $d^3\vec{r_{\mathbf{j}}}$ in (3.1) is substituted with $\frac{1}{\psi_{\mathbf{j}}}$, where $\psi_{\mathbf{j}}$ denotes the number density and defined as:

$$\psi_{\mathbf{i}} = \sum_{\mathbf{j}=1}^{J_n} W_{\mathbf{ij}}. \tag{3.5}$$

As discussed in the previous chapter, equations that govern the complex systems include the first and second derivatives, requiring us to provide an SPH discretization of such terms. This task is possible upon substituting function $f(\vec{r_{\mathbf{j}}})$ by $\partial f(\vec{r_{\mathbf{j}}})/\partial x_{\mathbf{j}}^k$ in (3.1). After performing some mathematical manipulations, one may obtain the SPH discretization for the gradient of the arbitrary function f_i as:

$$\frac{\partial f_{\mathbf{i}}}{\partial x_{\mathbf{i}}^k} = \sum_{\mathbf{j}=1}^{J_n} \frac{1}{\psi_{\mathbf{j}}} f_{\mathbf{j}} \frac{\partial W_{\mathbf{ij}}}{\partial x_{\mathbf{i}}^k}. \tag{3.6}$$

However, this form of derivative discretization does not provide sufficient accuracy and hence requires SPH researchers to propose discretization schemes with higher accuracy. Benefiting from the properties of a second-rank isotropic tensor, we use the corrective SPH formulation to calculate the first-order derivative of a vector valued function f^s as follows (Shadloo, Zainali, Sadek & Yildiz, 2011):

$$\frac{\partial f_{\mathbf{i}}^s}{\partial x_{\mathbf{i}}^k} \alpha_{\mathbf{i}}^{kl} = \sum_{\mathbf{j}=1}^{J_n} \frac{1}{\psi_{\mathbf{j}}} \left(f_{\mathbf{j}}^s - f_{\mathbf{i}}^s \right) \frac{\partial W_{\mathbf{ij}}}{\partial x_{\mathbf{i}}^l}, \tag{3.7}$$

where where $\alpha_{\mathbf{i}}^{kl}$ is a second rank tensor. Similarly, the second-order derivative of f^s can be written as (Shadloo et al., 2011):

$$\frac{\partial}{\partial x_{\mathbf{i}}^k} \left(\xi_{\mathbf{i}} \frac{\partial f_{\mathbf{i}}^s}{\partial x_{\mathbf{i}}^k} \right) \alpha_{\mathbf{i}}^{sl} = 8 \sum_{\mathbf{j}=1}^{J_n} \frac{2}{\psi_{\mathbf{j}}} \left(\frac{\xi_{\mathbf{i}} \xi_{\mathbf{j}}}{\xi_{\mathbf{i}} + \xi_{\mathbf{j}}} \right) \left(f_{\mathbf{i}}^s - f_{\mathbf{j}}^s \right) \frac{r_{\mathbf{ij}}^s}{r_{\mathbf{ij}}^2} \frac{\partial W_{\mathbf{ij}}}{\partial x_{\mathbf{i}}^l}, \tag{3.8}$$

where ξ may denote any hydrodynamical or electrical properties. The term with ξ is important when dealing with the interface of the multiphase systems. The jump in the transport parameters must be treated precisely across the interface of multiphase systems. Such treatment is provided by applying the WHM[1] interpolation as follows:

$$\frac{2\xi_{\mathbf{i}}\xi_{\mathbf{j}}}{\xi_{\mathbf{i}}+\xi_{\mathbf{j}}}. \tag{3.9}$$

The alternative form is the following discretization scheme for laplacian term:

$$\frac{\partial}{\partial x_{\mathbf{i}}^{k}}\left(\xi_{\mathbf{i}}\frac{\partial f_{\mathbf{i}}^{s}}{\partial x_{\mathbf{i}}^{k}}\right)\left(2+a_{\mathbf{i}}^{kk}\right)=8\sum_{\mathbf{j}=1}^{J_n}\frac{2}{\psi_{\mathbf{j}}}\left(\frac{\xi_{\mathbf{i}}\xi_{\mathbf{j}}}{\xi_{\mathbf{i}}+\xi_{\mathbf{j}}}\right)\left(f_{\mathbf{i}}^{s}-f_{\mathbf{j}}^{s}\right)\frac{r_{\mathbf{ij}}^{k}}{r_{\mathbf{ij}}^{2}}\frac{\partial W_{\mathbf{ij}}}{\partial x_{\mathbf{i}}^{k}}. \tag{3.10}$$

This form is used to discretize (2.17) for the volume and the left hand sides of Eq.2.8, as well as pressure poison equation (i.e., (3.15)) which will be introduced later in this chapter.

It is now possible to discretize the governing equations of soft matter systems in the form of the SPH scheme using the Eqs. 3.4, 3.7, and 3.8. However, additional treatment should be considered when dealing with the incompressible flow and multiphase systems. These issues will be discussed in the following sections.

3.1.1 Treating multiphase system

In the SPH simulation of emulsion systems, interface tracking between the liquid phases is obtained by utilizing the color function $\hat{c}$. For a system with two different phases, for example, one phase is assigned as $\hat{c}=1$ while the other phase the color function is taken as $\hat{c}=0$, and these values remain unchanged during the entire simulation. To achieve a smooth and finite transition between phases and hence enhance the convergence and accuracy of the SPH, the initial color function is smoothed out for particles in the vicinity of the interface by using the following equation:

$$c_{\mathbf{i}}=\sum_{\mathbf{j}=1}^{J_n}\frac{\hat{c}_{\mathbf{j}}W_{\mathbf{ij}}}{\psi_{\mathbf{i}}}. \tag{3.11}$$

---

[1] Weighted Harmonic Mean

The smoothed color function, $c_{\mathbf{i}}$ is then used to calculate the interface features described in (2.3), including unit surface normal vector $\mathbf{n} = \boldsymbol{\nabla} c / |\boldsymbol{\nabla} c|$ and Dirac delta function $\delta \simeq |\boldsymbol{\nabla} c|$. This formulation, however, might result in erroneous normal vector in the calculation of surface tension force, which can be mitigated by applying constraints on the gradient of the smoothed color function. As suggested by Morris (2000), $|\boldsymbol{\nabla} c_{\mathbf{i}}| \geq \alpha / h$ constraint is used here, where, α is a numerical constant which is taken as $\alpha = 0.08$ to obtain reliable and accurate results (Tofighi & Yildiz, 2013).

Thermodynamic properties (e.g., ρ) and transport coefficients (e.g., σ, ε and μ) can experience a discontinuity across the interface of emulsions, thereby resulting in numerical instabilities. As described in (3.9), this problem can be solved by applying the average scheme. The alternative averaging approach is WAM[2] which utilized the color function and defined as:

$$\chi_{\mathbf{i}} = c_{\mathbf{i}} \chi_d + (1 - c_{\mathbf{i}}) \chi_f, \tag{3.12}$$

where subscripts d and f denote the distinct fluid phases, and χ represents any hydrodynamic or electrical fluid properties.

3.1.2 Imposing incompressibility

Various procedures are available in SPH for simulating incompressible flows. In this thesis, two distinct procedures are used for emulsion and active nematics: the first one is based on an artificial compressibility scheme, known as the WCSPH[3] method, and the second approach is the ISPH[4] method which is based on the pressure projection scheme. In the former procedure, an equation of State is employed by the weakly compressible SPH method which reads (Monaghan, 1994):

$$p_{\mathbf{i}} = \frac{\rho_0 c_0^2}{\gamma} \left[\left(\frac{\rho_{\mathbf{i}}}{\rho_0} \right)^{\gamma} - 1 \right], \tag{3.13}$$

---

[2] Weighted Arithmetic Mean

[3] Weakly Compressible SPH

[4] Incompressible SPH

where, c_0 is the speed of sound parameter, and γ is the specific heat-ratio, which is taken as 7. In this study, the value of c_0 is determined at each time step as 10 times of the maximum velocity in the domain in order to satisfy the incompressiblity condition, which is defined by the mach number as $M = (u/c) < 0.1$. The WCSPH approach provides the explicit solution for the momentum equation. However, it limits the time step size since the speed of sound parameter becomes the dominant velocity scale in the domain at the definition of the CFL[5] stability condition (Courant, Friedrichs & Lewy, 1928) for WCSPH.

Cummins and Rudmann have adapted the projection procedure developed by Chorin (1968) and implemented it in the SPH, which is known as the ISPH method (Cummins & Rudman, 1999).

3.1.3 Time integration and numerical treatments

In the WCSPH procedure, the modified Euler predictor-corrector time integration scheme (Ozbulut, Yildiz & Goren, 2014b) begins with the projection of intermediate particle velocities and positions with half time step size as $\mathbf{u}_\mathbf{i}^{n+1/2} = \mathbf{u}_\mathbf{i}^n + 0.5\mathbf{a}_\mathbf{i}^n \Delta t$ and $\mathbf{r}_\mathbf{i}^{n+1/2} = \mathbf{r}_\mathbf{i}^n + 0.5\mathbf{u}_\mathbf{i}^{n+1/2}\Delta t$, respectively, where n is the temporal index and Δt is the time step size. Due to the adopted time integration scheme, all the SPH interpolations to compute the material derivatives are performed at this projected particle setup. Therefore, it is sufficient to perform a neighbor search and particle pairing operation only at this stage of the time integration procedure. After establishing the connections and computing the values of kernel function $W_\mathbf{ij}$, its gradient $\boldsymbol{\nabla}_\mathbf{i} W_\mathbf{ij}$, number density $\psi_\mathbf{j}$, and all relevant pairing information between neighboring particles such as $\mathbf{r}_\mathbf{ij}$ and $\mathbf{u}_\mathbf{ij}$, the correction tensor $\alpha_\mathbf{i}^{kl}$ is also computed for each particle. Followingly, the continuity equation is solved, and the particle densities are projected by half time step size as $\rho_\mathbf{i}^{n+1/2} = \rho_\mathbf{i}^n + 0.5k_\mathbf{i}^{n+1/2}\Delta t$. Additionally, a density filtering treatment (Ozbulut, Ramezanzadeh, Yildiz & Goren, 2020) is implemented in order to maintain a smooth spatial density distribution in the domain:

$$\widehat{\rho}_\mathbf{i} = \rho_\mathbf{i} - \beta \frac{\sum_{\mathbf{j}=1}^{N} \left(\rho_\mathbf{i} - \rho_\mathbf{j}\right) W_\mathbf{ij}}{\sum_{\mathbf{j}=1}^{N} W_\mathbf{ij}} \tag{3.14}$$

---

[5] Courant-Friedrichs-Lewy

where $\widehat{\rho}_{\mathbf{i}}$ is the corrected density and β is a density smoothing coefficient which is used to eliminate spurious density variation, thereby enhancing the robustness of the algorithm without impairing the fidelity of the results. The value of β varies between zero and unity, and the value of unity corresponds to well known Shepard's interpolation. In this study, β is chosen to be equal to unity. Subsequently, the particle pressures are computed by the equation of state Eq.3.13.

In the ISPH method, the pressure distribution is found by solving the pressure Poisson equation with a source term being the divergence of the intermediate velocity as given in Eq.3.15. As a result, the pressure values can be obtained in a way that incompressibility conditions is enforced. To complete the time marching scheme, the velocities and then the positions of the particles are corrected via Eqs.3.16 and 3.17, respectively.

$$\nabla \cdot \left(\frac{1}{\rho_{\mathbf{i}}^{*}} \boldsymbol{\nabla} p_{\mathbf{i}}^{(n+1)} \right) = \frac{\boldsymbol{\nabla} \cdot \mathbf{u}_{\mathbf{i}}^{*}}{\Delta t'}, \tag{3.15}$$

$$\mathbf{u}_{\mathbf{i}}^{(n+1)} = \mathbf{u}_{\mathbf{i}}^{*} - \frac{1}{\rho_{\mathbf{i}}^{*}} \boldsymbol{\nabla} p_{\mathbf{i}}^{(n+1)} \Delta t', \tag{3.16}$$

$$\mathbf{r}_{\mathbf{i}}^{(n+1)} = \mathbf{r}_{\mathbf{i}}^{(n)} + \frac{1}{2} \left(\mathbf{u}_{\mathbf{i}}^{(n)} + \mathbf{u}_{\mathbf{i}}^{(n+1)} \right) \Delta t' + \boldsymbol{\delta} \mathbf{r}_{\mathbf{i}}^{(n)}. \tag{3.17}$$

The APD[6] correction algorithm (Shadloo et al., 2011) is applied upon the finalization of the time step, in order to eliminate instabilities that are originated from particle clustering and particle fractures:

$$\delta \mathbf{r}_{\mathbf{i}} = \sum_{\mathbf{j}=1}^{N} \frac{\mathbf{r}_{\mathbf{ij}}}{r_{\mathbf{ij}}^{3}} r_0^2 u_v \Delta t \tag{3.18}$$

Here, $\delta \mathbf{r}_{\mathbf{i}}$ is the corrected particle position, $u_v = \left| \sum_{\mathbf{j}=1}^{N} \left(\mathbf{u}_{\mathbf{i}} - \mathbf{u}_{\mathbf{j}} \right) W_{\mathbf{ij}} \right| / \sum_{\mathbf{j}=1}^{N} W_{\mathbf{ij}}$ is the velocity variance based APD coefficient (Ozbulut et al., 2017) and $r_0 = \sum_{\mathbf{j}=1}^{N} r_{\mathbf{ij}} / N$ is the average neighbor distance of the particle $\mathbf{i}$.

---

[6] Artificial Particle Displacement

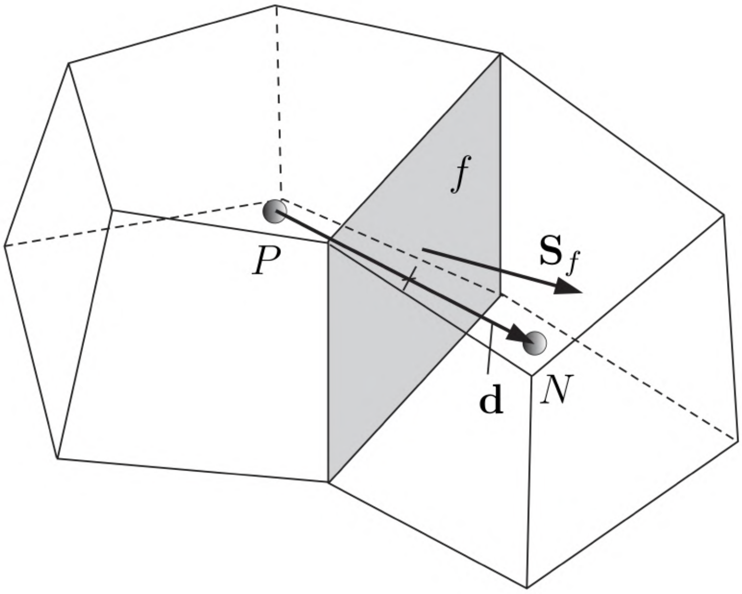

Figure 3.2 **Parameters in FVM discretization.** Cell centroids are denoted by P and N and $\mathbf{d}$ representing the distance between two centroids. The boundary face f is located between two cells with S being its normal surface area vector (The image from OpenFOAM (2011).)

3.2 Finite Volume Scheme

OpenFOAM utilizes finite volume discretization, which has been described by many researchers (Ferziger, Perić & Street, 2002; Patankar, 2018; Versteeg & Malalasekera, 2007; Weller et al., 1998). Thus, we present a concise review of this scheme in this section. After that, we describe the VoF[7] method which is used to model the multiphase flow in the simulation of emulsions.

3.2.1 FVM discretization

Similar to the SPH algorithm, three discretization procedures should be performed in FVM, including domain, equations, and temporal discretization. Unlike the glssph method, FVM utilizes the Eulerian grid to discretize the domain on which the PDEs are subsequently discretized. Time discretization, if required, is performed

---

[7] Volume of Fluid

by breaking it into a set of time steps Δt that may change during a numerical simulation, perhaps depending on some condition calculated during the simulation. Concretely, space discretization requires subdividing the domain into a number of cells, known as control volumes. These cells are contiguous, i.e. they do not overlap one another and completely fill the domain (Fig. 3.2). Dependent variables and other properties are stored at the cell centroid P. The cell is bounded by a set of flat[8] faces, given the generic label f. The cell faces are divided into two groups - internal faces (between two cells) and boundary faces, which coincide with the boundaries of the space domain. In the present study, the connectivity between cells is such that the cells adjacent to a given cell face are identified by the indices, and the cell edges form continuous mesh lines that begin and end on opposite cell faces. This kind of mesh is often referred to as *structured mesh.* The advantage of such a mesh is that the cell centroid can be easily addressed by double indices (i,j) in two dimensions.

The purpose of equation discretization is to convert the PDEs into a system of algebraic equations, making it possible to solve them numerically. Considering the generic form of the standard transport equation for any tensorial quantity ϕ (OpenFOAM, 2011):

$$\underbrace{\frac{\partial \rho\phi}{\partial t}}_{\text{time derivative}} + \overbrace{\boldsymbol{\nabla}\cdot(\rho\mathbf{U}\phi)}^{\text{advection term}} = \underbrace{\boldsymbol{\nabla}\cdot(\Gamma_\mu \boldsymbol{\nabla}\phi)}_{\text{diffusion term}} + \overbrace{\mathbf{S}_\phi(\phi)}^{\text{source term}}, \tag{3.19}$$

where $\mathbf{U}$ is velocity, Γ_μ is the diffusivity and $\mathbf{S}_\phi(\phi)$ denotes the source term. To discretize (3.19) based on the FVM, one needs to integrate the whole equation over the control volume V and time. Most spatial derivative terms are then converted to integrals over the cell surface S bounding the volume using the generalized form of the Gauss's theorem. The Laplacian term in (3.19) is integrated over a control volume and linearized as follows (OpenFOAM, 2011):

$$\int_V \boldsymbol{\nabla}\cdot(\Gamma_\mu \boldsymbol{\nabla}\phi)dV = \int_S d\mathbf{S}\cdot(\Gamma_\mu \boldsymbol{\nabla}\phi) = \sum_f (\Gamma_\mu)_f \mathbf{S}_f \cdot (\boldsymbol{\nabla}\phi)_f, \tag{3.20}$$

where S is the surface area vector, and subscript f denotes the surface index. In the present study, the length vector d between the center of the cell of interest P and

---

[8] For a flat face, all vertices lie in one plane.

the center of a neighboring cell N is orthogonal to the face plane (i.e., $\mathbf{d}$ is parallel to s_f). In such condition, the face gradient discretization is implicit and can be calculated as follows (OpenFOAM, 2011):

$$\mathbf{S}_f \cdot (\boldsymbol{\nabla}\phi)_f = |S_f| \frac{\phi_N - \phi_P}{\mathbf{d}}. \tag{3.21}$$

Similarly, the advection term is discretized as follows (OpenFOAM, 2011):

$$\int_V \boldsymbol{\nabla} \cdot (\rho \mathbf{U} \phi) dV = \int_S d\mathbf{S} \cdot (\rho \mathbf{U} \phi) = \sum_f \mathbf{S}_f \cdot (\rho \mathbf{U})_f \phi_f. \tag{3.22}$$

The face field ϕ_f can be evaluated using a variety of schemes, including CD[9], UD[10], and BD[11] (OpenFOAM, 2011).

The first time derivative is discretised by simple differencing in time using either Euler implicit or Backward differencing scheme (OpenFOAM, 2011). In addition to these terms, the divergence and the gradient terms are respectively discretized as follows (OpenFOAM, 2011):

$$\int_V \boldsymbol{\nabla} \cdot \phi dV = \int_S d\mathbf{S} \cdot \phi = \sum_f \mathbf{S}_f \cdot \phi_f, \tag{3.23}$$

$$\int_V \boldsymbol{\nabla} \phi dV = \int_S d\mathbf{S} \phi = \sum_f \mathbf{S}_f \phi_f. \tag{3.24}$$

where the form in (3.24) known as Gauss integration scheme, while other scheme also available in OpenFOAM such as least squares method and surface normal gradient scheme.

In order to guarantee the method stability, CFL condition is applied for each cell as

---

[9] Central Differencing

[10] Upwind Differencing

[11] Blended Differencing

follows (Courant et al., 1928; Ferziger et al., 2002):

$$\max_i C_i = \max_i \Delta t \frac{1}{2V_i} \sum_{f \in \partial V_i} |\varphi_f| \leq C_{max}, \tag{3.25}$$

where, C_{max} is the Courant number limit and in the OpenFOAM the typical value is $C_{max} = 1$, and $\varphi_f = \mathbf{S}_f \cdot \mathbf{u}$ denotes the volumetric flux through the face f.

3.2.2 The VoF method

The multiphase flow solver is incorporated in OpenFOAM and known as *interFoam* which is a two-phase incompressible flow solver (Deshpande, Anumolu & Trujillo, 2012). This solver uses the VoF method to simulate the dynamics of fluid-fluid interfaces. Based on the concept of color function, VoF introduces the volume fraction of fluid i (whereas in two phase, it could be either 1 or 2) as follows:

$$\alpha_i = \frac{\text{volume of fluid } i \text{ in the cell}}{\text{total volume of the cell}}, \tag{3.26}$$

where α_i may vary from 0 to 1. In a two-phase system, one can drop the subscript i such that $\alpha = 1$ corresponds to the cell entirely filled by fluid 1, while $\alpha = 0$ indicates that the cell is filled by fluid 2. Moreover, the intermediate values of α define a diffuse interface between the two fluids. At each time step, α is advected with the fluid following equation (Deshpande et al., 2012):

$$\frac{\partial \alpha}{\partial t} + \boldsymbol{\nabla} \cdot (\alpha \vec{u}) = 0. \tag{3.27}$$

However, utilizing (3.27) results in a numerical diffusion that increases the diffuse interface thickness throughout the simulation and subsequently, destroys the sharp interface. To limit the numerical interface smearing, (3.27) is modified by adding an artificial compression velocity term (Ubbink & Issa, 1999) as:

$$\frac{\partial \alpha}{\partial t} + \boldsymbol{\nabla} \cdot (\alpha \vec{u}) - \boldsymbol{\nabla} \cdot (\alpha(1-\alpha)\vec{u}_c) = 0, \tag{3.28}$$

where, $vecu_c$ denotes the artificial compression velocity. The artificial compression velocity term acts only in the vicinity of the interface and in the direction normal to it. Upon finding the volume fraction field, density and viscosity are obtained via (3.12) substituting $c_{\mathbf{i}}$ by α. Consequently, surface normal vectors and surface tension forces can be calculated as discussed in Secs. 2.1.1 and 3.1.1.

4. Electrohydrodynamics of a single emulsion in a highly confined domain

4.1 Introduction

In the present chapter, the deformation of a highly confined 2D Leaky dielectric droplet under the applied electric field will be simulated using ISPH. To see the impacts of electrical property ratios, six different systems of fluids will be employed. All the two main components of the electrical force will be calculated on the droplet interface and their influence on the droplet deformation will be discussed thoroughly considering their both magnitude and sign. Furthermore, the pressure field will be calculated inside the domain and its effect on the droplet deformation, particularly at the high confinement ratio will be discussed. In order to facilitate the analysis, a new parameter, namely the force ratio, will be introduced and applied on the droplet interface to evaluate the influences of all related forces on the droplet deformation. Additionally, it will be shown that the analytical results are not reasonable at high confinement ratios, while our numerical method is able to calculate the physical and justifiable deformation values at high confinement ratios.

4.2 Problem statement

This chapter is a slightly modified version of "Electrohydrodynamics of a droplet in a highly confined domain: A numerical study" published in "Physics of Fluids" by "R. Saghatchi, A. Rahmat, and M. Yildiz".

Dimensionless values are formed using the following scales

$$\begin{aligned}
&\mathbf{x} = \mathbf{x}^{+}/r, \quad \rho = \rho^{+}/\rho_d, \quad \mu = \mu^{+}/\mu_f \quad \mathbf{u} = \mathbf{u}^{+}/\left(d/t^{+}\right),\\
&t = t^{+}/\left(d/\left|\mathbf{u}_c\right|\right), \quad p = p^{+}/\rho_d\left(\left|\mathbf{u}_c\right|\right)^2,\\
&\mathcal{D} = \rho_d/\rho_f, \quad \mathcal{V} = \mu_d/\mu_f, \quad \mathcal{P} = \varepsilon_d/\varepsilon_f, \quad \mathcal{C} = \sigma_d/\sigma_f,
\end{aligned} \tag{4.1}$$

leading to Reynolds, Weber, Electro-Weber and electrical capillary numbers defined as

$$\mathrm{Re} = \frac{\rho_d\left|\mathbf{u}_c\right|d}{\mu_d}, \quad \mathrm{We} = \frac{\rho_d\left|\mathbf{u}_c\right|^2 d}{\gamma}, \quad \mathrm{Ew} = \frac{\rho_d\left|\mathbf{u}_c\right|^2}{\varepsilon_d E_\infty^2}, \quad \mathrm{Ec} = \frac{\mathrm{We}}{\mathrm{Ew}} = \frac{\varepsilon_d E_\infty^2 d}{\gamma}. \tag{4.2}$$

Here $\mathbf{u}_c = \varepsilon_d E_\infty^2 d/\mu_d$ is characteristic velocity, in which d and E_∞ are the droplet diameter, and electric field intensity respectively. Superscript $+$ denotes dimensional variables whereas subscripts f and d refer to background fluid and droplet phases, respectively. Governing equations are solved using SPH method.

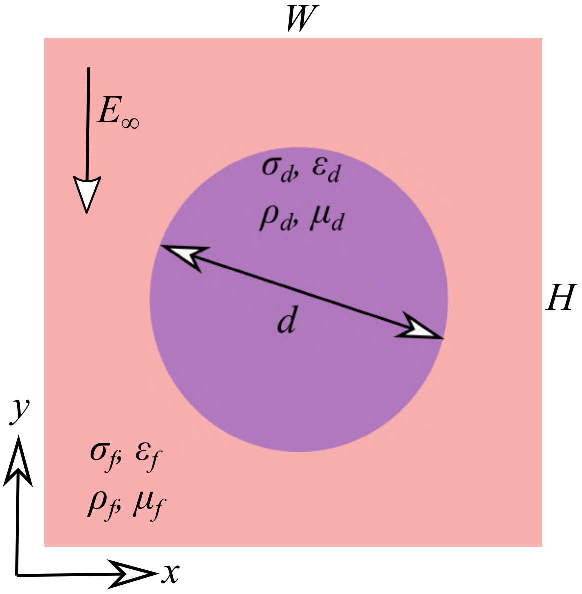

Figure 4.1 **Schematic representation of the physical setup.** The physical domain includes a suspended droplet with the initial diameter d in an ambient fluid under the constant electric field applied in the downward direction.

The computational domain is shown in Fig.5.1 which consists of a 2D droplet with diameter d suspended in an ambient fluid inside a confined square domain assuming $W = H$. The confinement ratio is defined as the ratio of droplet diameter to the domain length, $Wc = d/H$. A uniform electric field E_∞ is applied in the downward direction. It is assumed that no gravitational force is applied and there is no relative motion between droplet and ambient fluid initially. No-slip boundary condition is applied on all side boundaries to imitate the confined domain. Considering the

Table 4.1 The ratio of the material properties which is used to prove the code accuracy and also resolution dependency test.

System	$\mathcal{P}$	$\mathcal{C}$	$\mathcal{D}$	$\mathcal{V}$
Prolate	0.5	2.0	1	1
Oblate	5.0	0.2	1	1

electric field, Dirichlet and Neumann boundary conditions are applied for horizontal and vertical walls, respectively. All particles inside and outside the droplet are arranged using a uniformly spaced Cartesian grid.

4.3 Numerical consistency and accuracy studies

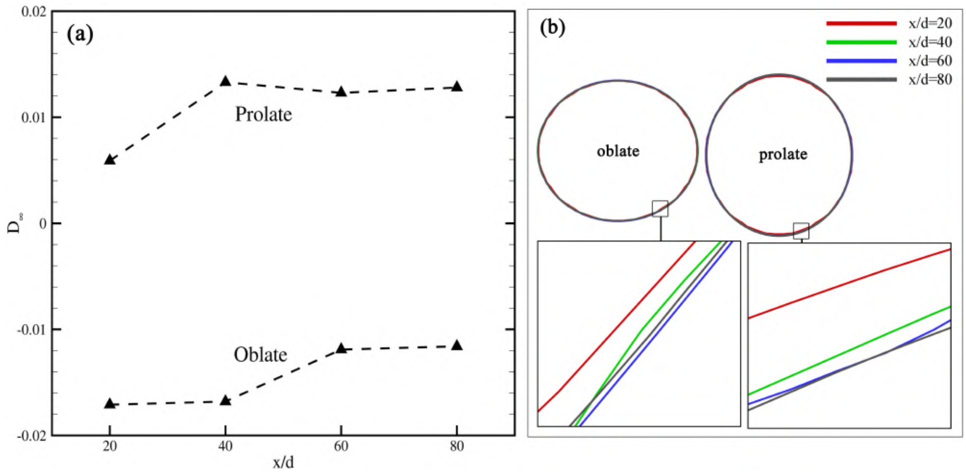

Figure 4.2 **Effect of particle resolution on the droplet deformation.** Results are obtained in $Wc = 0$ and $Ec = 0.02$. (a) quantitative result, and (b) qualitative result.

Considering the leaky dielectric model, the droplet may deform into two distinct configurations forming prolate or oblate shapes. The prolate shape is achieved when the droplet elongates in the direction of the applied electric field, while the transverse elongation of the droplet is known as oblate deformation. To check the dependency of numerical results with respect to particle resolution, the deformation of the droplet in an unbounded domain i.e. $Wc = 0$ is simulated for both prolate and oblate cases at $Ec = 0.02$. Fluid properties of the respective cases are tabulated in Tab.4.1. The simulations are performed for different values of particle resolution $x/d = 20, 40, 60,$ and 80, where x/d is the number of particles per unit of droplet's initial diameter.

The deformation of the droplet can be characterized as

$$D = \frac{l_1 - l_2}{l_1 + l_2}, \tag{4.3}$$

where l_1 and l_2 are the two main axes of the deformed droplet in the directions parallel and perpendicular to the applied electric field, respectively. So, positive and negative values calculated by (4.3) represent prolate and oblate deformations, respectively. It should be noted that for the unbounded domain, Wc is considered to be small enough such that the effect of boundaries is negligible as shown in our previous studies (see for example (Shadloo et al., 2013)).

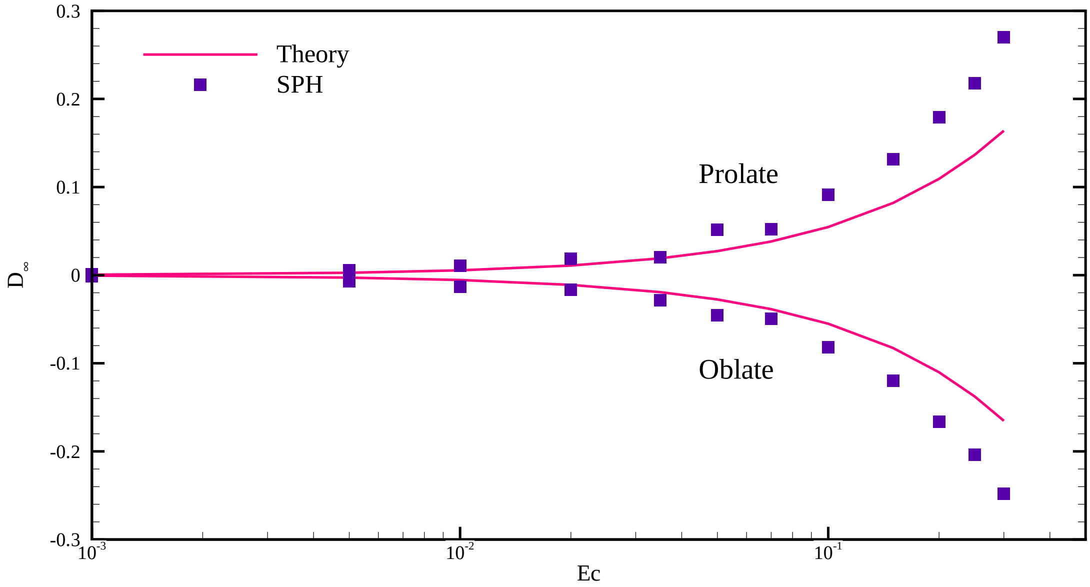

Figure 4.3 **Validation of current code for the EHD problem.** The comparison of the droplet deformation between our numerical simulation and analytical data of Feng & Scott (1996) for $Wc = 0$ and different amounts of Ec.

The steady-state deformation of the droplet is represented in Fig. 5.2 for different resolutions. Qualitative and quantitative comparison of the results in Fig. 5.2 indicates that increasing the resolution from $x/d = 20$ to 40 and from $x/d = 40$ to 60 shows improvement in the accuracy of the results. However, no significant improvement has been observed from $x/d = 60$ to 80, so $x/d = 60$ is considered as the reference particle resolution.

Validation test has been performed through simulating the droplet deformation under the effect of the electric field in an unbounded domain. To achieve this, two prolate and oblate systems based on the properties of Tab. 4.1 are modeled under various electrical capillary numbers Ec. The effect of the electrical capillary number on the droplet deformation is shown in Fig. 5.3 and is compared with the analytical results of Feng & Scott (1996). Feng and Scott used the following equation for calculating the deformation of the droplet as

$$D = \frac{f_d E_\infty^2 \varepsilon_d (d/2)}{3(1+\mathcal{C})^2 \mathcal{P}\gamma}, \tag{4.4}$$

where f_d is the discriminating function defined as:

$$f_d = \mathcal{C}^2 + \mathcal{C} + 1 - 3\mathcal{P}. \tag{4.5}$$

As it is shown in Fig. 5.3, our results perfectly match with the analytical data for small deformations ($|D_\infty| < 0.05$). For larger deformations, however, it is observed that the numerical data deviates from the analytical data. This is due to the assumptions made in the theory which considers the droplet to remain almost circular. Thus, the analytical predictions are only valid for small deformations. Such observations have been frequently reported by other numerical studies (see for example (Roghair et al., 2015; Shadloo et al., 2013; Zhang & Kwok, 2005)).

4.4 Results

Here, the EHD deformation of a single droplet in a confined domain is presented by considering six different systems of fluids, as tabulated in Tab.5.1. The properties of the first four systems are selected from experiments in micro- and bio-fluidics applications. The properties of the other two systems are chosen hypothetically to illustrate all possible forms of droplet deformation which will be thoroughly discussed. These fluid systems are selected such that they represent the electric conductivity of the droplet to be smaller (systems II and VI), in the same order (systems I, III, and V), and larger (system IV) than the ambient fluid. Since the deformation of droplets is limited to the confined characteristics of the domain, the electric capillary number is chosen such that the unbounded deformation of the respective systems is relatively small and equal to $|D_\infty| = 0.05$, unless stated otherwise.

Figure 4.4 represents the deformation of the droplet normalized with respect to

Table 4.2 Dielectric properties that are used in this study. Data are taken from (Tsukada et al., 1994), (Allan et al., 1962), and (Hunt et al., 2009).

System	Ambient fluid	$\sigma_f(\frac{S}{m})$	$\varepsilon_f(\frac{F}{m})$	Droplet fluid	$\sigma_d(\frac{S}{m})$	$\varepsilon_d(\frac{F}{m})$	$\mathcal{C}$	$\mathcal{P}$	Reference
I	silicon oil 1	2.67×10^{-12}	2.66	corn oil	1.06×10^{-11}	3.24	3.9700	1.2180	(Tsukada et al., 1994)
II	oxidized castor oil	1.0×10^{-9}	6.3	silicone oil 5000	3.33×10^{-11}	2.77	0.0333	0.4397	(Allan et al., 1962)
III	corn oil	1.06×10^{-11}	3.24	silicon oil 1	2.67×10^{-12}	2.66	0.2519	0.8210	(Tsukada et al., 1994)
IV	medium	1.8×10^{-2}	80	cytoplasm	0.5	75	27.7778	0.9375	(Hunt et al., 2009)
V	hypothetical	-	-	hypothetical	-	-	1.0	0.2	-
VI	hypothetical	-	-	hypothetical	-	-	0.02	0.1	-

the unbounded deformation for the systems in Tab.5.1. In this figure, the present numerical data is further compared with the theoretical results of Behjatian & Esmaeeli (2013). They have introduced an analytical solution for a confined droplet in circular domains by

$$D = \frac{\mathrm{Ec}}{3}\frac{\Gamma^2\Phi}{(\mathcal{C}+1)^2}, \tag{4.6}$$

where

$$\Gamma = \frac{\mathcal{C}+1}{(\mathcal{C}+1) - Wc^2(\mathcal{C}-1)}, \tag{4.7}$$

and

$$\Phi = \mathcal{C}^2 + 1 - 2\mathcal{P} + \mathcal{F}(\mathcal{C}-\mathcal{P}), \tag{4.8}$$

in which $\mathcal{F}$ is a characteristic function. Interested readers may refer to Behjatian & Esmaeeli (2013) for further information.

Equation (4.6) shows that for small confinement ratios ($Wc < 0.4$), the normalized deformation does not represent significant variations. At larger confinement ratios, however, the deformation changes significantly in most cases. It is observed that for some of the systems, the droplet elongation shifts from oblate to prolate or vice versa. This behavior can be justified considering the variation in the magnitude and direction of electrical and hydrodynamic forces on the interface.

It is revealed that for small to moderate values of confinement ratio, i.e, $Wc < 0.6$, the present numerical method and the analytical solution produce similar results. However, our numerical results deviate from the theory at large confinement ratios. Considering the asymptotic behavior of the theoretical results for some of the presented systems, one can easily conclude that this cannot be valid due to the small and limited characteristic of a confined droplet deformation. Additionally, in some systems, the droplet might reach the boundaries and the corresponding deformation becomes undefined. The deformation of system IV, for instance, cannot be obtained beyond $Wc = 0.6$, since the droplet reaches the top and bottom boundaries. Thus, the analytical solution is only limited to small ranges of confinement ratio while our SPH method can predict reasonable values for large confinement ratios, and

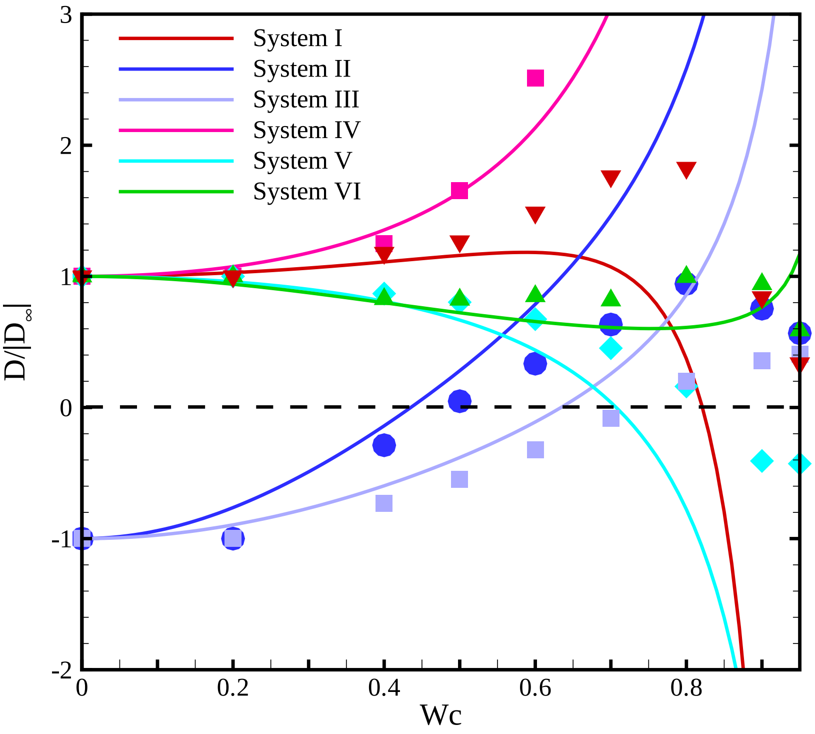

Figure 4.4 **Variation of deformation which is normalized with the deformation at $Wc = 0$ with respect to the confinement ratio.** Solid lines demonstrate the analytical solution of Behjatian & Esmaeeli (2013) and points represent the SPH results.

corresponding values of deformation are limited and physically justifiable as shown in Fig. 4.4.

It can be shown that the hydrodynamics of the systems depends on the sign of $\mathcal{P} - \mathcal{C}$ such that the droplet and ambient fluids may circulate accordingly (Shadloo et al., 2013). So, systems V and II are chosen which correspond to the $\mathcal{P} < \mathcal{C}$ and $\mathcal{P} > \mathcal{C}$ respectively to scrutinize the confinement effect on the characteristics of the flow. Figure 4.5- a and c demonstrates the streamlines for these systems at four different confinement ratios of $Wc = 0.6, 0.7, 0.8$ and 0.9. Due to the symmetric nature of the problem in x and y directions, only a quarter of the domain is shown. In each quarter, the flow consists of a pair of vortices inside and outside of the droplet, circulating in opposite directions since they match with their counterpart. For system II, outside velocities run from the left and the right ($\theta = 0$ and π) towards the top and the bottom ($\theta = \pi/2$ and $3\pi/2$), which leads to the droplet elongation in the x-direction (oblate shape) in an unbounded domain. For system V, ambient velocities run from the top and the bottom ($\theta = \pi/2$ and $3\pi/2$) towards the left and the right ($\theta = 0$ and π) as shown in Fig. 4.5, resulting in elongation of the droplet

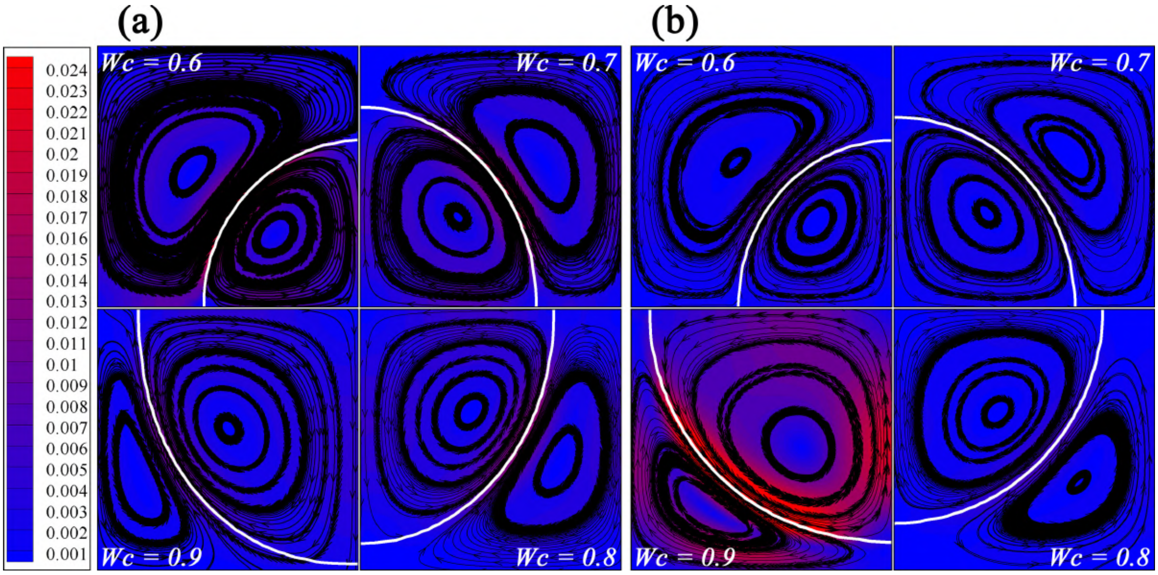

Figure 4.5 **Streamlines and magnitude of velocity contours.** Results are shown for (a) system II and (b) system V at various values of Wc. Due to symmetry in x- and y- directions, only a quarter of the domain is shown.

in the y-direction (prolate shape) in small confinement ratios. At large confinement ratios, however, the deformation of these two systems shifts from prolate to oblate and vice versa. Nevertheless, by increasing the confinement ratio the circulation direction of the vortices at the interior and exterior regions is not changed. Thus, the change in the deformation due to the confinement ratio variation cannot be justified by considering the vortex structure only. Therefore, it is needed to analyze the electrical and hydrodynamic forces on the interface of the droplet to investigate the reason for the deformation variation, precisely.

Santra et al. investigated the effect of confinement ratio on the magnitude of velocity on a line passing through the center of the droplet (Santra et al., 2018). To see the effect of confinement ratio on the velocity magnitude of the entire domain, contours of this parameter are calculated and plotted in Fig. 4.5-a and b for systems II and V, respectively, at various amounts of confinement ratios. As shown in this figure, by increasing the confinement ratio for system II, velocity magnitude reacts inversely and its value decreases inside the domain, which is consistent with the results from Santra et al. (2018). In contrast to system II, velocity magnitude increases by increasing the confinement ratio for system V as shown in Fig. 4.5-b. As it is demonstrated in this figure, the velocity magnitude is relatively high at the top and bottom sides of the droplet at $Wc = 0.9$ which can prove the reason for the oblate deformation of system V at high confinement ratios. However, a detailed investigation of the competing interfacial forces is needed which will be provided in the following.

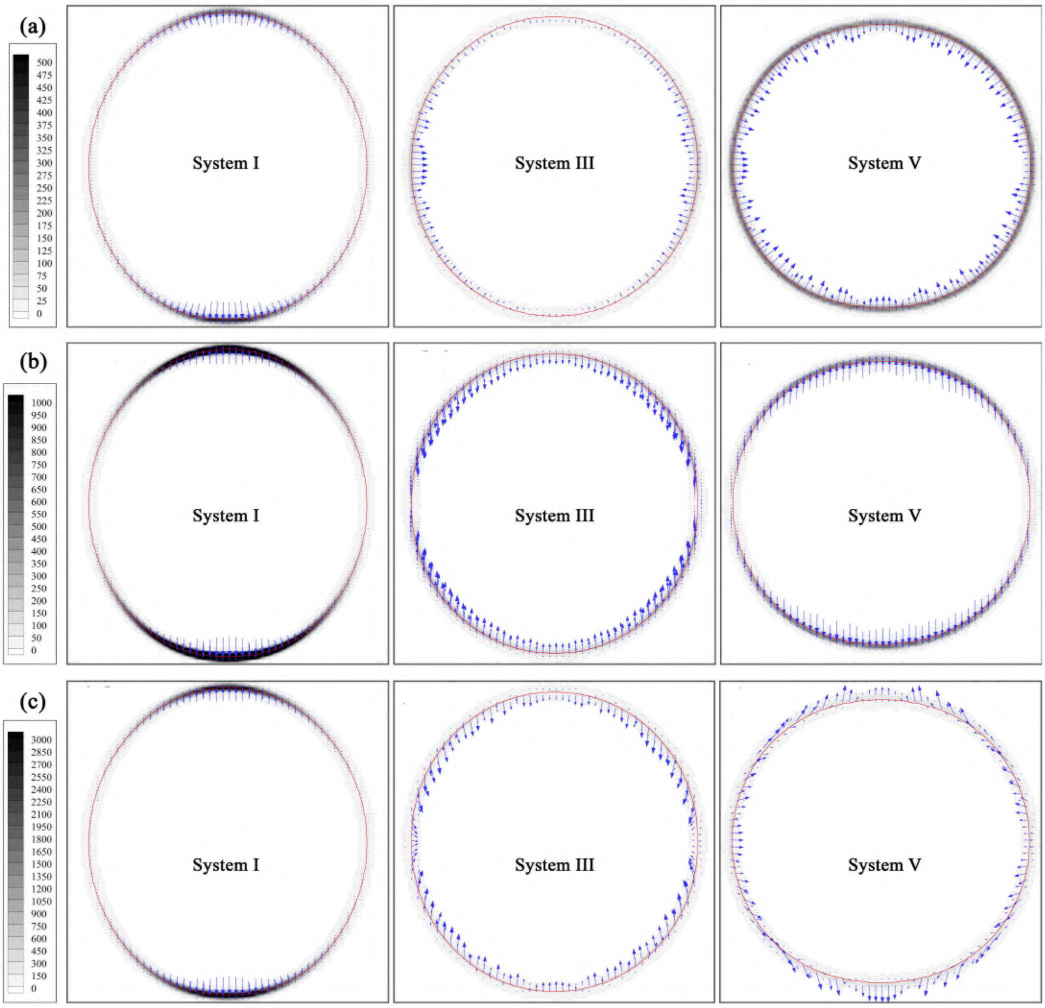

Figure 4.6 **Electric forces on the interface.** Comparison of (a) polarization force, (b) Coulomb force, and (c) total electric force on the interface of the droplet at $Wc = 0.9$ for systems I, III and V.

Figure 4.6 represents the polarization (a), the Coulomb (b), and the total (c) electric forces by showing their direction and magnitude on the droplet interface for systems I, III, and V at $Wc = 0.9$. These three systems are selected since they represent different behavior due to different electric force configurations. It can be easily concluded that the polarization force acts normal to the interface in the opposite direction of the electrical permittivity gradient, while the direction of the Coulomb force depends on the interplay between the electric field and the electrical surface charges. Considering Fig. 4.6-a, the polarization force stretches the droplet into a prolate shape by acting at the top and bottom poles of the droplet in system I. In system III, the effect of the polarization force is more pronounced at the side of the droplet direction inwards, while system V shows an almost constant distribution of the polarization force across the interface towards the center of the droplet. Figure 4.6-b shows that the Coulomb force acts mainly parallel to the applied electric field vertically, representing an outward direction for systems I and V, in contrast to system III. By comparing the magnitude of the polarization and Coulomb force terms, Fig. 4.6-c shows the effect of the total electric force for these three systems. For the system I, the Coulomb and polarization forces are in the same direction acting at the top and bottom poles, magnifying their effect. For the system III, the Coulomb force is much stronger than the polarization force, thus it dominates the total electric force influence. For system V, the polarization and Coulomb forces act in opposite directions especially at the top and bottom parts of the droplet. The interplay between these two terms results in an inward contribution from the polarization force at the side of the droplet and an outward effect at the top and bottom due to the stronger Coulomb force. It should be noted that the electric force configurations of system II and VI are the same as III, so they are not represented here for the sake of brevity. Additionally, the polarization and Coulomb forces act on the top and bottom poles toward and outward the center respectively for system IV, while the magnitude of the Coulomb force is greater than the polarization force. Hence, the total electric force stretches the droplet in a vertical direction similar to the system I, as shown in Fig. 4.7-a and c.

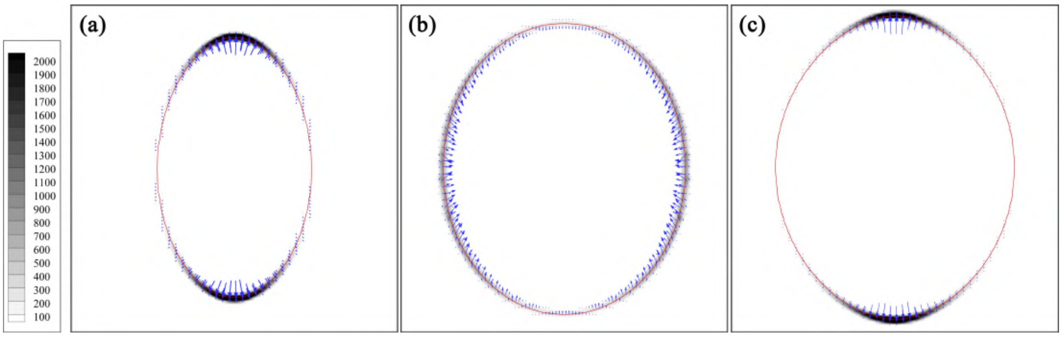

Figure 4.7 **Total electric force on the interface of the droplet.** Results are shown for (a) system IV at $Wc = 0.6$ and $|D_\infty| = 0.05$, (b) system II at $Wc = 0.8$ and $|D_\infty| = 0.05$, and (c) system IV at $Wc = 0.8$ and $|D_\infty| = 0.01$.

Recalling from Fig. 4.4, $|D_\infty|$ is set to 0.05 for all systems and the $D/|D_\infty|$ is evaluated up to $Wc = 0.95$. On the other hand, it can be observed from the analytical results shown in 4.4 that systems II and IV tend to reach very large deformations at high confinement ratios (i.e. $Wc > 0.7$). However, we observe that systems II and IV behave differently under the EHD effects. The discrepancy is due to different electric force field configurations on the droplet interface. Figure 4.7 represents the deformation of systems II and IV and illustrates the electric force vectors and their magnitude on the interface. It can be clearly seen in Fig. 4.7-a that the electric forces act at the top and bottom poles of the droplet in system IV and elongate it into a prolate shape while the cause for the deformation of system II is the inward electric forces at the side poles of the droplet as shown in Fig. 4.7-b. Additionally, the magnitude of the electric forces is much larger in system IV. This results in large droplet deformations at relatively smaller confinement ratios where the droplet reaches the top and bottom boundaries at $Wc > 0.6$. In order to represent the deformation of system IV at larger confinement ratios, the unbounded deformation has been changed from $|D_\infty| = 0.05$ to $|D_\infty| = 0.01$ which corresponds to the smaller electrical capillary number. Hence, this indicates that the applied electric force is weaker on the droplet interface leading to smaller unbounded deformations. Under this condition, the droplet deformation of system IV can be tracked up to large confinement ratios i.e. $Wc = 0.8$ reaching $D/|D_\infty| = 6.96$ as represented in Fig. 4.7-c. This shows that the analytical solution predicts the deformation of system IV correctly only at very small unbounded deformations. For system II, however, the analytical solution does not represent accurate results at large confinement ratios.

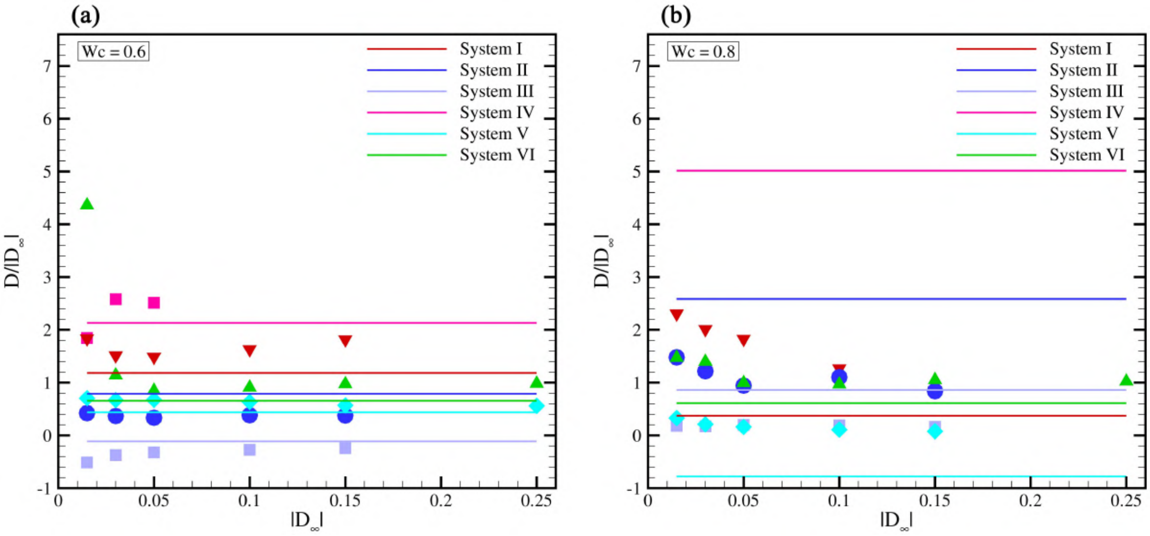

Figure 4.8 **Effect of unbounded deformation on the variation of normalized droplet deformation.** (a) $Wc = 0.6$, and (b) $Wc = 0.8$. Solid lines demonstrate the results of Behjatian & Esmaeeli (2013) and points represent the SPH results.

In Fig. 4.7, it is shown that the value of the unbounded deformation (e.g. in system IV) affects the predictions at large confinement ratios and results in different $D/|D_\infty|$. In order to analyze this effect, Fig. 4.8 represents the $D/|D_\infty|$ at two confinement ratios (a) $Wc = 0.6$ and (b) $Wc = 0.8$ for all six systems in Tab. 5.1 as a function of $|D_\infty|$, which can be interpreted as an effect of the applied electric field strength. At $Wc = 0.6$, it is observed that the analytical solution provides relatively accurate results for all systems. For systems II and V, the variation of the unbounded deformation does not show a considerable effect on $D/|D_\infty|$ while it is observed that for systems III and VI, the analytical solution predicts more accurate results at large unbounded deformations. On the other hand, the variations of systems I and IV do not indicate a meaningful relationship. At $Wc = 0.8$, systems I and VI represent an approaching trend as the unbounded deformation increases, in contrast to system II, while systems III and V do not show remarkable sensitivity to the variations of unbounded deformation. For system IV, there is no available data at this confinement due to the extreme action of the electric forces by which the droplet reaches the top and bottom boundaries at very small unbounded deformations (i.e. $D_\infty < 0.02$). By analyzing the data, one may notice that the analytical solution is accurate at small and moderate confinement ratios ($Wc \leq 0.6$) which confirms our previous conclusion. For the high confinement ratios, on the other hand, high unbounded deformation should be selected to making analytical solutions applicable. Otherwise, there will be a difference between analytical and numerical results. The reason behind such difference is due to the existence of complex interactions and the interplay between electrical and hydrodynamic forces that we aim to elaborate for some of the systems in the following.

Recalling from Fig. 4.4, one can notice that the general trend of systems I and V are similar except the difference in numerical results at large confinement ratios. It should be noted that for both systems I and V, the comparison of the electrical conductivity and permittivity ratios yields $\mathcal{P} < \mathcal{C}$. So, the inner and outer vortices around the droplet are as described in Fig. 4.5-b. Additionally, the electric forces on the interface tend to deform the droplet into a prolate shape as shown in Fig. 4.6-a to c, as observed for both cases at small confinement ratios. In contrast, the electrical conductivity and permittivity ratios of systems II and III result in $\mathcal{P} > \mathcal{C}$, so it is expected that they deform into an oblate shape as seen in small confinement ratios. However, the deformations of these two systems represent a shift from oblate to prolate deformation at large confinement ratios. In order to explain the above-mentioned cases, other dominating terms such as pressure should be also considered which can highly influence the hydrodynamics of microfluidic systems. We believe that the reason for such discrepancies is inherited in inappropriate utilization of the pressure term in the analytical solution. In the following, it will be shown how the pressure dominates the flow and changes the hydrodynamics of the system. This will be represented in Fig. 4.9 by comparing the dynamics of systems I and V, as well as in Fig. 4.10 for systems II and III.

Figure 4.9 compares the electrical and pressure forces for systems I and V. In Fig. 4.9-a, a new parameter is introduced here namely the Force Ratio (FR), which is the ratio of forces normal to the interface at the sides and top/bottom poles of the droplet. The FR is defined such that if $FR > 1$, interfacial forces deform the droplet into a prolate shape, while $FR < 1$ leads to an oblate elongation. Figure 4.9-b and c represent the contours of the pressure and the electric force vectors of systems I and V at $Wc = 0.6$, 0.8, and 0.95, respectively. It is observed that system I remains prolate at all confinement ratios, while system V shifts in an oblate deformation at large confinement ratios. Considering FR of the system I, both polarization

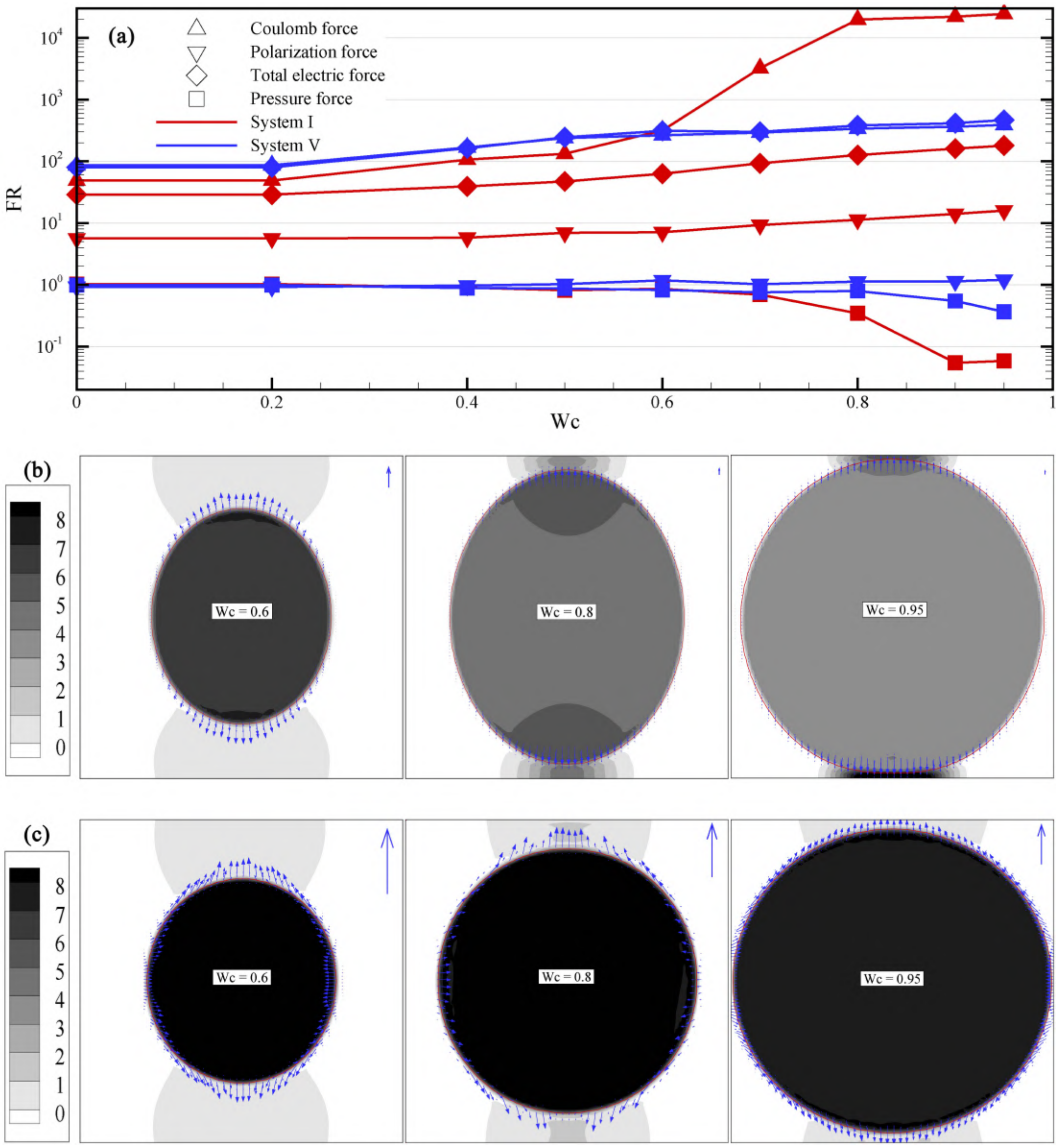

Figure 4.9 **Comparison between forces on the interface of system I and V.** (a) Effect of confinement ratio on the force ratio of points on the vertical and horizontal axes of the droplet which act in the prolate elongation. Pressure contour and vectors of total electric force for (b) system I, and (c) system V. Unit arrows are shown at the top-right corner of the sub-figures.

and Coulomb forces increase at large confinement ratios, while this increment is significant for Coulomb force, resulting in the growth of the total electric force on the interface. Accordingly, one can expect the monotonical increase of the prolate deformation with respect to the confinement ratio. As shown in Fig. 4.4, however, the deformation value starts to decrease at $Wc = 0.8$. On the other hand, FR of the pressure indicates that in small confinement ratios, this value is around unity, meaning that the pressure is distributed equally around the interface. However, by further increasing the confinement ratio above $Wc > 0.7$, FR decreases such that the pressure force pushes the droplet from top/bottom poles of the droplet, so it acts in the opposite direction of the electric forces. In very large confinement ratios i.e. $Wc > 0.8$, the pressure dominates the electric forces leading to a reduction in the prolate deformation of the droplet in system I. This explains the maximum prolate deformation at $Wc = 0.8$. For system V, the FR of the polarization force remains almost constant across all confinement ratios, while the Coulomb force slightly increases at large confinement ratios. On the other hand, the pressure FR decreases such that it dominates the Coulomb force. As it can be seen in Fig. 4.9-b and c, the magnitude of the electric forces in the system I is much larger than those in system V as represented by the unit arrows shown at the top-right corner of the sub-figures. So, the decrease of the pressure FR is magnified enough in very large confinement ratios so that the droplet exhibits an oblate deformation as seen in Fig. 4.4.

A similar analysis has been conducted here for systems II and III as demonstrated in 4.10. In contrast to systems I and V, systems II and III have oblate deformations in small confinement ratios, but increasing the confinement ratio will change their deformation into prolate shapes. By analyzing the force ratio FR of both systems in Fig. 4.10-a, it is revealed that the Coulomb force ratio is very small at small confinement ratios, showing an extreme tendency to deform the droplet into an oblate shape. It should be noted that the Coulomb force ratio of system III is extremely small, i.e. $O(10^{-4})$ thus, it is not shown in Fig. 4.10-a. The polarisation force ratio, on the other hand, is in the order of $O(10^{0})$ for both cases. This results in a total electric force ratio in the range of $O(10^{-1})$ which induces oblate deformation for both systems, despite the presence of the opposing pressure force ratio. Subsequently, the interplay between the resultant electric force and the pressure enforces the droplet to deform into an oblate shape. By increasing the confinement ratio, the Coulomb FR remains in the same order of magnitude while the polarisation force ratio monotonically increases for both systems. So, the resultant electric force has an increasing trend that changes the deformation of both systems from oblate to prolate elongation. It is observed for system II that the pressure force ratio decreases considerably such that it balances the effect of the total electric force in the opposite way. This reduces the prolate deformation of the droplet in system II at very large confinement ratios $Wc > 0.8$. This condition is not observed in system III.

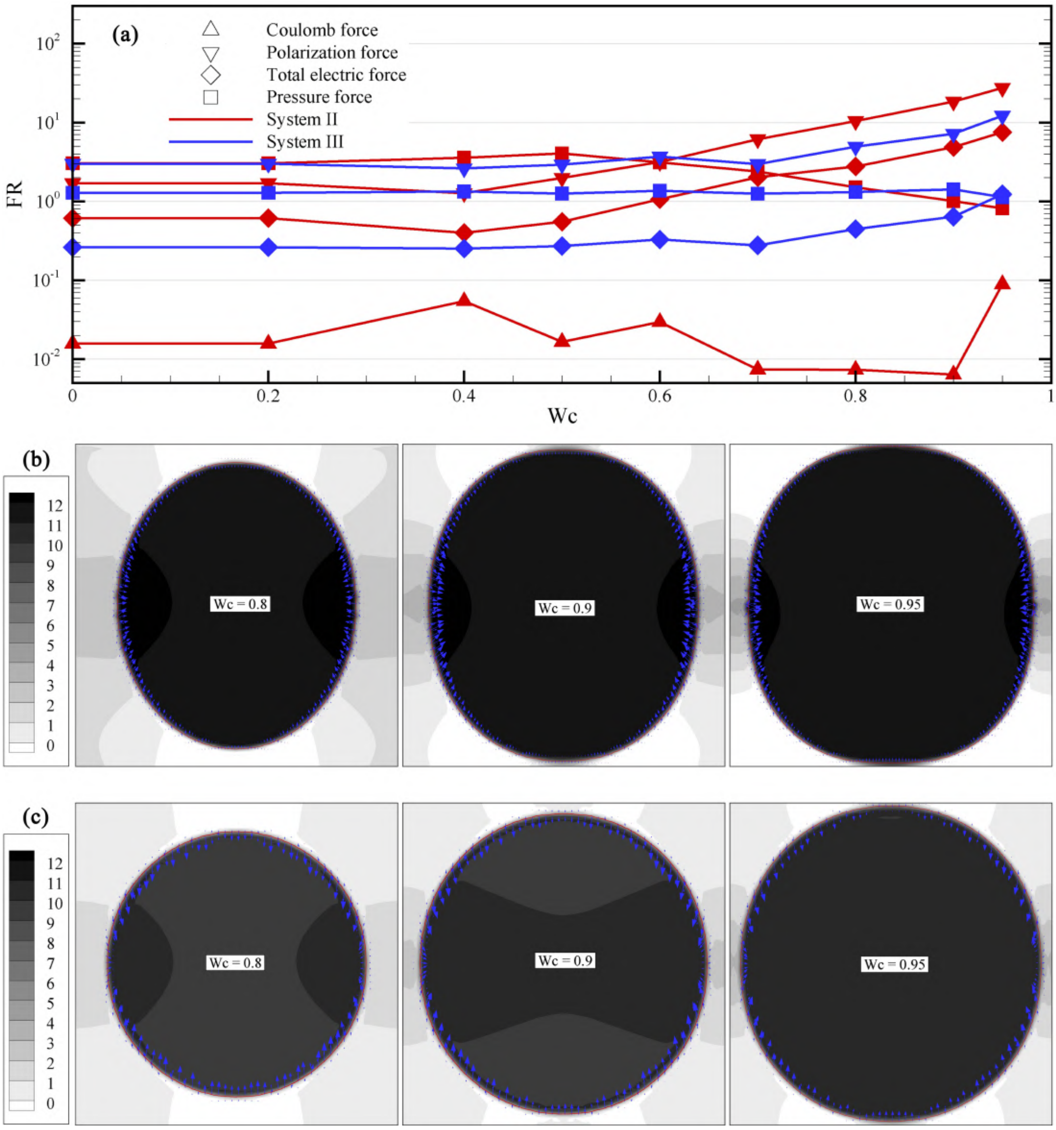

Figure 4.10 **Comparison between forces on the interface of system II and III.** (a) Effect of confinement ratio on the force ratio of points on the vertical and horizontal axes of the droplet which act in the prolate elongation. Pressure contour and vectors of total electric force for (b) system II, and (c) system III.

5. Dynamics of a double emulsion under the combined effects of electric field and shear flow

5.1 Introduction

in the present study, the dynamics of a 2D Leaky dielectric double emulsion is thoroughly investigated under the combined effect of applied electric field and shear flow using ISPH. To address the impacts of electrical property ratios of the core, shell, and medium, six different fluid configurations are numerically handled. All the components of the electrical and hydrodynamics forces are calculated on the droplet interfaces and within the flow domain correspondingly and their influence on the droplet deformation are discussed in detail considering both their magnitude and sign. Effects of capillary and electrical capillary numbers, droplet radius ratio, electrical conductivity and permittivity ratios on the emulsion deformation and angular orientation are explored.

5.2 Problem statement

The schematic of the physical system is shown in Fig. 5.1. As can be seen from the figure, a 2D double emulsion droplet consists of concentric core and shell droplets

---

This chapter is a slightly modified version of "Dynamics of double emulsion interfaces under the combined effects of electric field and shear flow" published in "Computational Mechanics" by "R. Saghatchi, M. Ozbulut, and M. Yildiz"

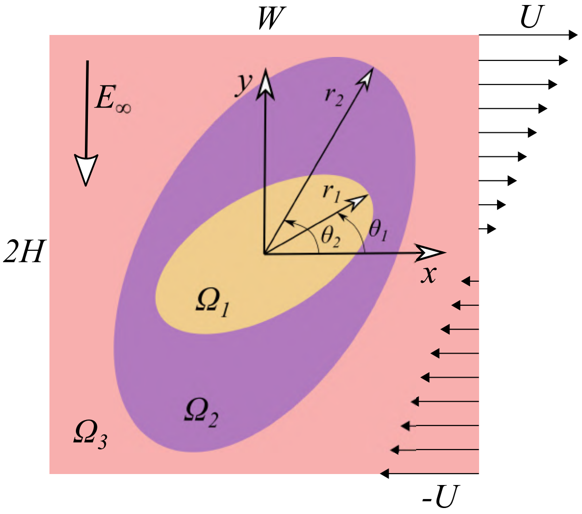

Figure 5.1 **Schematic representation of the physical system.** The double emulsion droplet placed in a Couette device and the constant external electric field is applied in the vertical direction.

with initial radii of r_1 and r_2, respectively, and is suspended in a third medium fluid subjected to a simple shear flow in a square domain with dimensions of $W = 2H$. A uniform electric field E_∞ is applied in the downward direction. It is assumed that there is no relative motion between droplets and ambient fluid initially, and no gravitational force is present. No-slip boundary condition is applied on top and bottom boundaries with constant velocities $\mathbf{U}$ and $-\mathbf{U}$, respectively, while periodic boundary condition is enforced on the right and left boundaries of the domain to reproduce the shear-driven (Couette) flow. As for the electric potential, Dirichlet and Neumann boundary conditions are employed for horizontal and vertical walls, respectively. All particles inside and outside the double emulsion are arranged in the form of a uniformly spaced Cartesian grid.

The ratio of physical properties in the domain is defined as:

$$\mathcal{D}_{mn} = \rho_m/\rho_n, \quad \mathcal{V}_{mn} = \mu_m/\mu_n, \quad \mathcal{P}_{mn} = \varepsilon_m/\varepsilon_n, \quad \mathcal{C}_{mn} = \sigma_m/\sigma_n, \tag{5.1}$$

whereas subscripts m and n refer to mth and nth fluids, respectively ($m, n = 1, 2, 3$). Subscripts 1, 2 and 3 denote the core (inner droplet), shell (intermediate droplet) and background or medium fluid phases, respectively, whereas the double subscript mn represents the interface between mth and nth fluids. Important non-dimensional parameters of the current study are Reynolds number ($\mathrm{Re} = \frac{\rho_2 \mathbf{U} d_2}{\mu_2}$), Weber number ($\mathrm{We} = \frac{\rho_2 \mathbf{U}^2 d_2}{\gamma_{23}}$), Electro-Weber number ($\mathrm{Ew} = \frac{\rho_2 \mathbf{U}^2}{\varepsilon_2 E_\infty^2}$), capillary number ($\mathrm{Ca} = \frac{\mathrm{We}}{\mathrm{Re}} = \frac{\mu_2 \mathbf{U}}{\gamma_{23}}$), and electrical capillary number ($\mathrm{Ec} = \frac{\mathrm{We}}{\mathrm{Ew}} = \frac{\varepsilon_2 E_\infty^2 d_2}{\gamma_{23}}$), where E_∞ is the electric field intensity, $\mathbf{U}$ is the velocity of top and bottom plates and d is the droplet diameter. We will also use dimensionless time t in our simulation which is defined as $t = \frac{t'\mathbf{U}}{2H}$ where $2H$ is the domain width.

5.3 Numerical consistency and accuracy studies

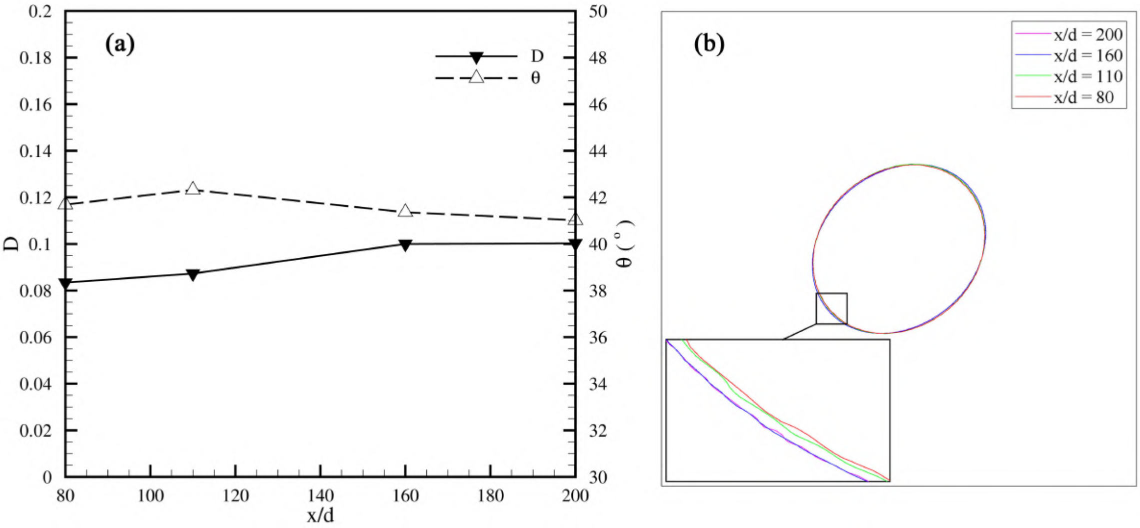

Figure 5.2 **Effect of particle resolution on the droplet deformation in pure shear flow.** (a) Quantitative, and (b) qualitative results.

Particle resolution independency test is carried out by simulating a single emulsion droplet ($r_1/r_2 = 0$) under the effect of pure shear flow ($E_\infty = 0$) whereby the deformation and angular orientation of the droplet is analyzed. Considering different particle resolution $X/d = 80, 110, 160$, and 200 where X/d is the number of particles per unit of droplet's initial diameter, numerical simulations are performed for Re << 1 and Ca = 0.094, which imitate the conditions used in the experimental study of Bruijn, de (1989). It should be noted that the density and viscosity ratios are considered as $\mathcal{D}_{ij} = \mathcal{V}_{ij} = 1$. The extent of the deformation for the single emulsion droplet is calculated by (4.3). However, here, l_1 and l_2 are the longest and shortest diameters of the deformed droplet, respectively. In Fig. 5.2, the results of these simulations are given both qualitatively and qualitatively for $t = 0.25$. As seen from the figure, upon increasing the particle resolution from $x/d = 80$ to 110 and 160, the numerical accuracy also gets improved. However, further increase in the particle resolution does not bring about significant change in the obtained results. Thus, $x/d = 160$ is selected as a reference particle resolution.

The fidelity and the reliability of our current in-house code has been proven for the EHD simulation of a droplet in chapter 4. However, for the additional validation and verification tests, the deformation of a single emulsion droplet is simulated under the pure shear flow. For this test case, the same simulation condition is considered as in the case of the particle resolution dependency analysis. SPH results are compared with the available results from previous numerical and experimental studies. To further demonstrate the accuracy of the SPH method, another simulation is also performed using the OpenFOAM. Having performed a mesh and time step independency analysis, a uniform Cartesian mesh composed of 120 by 120 cells and 10^{-4} time step size are selected for all the simulations with OpenFOAM, while the CFL condition is utilized to adjust the time step size throughout the simulation. Gauss upwind scheme is used for the discretization of convection term and the Euler scheme is used for the time marching with PISO algorithm for the correction. Transient droplet deformation is calculated for different values of Ca number and the results are shown in Fig. 5.3-a and b. Reynolds number is set to $\mathrm{Re} = 1$ and $\mathrm{Re} << 1$ for Fig. 5.3-a and b, respectively. As shown in these figures, a close agreement is observed between SPH and other numerical/experimental results as well as the values obtained by OpenFOAM. A qualitative comparison is also realized between SPH and OpenFOAM result and shown in Fig. 5.4 for $\mathrm{Ca} = 0.194$ at $t = 1$. As can be readily inferred from this figure, both numerical results exhibit similar patterns of streamlines and contour of normalized velocity magnitude.

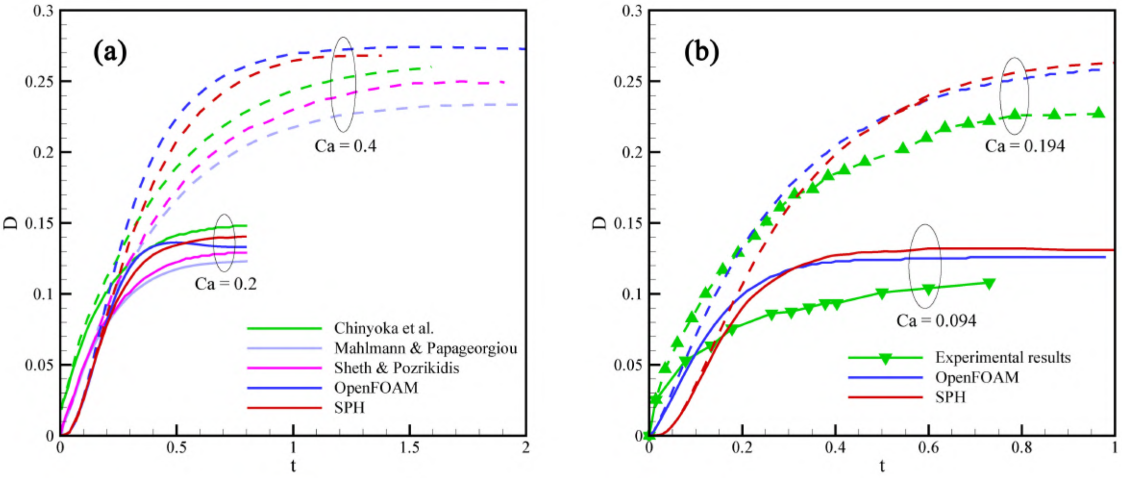

Figure 5.3 **The comparison of the single emulsion droplet deformation under the pure shear flow.** Data of the previous (a) numerical and (b) experimental studies. For the pure shear flow, numerical results of Chinyoka et al. (2005), Mählmann & Papageorgiou (2009), and Sheth & Pozrikidis (1995), and experimental results of Bruijn, de (1989) are used here. Results of Finite Volume simulation with OpenFOAM are compared as well.

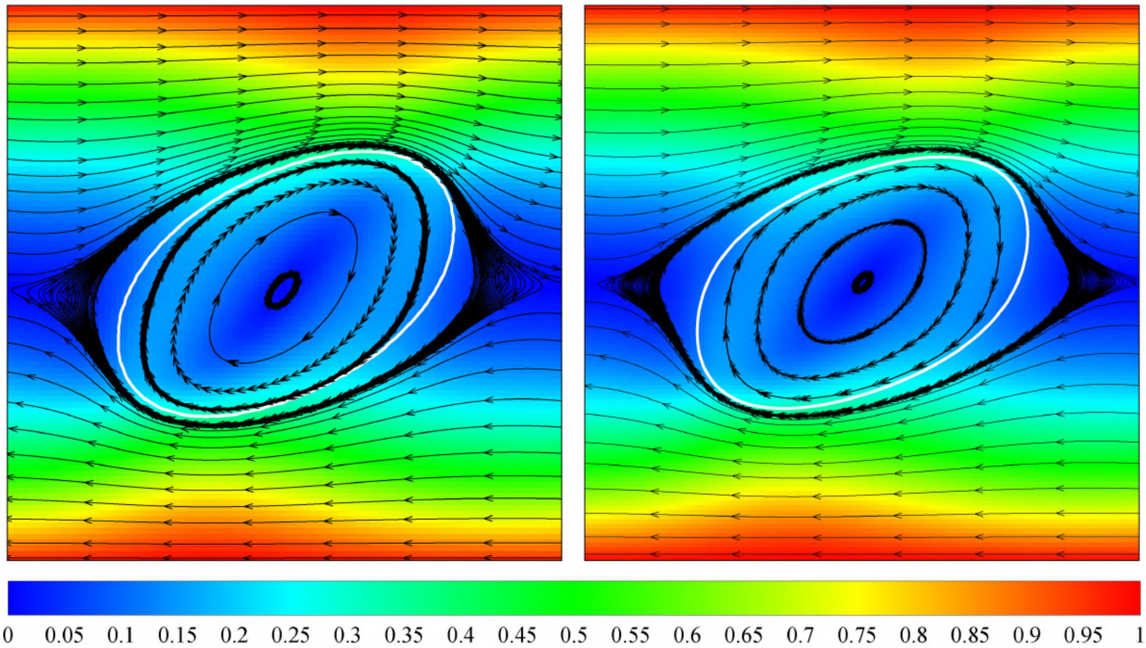

Figure 5.4 **The comparison of normalized velocity magnitude contour and streamlines for the single emulsion droplet under the pure shear flow.** The SPH data are shown on the left and OpenFOAM on the right. Results are taken at $Ca = 0.194$, and $t = 1$.

In this section, the dynamics of a double emulsion droplet under the combined effects of electric field and shear flow is presented by considering six different systems of fluids, as tabulated in Tab.5.1. The first three systems are selected from experiments in micro- and bio-fluidics applications. The properties of the remaining systems are chosen hypothetically but carefully to scrutinize all possible forms of double emulsion deformation. In all simulations, core and medium fluids are identical, which is the condition that has also been utilized in some previous numerical and experimental studies (Abbasi et al., 2019; Opalski, Makuch, Derzsi & Garstecki, 2020; Song & Shum, 2012; Tsukada et al., 1997). Furthermore, in all cases, viscosity and density ratios are considered to be unity, $\mathcal{D}_{mn} = \mathcal{V}_{mn} = 1$. Double emulsion dimensions are chosen as $r_2/H = 0.25$ and core to shell droplet radius ratio is $r_1/r_2 = 0.5$, unless stated otherwise.

Figure 5.5 represents the streamlines inside the domain for all systems at $t = 0.4$. All sub-figures demonstrate the deformed double emulsions at $\mathrm{Ca} = 0.4$ and $\mathrm{Ec} = 0.4$. As shown in this figure, the deformed shape of the double emulsions is closely related to the conductivity ratios of the fluids. For systems I, II, III, and VI, which have relatively large values of conductivity ratio ($\mathcal{C}_{21} > \mathcal{O}(10^{-1})$), double emulsions are deformed and oriented without breakup. However, in systems IV and V with smaller conductivity ratios ($\mathcal{C}_{21} = \mathcal{O}(10^{-2})$), breakup occurs. For the double emulsions with no breakup, there is a high strength vortex inside the core, and two weak vortices

Table 5.1 Dielectric properties that are used in this study.

System	Ambient & core fluids	$\sigma_1, \sigma_3(\frac{S}{m})$	$\varepsilon_1, \varepsilon_3(\frac{F}{m})$	Shell fluid	$\sigma_2(\frac{S}{m})$	$\varepsilon_2(\frac{F}{m})$	$\mathcal{C}_{21}$	$\mathcal{P}_{21}$	Reference
I	silicon oil 1	2.67×10^{-12}	2.66	corn oil	1.06×10^{-11}	3.24	3.9700	1.2180	(Tsukada et al., 1994)
II	medium	1.8×10^{-2}	80	cytoplasm	0.5	75	27.780	0.9375	(Hunt et al., 2009)
III	corn oil	1.06×10^{-11}	3.24	silicon oil 1	2.67×10^{-12}	2.66	0.2519	0.8210	(Tsukada et al., 1994)
IV	hypothetical	27.78	0.821	hypothetical	1	1	0.0360	1.2180	-
V	hypothetical	50	10	hypothetical	1	1	0.020	0.10	-
VI	hypothetical	0.05	0.033	hypothetical	1	1	20.0	30.0	-

at both sides of it. For systems IV and V, however, the pattern of streamlines is more complex due to the breakup of the droplet.

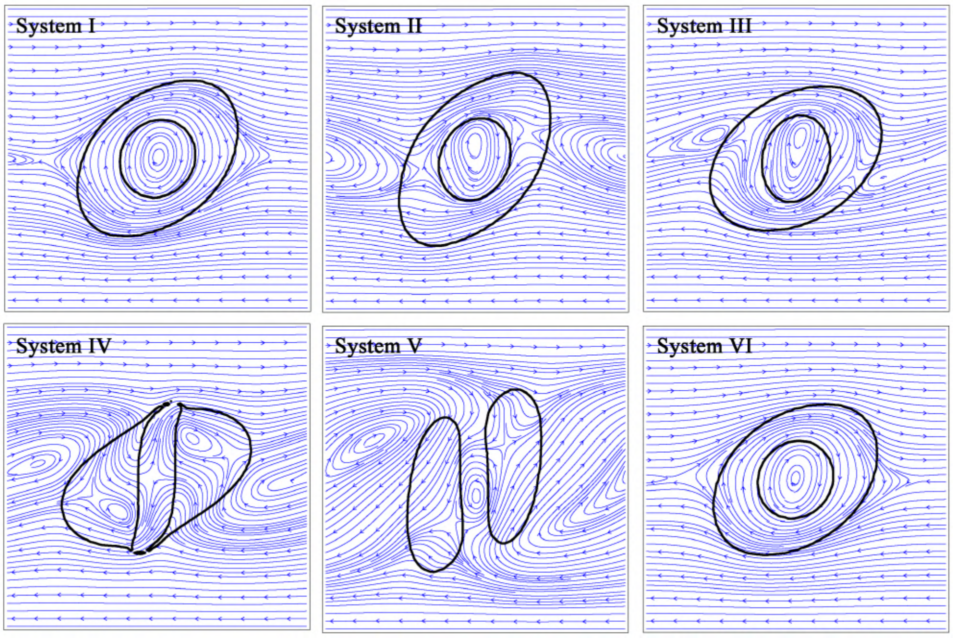

Figure 5.5 **Streamlines inside and outside of the deformed double emulsions.** Double emulsions are deformed under the combined effect of electric field and shear flow for Ca $= 0.4$ and Ec $= 0.4$ at the non-dimensional time $t = 0.4$

To see the effect of electric field and shear flow separately, a streamline of the domain is shown in Fig. 5.6. In the sub-figures (a) and (b), the dynamics of the double emulsions are presented in the presence of pure electric field and pure shear flow, respectively. As it is shown in Fig. 5.6-b, all systems exhibit a similar behavior under the effect of pure shear flow regardless of their different electrical properties as it should be. Since in the pure EHD, the flow field is symmetric in both x- and y- directions, only half of the domain is shown in Fig. 5.6-a. It should be noted that all figures are plotted for the same instant of the time (i.e., $t = 0.4$) as in Fig. 5.5. Three different vortex patterns can be observed in the flow field under the pure effect of the electric field. In systems II, V, and VI, there is only one vortex in each quarter. However, for the other systems, there is a pair of vortices in each quarter, one in the ambient fluid, and the other in either shell (systems III and IV) or core (system I) droplets. The direction of the ambient vortex depends on the conductivity and permittivity ratios such that the velocities run from the top and the bottom towards the left and the right of the droplet for the systems I, II, V and VI while it rotates in the opposite direction for the others. We have shown in chapter 4 that for the single emulsion, velocity in medium fluid runs from poles to the equators when $\mathcal{C} > \mathcal{P}$ and vice versa. For the double emulsion, however, this is only true when the deviation of $\mathcal{P}$ from unity is not too high. Thus, for the systems

I, II, III, and IV, the circulation direction is similar to the single emulsion studied in chapter 4. For the systems V and VI, circulation behaves reversely due to the significant difference between $\mathcal{P}$ and unity.

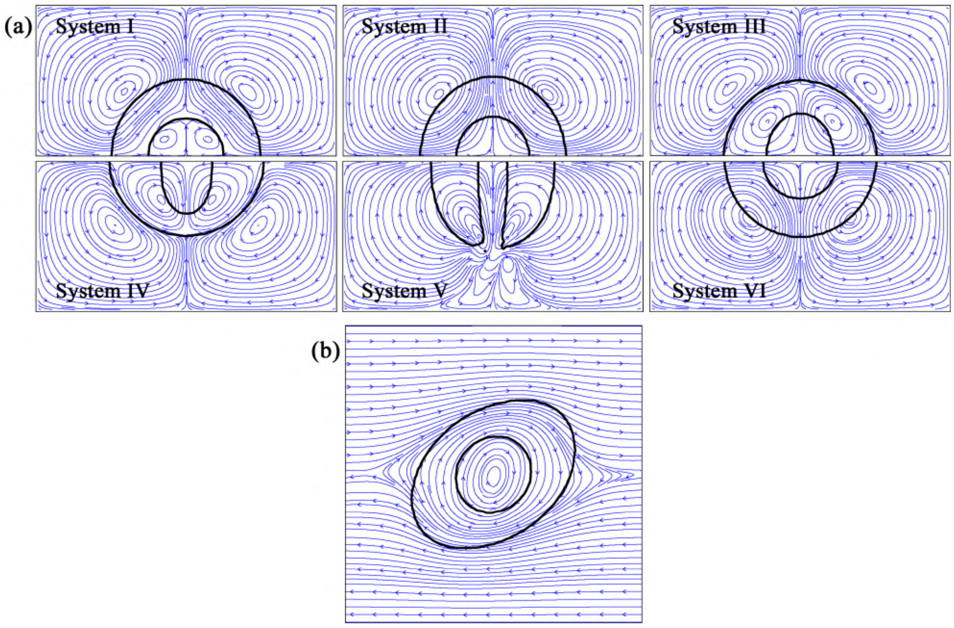

Figure 5.6 **Streamlines inside and outside of the deformed double emulsions.** Deformations are due to (a) the pure electric field with Ec $= 0.4$ and (b) the pure shear flow with Ca $= 0.4$ at the non-dimensional time $t = 0.4$. Due to the symmetry in the y- direction of the flow in the presence of the pure electric field, only the half of the domain is shown.

To shed light on why double emulsion breaks up and also vortex location changes, we studied the individual effect of electrical properties of droplet, electric field strength and the shear flow characteristic on the deformation values of core/shell droplet as well as the droplet orientation. The deformation D and orientation θ of the core and shell droplets are obtained for each system at $t = 0.4$ and tabulated in Tab.5.2 for different cases including pure EHD, pure shear flow, and combined EHD and shear flow. The orientation angle $\theta = 90$ and $\theta = 0$ correspond to prolate and oblate elongations, respectively. It should be noted that in the pure EHD flow, the necessary condition for the double emulsion breakup is the large difference in deformation values between core and shell droplets ($D_{core} >> D_{shell}$). The breakup will be further facilitated if the core and shell droplets deform into different shapes and have the opposite deformation sign (i.e., one assumes $\theta < 45$ and the other one has $\theta > 45$). These conditions are realized for systems I, III, IV, and V. However, breakup occurs only in the system V since the strength of the electric force is large enough to elongate the core droplet adequately. As a result, the core droplet splits the shell droplet and thereby lead to the breakup of the double emulsion. In the system V, both core and shell droplets are deformed into the prolate shape with much higher deformation for the core. For example, the deformation values before the breakup at $t = 0.2$ are $D = 0.281$ and $D = 0.055$ for core and shell droplets, respectively. Applying a shear force in addition to the EHD would intensify the breakup tendency of these systems. As can be recalled from Fig. 5.5, the applied shear force would cause the double emulsion for the system IV to undergo a breakup. Another interesting finding is related to the orientation angle of core and shell droplets. As was remarked by Hua et al. (2014), the orientation angle of the core is always greater than or equal to the shell's for the double emulsion under the pure shear flow. Our numerical results also confirm the claim of Hua *et al.* for pure shear flow as well as the combined EHD and shear flow. Recalling from Fig. 5.6, there is a pair of vortices in each quarter of the systems I, III, and IV whereas there is only one in the systems II, V, and VI. This can be reasoned out through considering the orientation angles given in Tab.5.2 for the pure EHD case. The difference between the orientation angle of core and shell droplets in the systems with a pair of vortices, is $\Delta\theta = 90^o$ whereas for the systems with only one vortex is $\Delta\theta = 0^o$. Moreover, in the systems with a pair of vortices (I, III, and IV), only for the system I, there are vortices inside the core droplet. As shown in Tab.5.2 for the system I, the core and shell droplets deform into the oblate and prolate shapes, respectively unlike the system III and IV, in which the core and shell droplets deform into the prolate and oblate shapes, respectively.

Figure 5.7 present the variation of the absolute value of double emulsion deformation as a function of the non-dimensional time for both core and shell droplets under the effect of combined EHD and shear flow. In this figure, core and shell deformations are shown with solid and dashed lines, respectively. As mentioned previously, the deformation of the core droplet is much higher for systems IV and V which undergo a breakup. Moreover, the core deformation for the system V is much greater than that for the system IV. Consequently, the system V breaks up before the system IV. Nonetheless, the difference between core and shell deformations are not significantly high for the rest of the systems.

To investigate the core and shell droplet deformations, interface forces should be evaluated in detail. As described in chapter 2, one of the important interfacial forces is the electrical force composed of two important components, namely, Coulomb and polarization forces. It can be easily concluded that the Coulomb force acts along the direction of the electric field while the direction of the polarization force is normal to the droplet interface in the opposite direction of the electrical permittivity gradient. These two forces are demonstrated in Fig. 5.8 for all systems at $t = 0.1$. The contours and directions of the Coulomb and polarization forces are shown in Fig. 5.8 (a) and (b), respectively. In the systems I and II, the Coulomb force is exerted on the top and bottom poles of the shell droplet in the outward direction while

Table 5.2 Deformation and orientation of core and shell droplets in all six systems at $t = 0.4$ for a double emulsion under the effect of pure electric field, shear flow and combined EHD and shear.

Case		system I		system II		system III		system IV		system V		system VI	
		Core	Shell	Core	Shell	Core	Shell	Core	Shell	Core	Shell	Core	Shell
Pure EHD	D	0.001	0.015	0.043	0.046	0.121	0.004	0.345	0.016	-	-	0.006	0.004
	θ	0	90	90	90	90	0	90	0	-	-	90	90
Pure shear	D	0.044	0.179	0.044	0.179	0.044	0.179	0.044	0.179	0.044	0.179	0.044	0.179
	θ	47.90	36.38	47.90	36.38	47.90	36.38	47.90	36.38	47.90	36.38	47.90	36.38
Combined effect	D	0.049	0.190	0.108	0.250	0.134	0.192	-	-	-	-	0.047	0.181
	θ	51.63	42.09	63.67	51.72	75.60	31.20	-	-	-	-	52.00	37.80

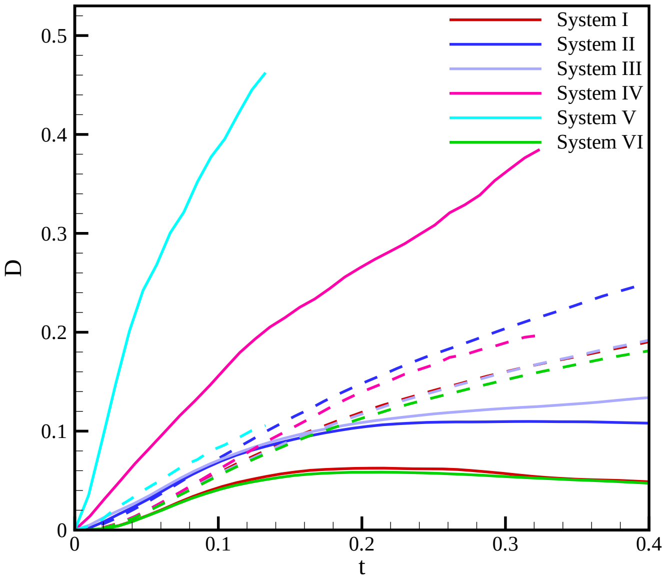

Figure 5.7 **Time evolution of double emulsion deformation.** The solid- and dashed- lines correspond to the core and shell deformations, respectively. Data are taken at $\mathrm{Ca} = 0.4$ and $\mathrm{Ec} = 0.4$.

the polarization forces act in the outward and inward directions for the systems I and II, respectively. By comparing the magnitude of forces for the system II, the resultant electric force is in the outward direction similar to the system I, which elongates both shell droplets into prolate shape. For the other systems, Coulomb forces act in the inward direction whereas the polarization forces act toward the center of the systems III and II unlike the systems IV and VI. By comparing the magnitude of the Coulomb and polarization forces, the total electric forces lead to the oblate deformation of the shell droplet for the systems III, IV, and VI. For the system V, however, the magnitude of the electric force is higher at the sides of the shell droplet, thus deforming it into the prolate shape. A similar analysis may be conducted for the core droplet. Such investigation reveals that the direction of both Coulomb and polarization forces are toward the center for the system I only, and the resultant total electric force acts on the left and right sides of the core droplet and stretches it to deform into the oblate shape. For the other systems, however, the force direction and its point of application are such that the total electric force deforms the core droplet into a prolate shape.

In addition to the electric forces, hydrodynamic interaction plays an important role in the double emulsion dynamics (Luo et al., 2015). These interaction can be studied considering the hydrodynamic stress tensor. Lou *et al.* claimed that the hydrodynamic interaction mainly depends on the distribution of the stresses inside the shell

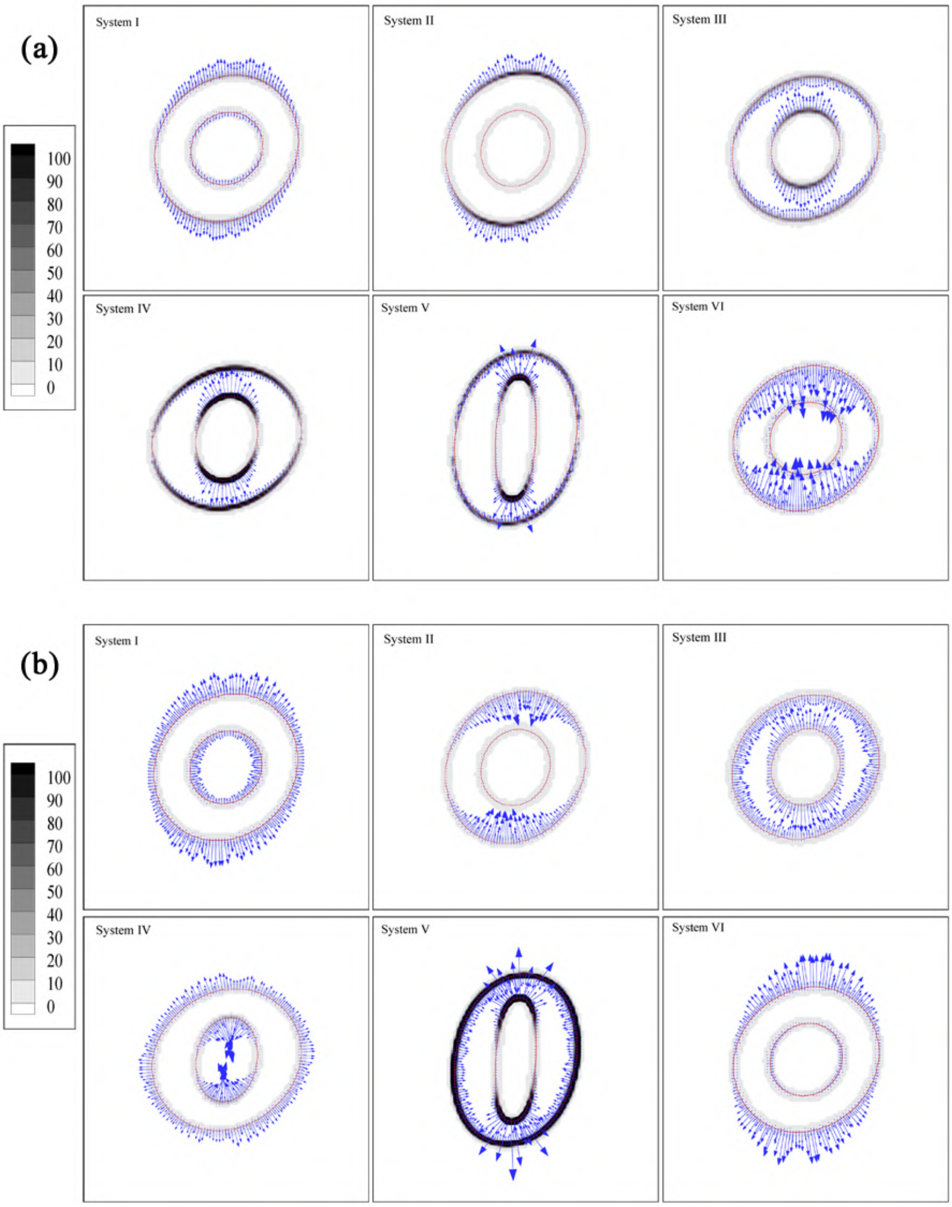

Figure 5.8 **Electric force on the interfaces.** Comparison of (a) Coulomb force and (b) polarization force on the interface of core and shell droplets at $t = 0.1$ for all systems. Note that contours on the interface indicate the magnitude of the corresponding force.

droplet, which is significantly affected by the core size and the deformations of the shell and core droplets (Luo et al., 2015). Hence, pressure and viscous stresses are shown in Fig. 5.9. Since the stress distribution of double emulsions in the systems I, II, III, and VI are almost similar, for the sake of brevity, only system III is selected as their representative and shown alongside the system IV and V. As shown in Fig. 5.9, the pressure force has a significant contribution to the hydrodynamic interactions while the viscous force is trivial in these systems since the viscosity ratio is unity. Therefore, we only consider the pressure term in the following. The pressure value is high in the core droplet of the system III while the maximum pressure occurs at the shell droplet for the system V. The pressure distribution determines the curvature of the droplet interface and subsequently, its deformation value. As presented in Fig. 5.9-a for the systems IV and V, pressure in the core droplet has its lower value near the tips (high curvature) while it reaches its higher values at the equator of the core droplet (low curvature). Within the shell droplet, regions with maximum and minimum pressure values coincide with the different locations for the systems IV and V. As represented in Fig. 5.9-a, there is high- and low-pressure regions at the equator and tips for the systems IV, respectively. For the system V, however, tips and equator correspond to the high- and low-pressure regions, respectively. The pressure is distributed uniformly inside the core and shell droplets for the system III, which is commensurate with the uniform curvature of these droplets, thereby resulting in the low deformation value as represented in Fig. 5.7. The pressure gradient inside the droplets for the system V is higher than that of the system IV, which leads to the higher value of deformation in the system V.

To particularize the effect of shell droplet thickness on the double emulsion dynamics and deformation, two additional core to shell droplet radius ratios, i.e. $r_1/r_2 = 0.25$ and 0.75 are also simulated. The results of these simulations are presented in Fig. 5.10-a in terms of the deformation and the angular orientation values of the double emulsion. A detailed evaluation of this figure reveals that the variation of the deformation with respect to r_1/r_2 for the core droplet has an opposite trend in comparison to that for the shell droplet. Namely, as the deformation increases for the core droplet, it decreases for the shell one. This behavior can be explained considering that the deformation of droplet is directly linked to its diameter. Note that the increase in r_1/r_2 can be controlled by either increasing or decreasing the diameter of core or shell droplet, respectively. This can explain the opposite behavior of core and shell deformations. Droplets with the higher extent of prolate deformation would experience a higher inertial force under the shear flow. This force will compel the droplet to orient itself in a horizontal position. Thus, the orientation angle of the core droplet decreases by the increase in r_1/r_2. Remembering Fig. 5.8, the direction of the electric force on the core droplet for the system III is such that it elongates the core, hence causing prolate deformation. Because of this elongation, the pressure force inside the shell would be higher at the poles and causes the shell droplet to elongate and to acquire a more prolate shape accordingly. The larger value of r_1/r_2 corresponds to a thinner shell droplet, in which there is not enough space for the core droplet to deform freely, resulting in an increase in the pressure force at the shell poles. Thus, at higher r_1/r_2, the shell droplet is forced to elongate in the vertical direction and in turn has a higher orientation angle value.

To investigate the effect of electrical capillary number on the double emulsion dy-

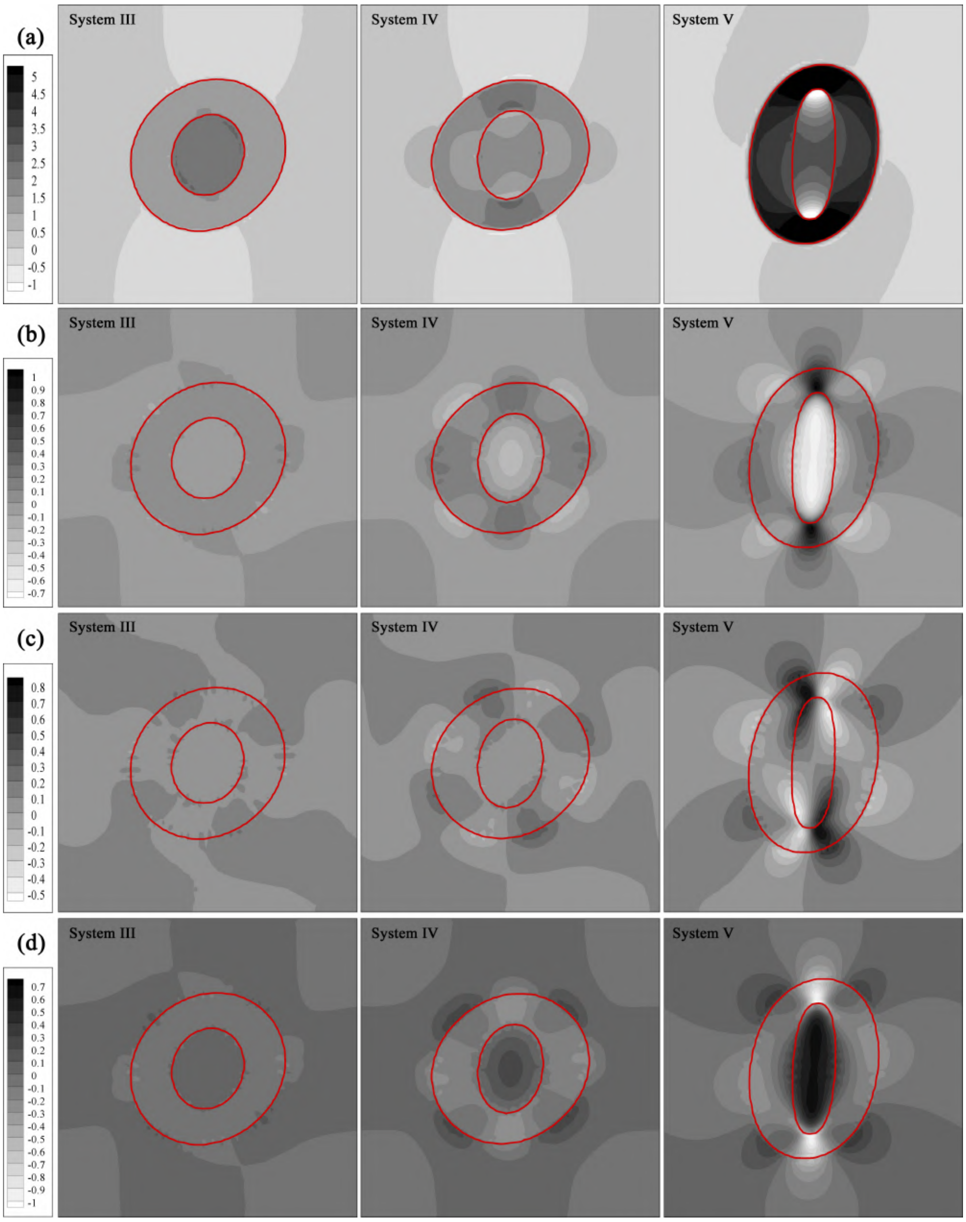

Figure 5.9 **Hydrodynamic and shear forces on the double emulsions.** Comparison of (a) p, (b) $\mu du/dx$, (c) $(\mu/2)(du/dy + dv/dx)$, and (d) $\mu dv/dy$ in the double emulsion under the effect of combined electric field and shear flow at $t = 0.1$.

namics, the capillary number is maintained constant ($\mathrm{Ca} = 0.4$) while the electrical capillary number is changed for each system. The deformation value and the angular orientation are calculated at $t = 0.4$ and presented in Fig. 5.10-b. Regarding the shell droplet, the deformation value is observed to be directly related to the electrical capillary number for all the systems except the system VI in which there is no significant change in the deformation value. Similarly, the orientation angle is also affected by the electrical capillary number for all systems except the system III. These correlations can be explained considering the electric forces on the interface of the shell droplet as has been shown in Fig. 5.8. It can be seen that the resultant

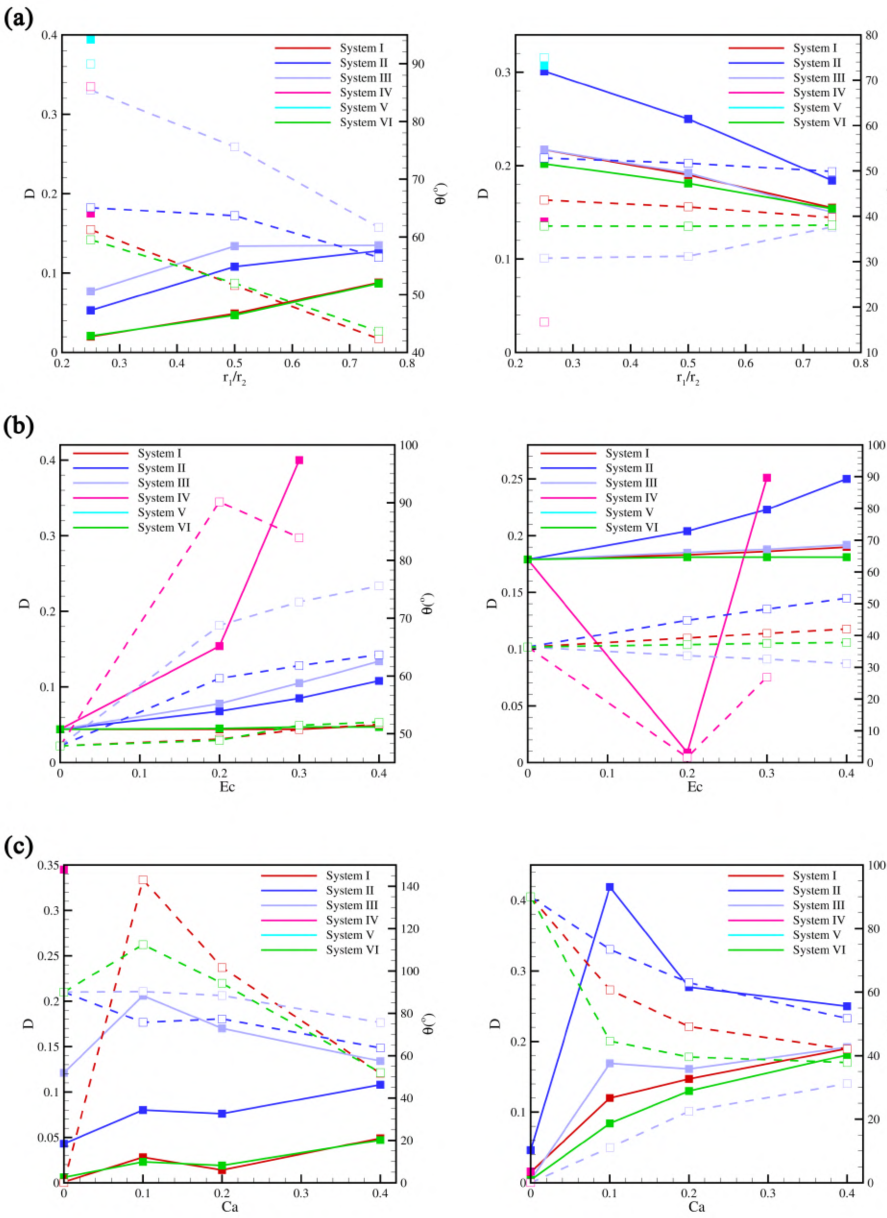

Figure 5.10 **Variation of the emulsions deformation and orientation angle with respect to the important parameters.** Effect of r_1/r_2 (a), Ec (b), and Ca (c) on the deformation, D (—■—) and orientation angle, θ (- - □ - - -) of core droplet (left column) and shell droplet (right column). All data are taken at $t = 0.4$.

electric force exerted on the top and bottom regions of the shell droplet is high for the system III and acts inwardly to the interface. Shear flow induced angular orientation of the droplet leads to the occurrence of a couple force that tends to rotate the droplet in the clockwise direction, hence decreasing its orientation angle. However, for the other systems, this couple force acts such that it rotates the shell droplet in the counterclockwise direction thereby increasing the orientation angle. Moreover, in the system VI, Coulomb and polarization forces on the shell droplet interface have a relatively similar order of magnitude and act in the opposite directions, thus resulting in a negligibly small net electric force. As a consequence, the variation in electrical capillary number does not have a considerable effect on the shell deformation for the system VI. It can be concluded that for those systems in which the shell droplet undergoes an oblate deformation in the absence of shear flow, their orientation angle decreases in mixed EHD and shear flow with an increase in the electrical capillary number. In the system IV, one can see a minimum value in the deformation and orientation angle at $\mathrm{Ec} = 0.2$. It should be noted that applying electric field on this system first reduces the deformation and orientation angle of the shell due to the pure shear flow. However, on further increasing the electrical capillary number, electrical forces on the interface become dominant and affect the droplet behavior. Likewise, core droplet behavior can be explained by investigating the electrical forces on its interface. As a result, the core droplet experiences a high deformation and orientation angle at high electrical capillary numbers. For the double emulsion in which breakup occurs, the variation of deformation with electric capillary number is significant. For instance, in the system IV, the deformation of the core droplet at $\mathrm{Ec} = 0.3$ becomes 9.1 times of its value for the pure shear flow ($\mathrm{Ec} = 0$).

The effect of capillary number (Ca) on the double emulsion dynamics is shown in Fig. 5.10-c for constant electrical capillary number, ($\mathrm{Ec} = 0.4$). The interplay between electrical and hydrodynamics forces determines the droplet deformation and orientation angle. As elaborated previously, core and shell droplets have a significant impact on each other. For instance, the deformation value for the shell droplet of the system III first increases up to $\mathrm{Ca} = 0.1$. The further increase in the capillary number decreases the deformation value as the inertial force becomes dominant. At high capillary numbers, however, the shell droplet thickness decreases at the pole regions, which leads to an increase in the pressure near the poles (Fig. 5.9-a). As a consequence, the shell droplet elongates and hence acquires a larger deformation value. For the system II, there is an extremum at $\mathrm{Ca} = 0.1$ which acts as a maximum point for the shell deformation. For the systems I and VI, the variation of deformation as a function of the capillary number has an increasing, which points out that the hydrodynamics forces are the dominant in these systems. The orientation angle of shell droplet increases for the system III whereas it decreases for the systems I, II, and VI. Core droplet behavior can be explained in a similar manner. It can be shown that the capillary number may enhance the likelihood of the breakup of double emulsion in the system IV. For the system V, however, breakup occurs even without the shear flow ($\mathrm{Ca} = 0$) due to the high value of resultant electric force.

Transient behavior of double emulsions for the systems IV and V are demonstrated

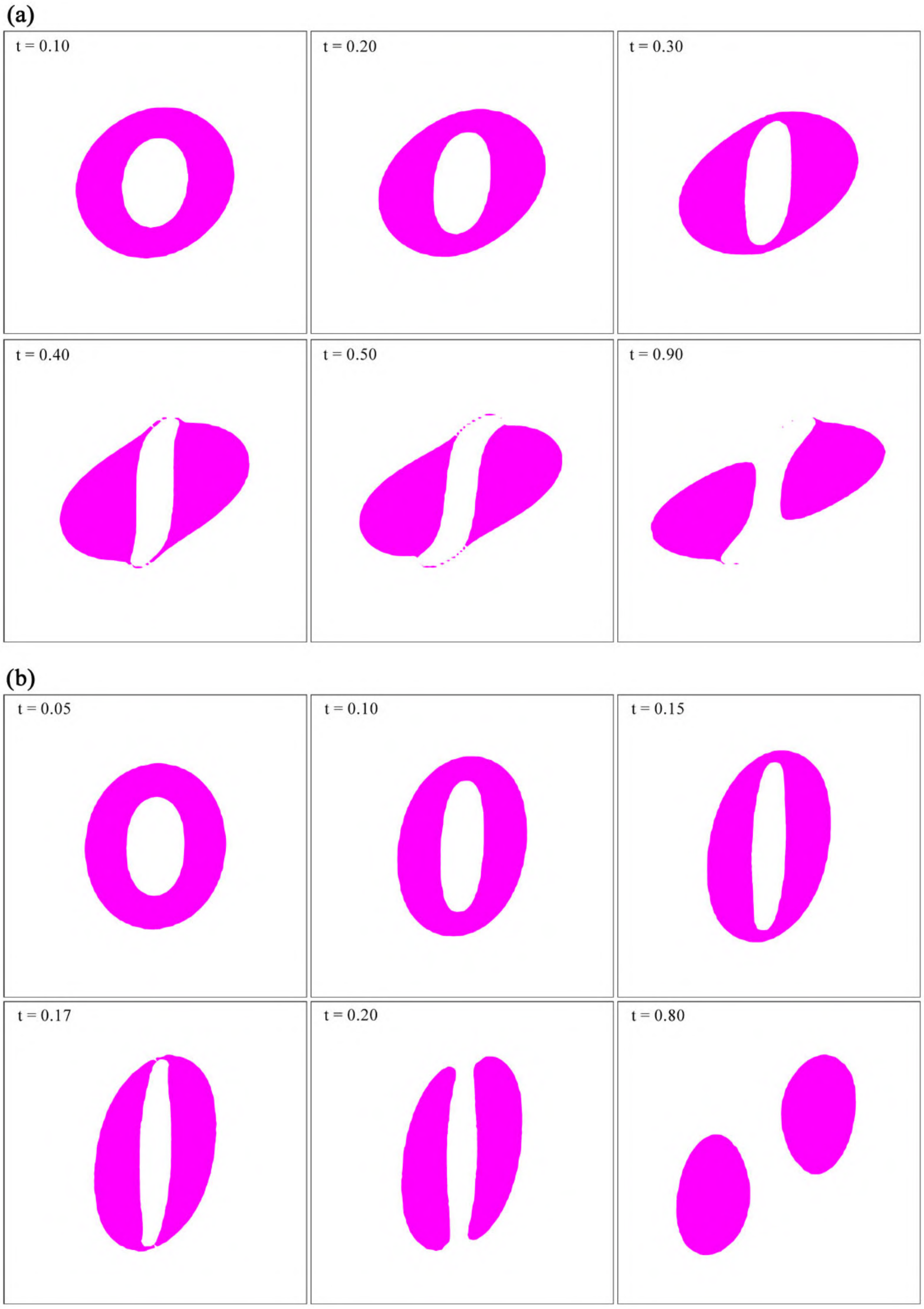

Figure 5.11 **Time evolution of double emulsion during the breakup.** (a) System IV and (b) system V at $\mathrm{Ca} = 0.4$ and $\mathrm{Ec} = 0.4$.

in Fig. 5.11. As mentioned previously, due to the large deformation of the core droplets in the systems IV and V, a breakup occurs. However, the behavior of double emulsions is quite different for these two systems. As such, the core droplet in the system IV deforms into an "S" shape whereas the "S" shape like deformation of the core in the system V is insignificant. Accordingly, after the pinch-off, the shapes of two daughter droplets are different for these two systems. As shown in Fig. 5.11, the daughter droplets in the system IV are "*onion-shaped*" whereas they are "*bean-shaped*" in the system V. It should be noted that in the presence of shear flow, two daughter droplets exhibit radial symmetry, while, in the absence of shear flow, there is a reflective symmetry between them. After a complete breakup, two daughter droplets move away from each other due to the shear forces and each act as a single emulsion. As the time progress, the surface tension force removes the sharp edges of the daughter droplets, thus leading to a smoother interface shape.

6. Development of Smoothed Particle Hydrodynamics Method for Modeling Active Nematics

6.1 Introduction

Recall that governing equations of active nematic fluids are highly coupled and involves advective terms, which are rather challenging to solve with Eulerian based approaches such as LBM. On the other hand, SPH method due to its Lagragian nature can lend itself to the discretization and then to the solution of these equations much more effectively. Specifically, one of the biggest advantages of the SPH method is that the advective terms in the conservation of mass and linear momentum as well as nematodynamics equations can be discretized directly by using material derivative terms thereby circumventing the numerical complexity associated with the solution of these nonlinear terms. Moreover, in SPH, complex and deformable domains, mixtures, multiphase interfaces can also be modelled with relative ease unlike Eulerian approach. This attribute of the SPH method is particularly appealing for modeling mixing behavior in active nematics as well as nematc flow with material interfaces and interface motion (e.g., bacterial growth), which will be the subject of future direction of our research. In this study, due to these particular features, the SPH method is preferred for the numerical solution of active nematic flows.

This chapter is a slightly modified version of "Development of Smoothed Particle Hydrodynamics Method for Modeling Active Nematics" published in "International Journal for Numerical Methods in Engineering" by "R. Saghatchi, D.C. Kolukisa, and M. Yildiz"

6.2 Parallelization algorithm

In this section, a parallel implementation of the developed algorithm is elaborated along with the adopted data structure model. The in-house computer code to perform the simulations is built upon the CUDA GPU parallelism. An object oriented approach that focuses on flexibility and ease of programming rather than pure computational efficiency is adopted in the design of the data structures of the program, which have also enabled the integration of the nematics variables into the SPH particle framework effortlessly. To this end, particle data is organized based on the Array of Structures of Arrays (AoSoA) principle. Physical properties of particles, as well as their relative values between their neighbors are stored in a Structure of Arrays (SoA) for each particle, which are the elements of the particle array as depicted in Figure 6.1. Through this AoSoA approach, memory coalescence is obtained for the intermediary interaction variables ($\mathbf{r_{ij}}$, $r_{\mathbf{ij}}$, $\mathbf{u_{ij}}$, $W_{\mathbf{ij}}$, and $\nabla_{\mathbf{i}} W_{\mathbf{ij}}$) with repetitive usage.

Computations for each particle of the SPH system are assigned to a single thread within the framework of the Single Instruction Multiple Thread (SIMT) execution model of the CUDA programming language. These large numbers of threads are grouped as blocks of threads and are designed to work simultaneously in a parallel manner. All threads have access to the global memory of the GPU, while the threads within the same block also have access to a specific shared memory, and each thread has its own local memory. Following the initial distribution of particles, the particle array is copied from the host (CPU) memory to the device (GPU) global memory. Parallel computations are performed via the CUDA kernel functions, which are written in isolated serial forms, and executed simultaneously for each thread/particle in the SIMT framework. It should be noted that the term CUDA kernel is a programming concept that should be distinguished from the term kernel function in SPH formalism.

Generating ghost boundary particles are problematical for parallel algorithms, since a so-called race condition appears when boundary fluid particles attempt to insert their corresponding ghost duplicates into the particle array simultaneously. Therefore, ghost particle generation needs to be handled serially. In this study, a single GPU thread within a CUDA kernel is utilized for this task in order to avoid performing a costly two-way memory copying operation of particle array between the device and the host at each time step. An outline of the computational algorithm for one time step is schematized in 1. The sequential instructions which are grouped

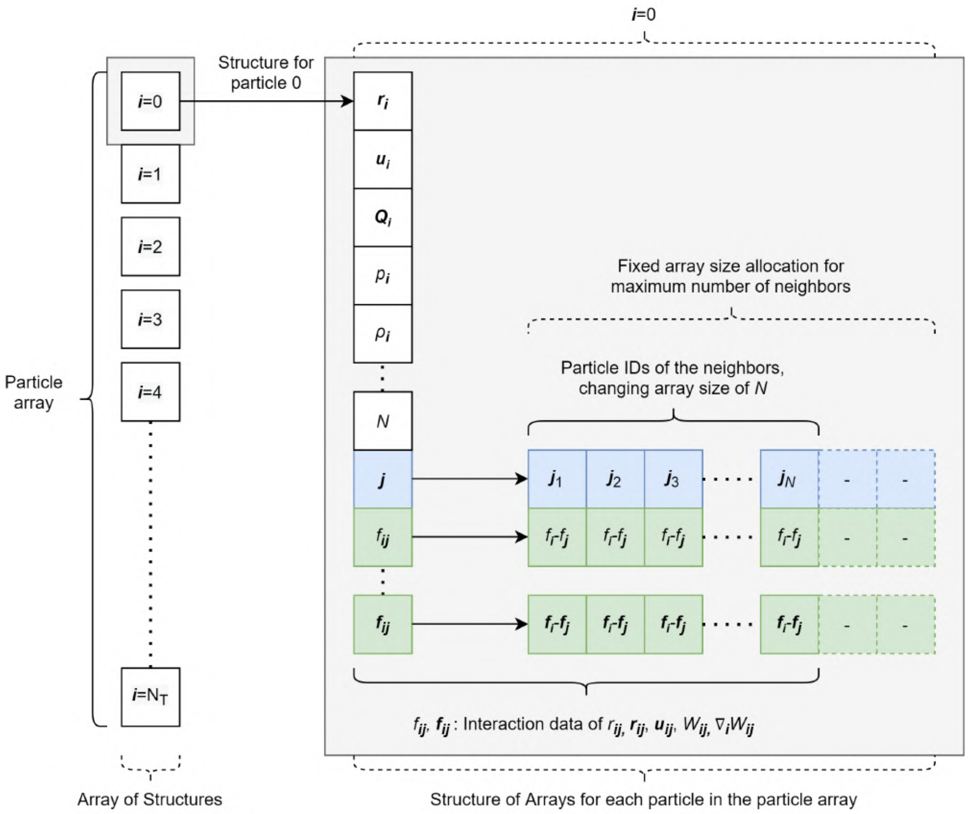

Figure 6.1 **Array of Structures of Arrays organization for storing particle and interaction data.** The column on the left hand side is the particle array. Each member of the particle array consists of a SoA as depicted on the right hand side. The SoAs for each particle "**i**" have members of variables that store function values for the given particle and have array members as well to store neighbor interaction data.

under CUDA kernels 1, 2, and 3 in 1 are serial instructions for a single thread that is mapped for the computations of a single particle. However, the ghost particle production operation is an exception since it is performed serially by a single GPU thread. It should be noted that the computations that require summations of the neighbor values include nested serial loops within the thread. A GPU-optimized neighbor searching algorithm (Green, 2007) is implemented for computing neighbor interactions. In this approach, the flow domain is divided by square cells, and a pseudo particle number array is sorted according to their cell numbers at each time step. Subsequently, linked lists of the pseudo particle number arrays are created for each cell by utilizing shared memory arrays. As a result, a data structure is obtained, where the threads of each particle can easily search the linked lists of neighboring cells. In order to avoid performing this search operation repeatedly within a time step, particle IDs of neighboring particles are stored in an array for each particle.

All main time-step computations are performed by the CUDA kernels. However, the particle array is only copied from device memory to the host memory when the

Algorithm 1 The algorithm for the computations of one time step

```
Initialize time step
Project $\mathbf{u_i}$ and $\mathbf{r_i}$ with $\Delta t/2$:
    $\mathbf{u_i}^{n+1/2} = \mathbf{u_i}^n + \mathbf{a_i}^n \Delta t/2$
    $\mathbf{r_i}^{n+1/2} = \mathbf{r_i}^n + \mathbf{u_i}^{n+1/2} \Delta t/2$
Produce ghost particles for boundaries
Perform neighbor search:
    Compute $W_{\mathbf{ij}}$, $\nabla_{\mathbf{i}} W_{\mathbf{ij}}$, $V_{\mathbf{i}}$, $\mathbf{r_{ij}}$, $\mathbf{u_{ij}}$
Compute the correction tensor $\mathbf{A_i}$
Compute $k_{\mathbf{i}}^{n+1/2}$
Project $\rho_{\mathbf{i}}$ with $\Delta t/2$:
    $\rho_{\mathbf{i}}^{n+1/2} = \rho_{\mathbf{i}}^n + k_{\mathbf{i}}^{n+1/2} \Delta t/2$
Apply density filtering
Compute $p_{\mathbf{i}}$
Compute $\mathbf{M_i}^{n+1/2}$
Compute $\mathbf{Q_i}^{n+1} = \mathbf{Q_i}^n + \mathbf{M_i}^{n+1/2} \Delta t$
Compute $\mathbf{a_i}^{n+1/2}$
Correct particle velocity, position and densities:
    $\mathbf{u_i}^{n+1} = \mathbf{u_i}^n + \mathbf{a_i}^{n+1/2} \Delta t/2$
    $\mathbf{r_i}^{n+1} = \mathbf{r_i}^{n+1/2} + \mathbf{u_i}^{n+1} \Delta t/2$
    $\rho_{\mathbf{i}}^{n+1} = \rho_{\mathbf{i}}^{n+1/2} + k_{\mathbf{i}}^{n+1} \Delta t/2$
Apply APD
Finalize time step:    $t = t + \Delta t, \quad n = n + 1$
```

Table 6.1 Performance profile of the CUDA kernels.

Operation	Percentage of computational cost
CUDA Kernel 1	43.90%
CUDA Kernel 2	30.71%
CUDA Kernel 3	24.08%
Other CUDA operations	1.31%

program needs to write the outputs for the post-process. It should be noted that the neighbor interaction arrays, as well as the main particle array, have pre-allocated maximum sizes. Ghost particles are added after the end of the fluid particles on the array and their corresponding data are overwritten at each time step, while a variable holds the value of the actual particle number in order to define the end of the meaningful data. The same process applies to the particle neighbor interaction arrays, which also have variable sizes throughout the simulation.

Percentages of average computational time costs of the different CUDA kernel groups (1) over 100 iterations with $\approx 2.5 \times 10^5$ particles are provided in Tab. 6.1. Percentage of the CUDA kernel 1 reveals the impact of the serial ghost particle algorithm on the performance of the program. Here, it can also be inferred that any improvement on the neighbor searching algorithm may also lead to a significant increase in the performance. To demonstrate the speed-up achieved by the CUDA-based parallel algorithm of this study, the ratio of computational time required by the the serial Finite Volume solver of OpenFOAM to the time needed by the parallel SPH algorithm is plotted as a function of mesh resolution in Fig. 6.2 for the solution of the same problem. Generally, mesh-based algorithms are expected to be faster than mesh-free methods since they have fewer number of neighbors for each computational node and do not require updated neighbour lists throughout the simulation. As seen in this figure, the current GPU-parallelized SPH method notably outperforms the serial OpenFOAM particularly at higher resolutions although in this comparison, the time integration scheme used in the SPH method is second order Runge-Kutta whereas the one employed in the OpenFOAM is the first order Runge-Kutta (Euler) method.

6.3 Problem definition, numerical consistency and accuracy studies

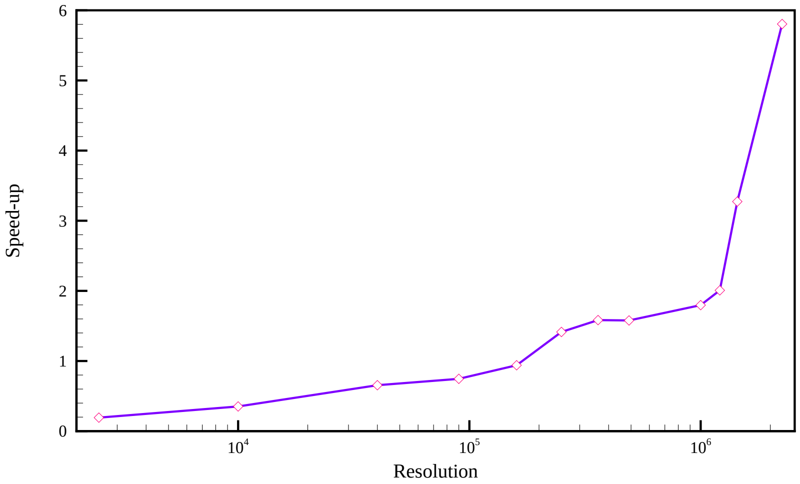

Figure 6.2 **Speed-up of the current CUDA based SPH solver with respect to the serial OpenFOAM solver.** Although the OpenFOAM requires smaller solution time at lower resolutions ($< O(5)$), significant speed-up is obtained by SPH for higher resolutions ($O(6) <$). "Resolution" corresponds to the number of particles and the number of cells in the grid for the SPH and the OpenFOAM, respectively.

The computational domain is a two-dimensional square one with a normalized size of unity. In order to avoid any confinement effect, a fully periodic unit domain is ensured by the periodic ghost boundary treatment. The particle resolution test is carried on with four different particle sizes, including $\approx 10^4$, 4×10^4, 2.5×10^5, and 10^6, and taking the physical parameters as tabulated in Tab.7.2. Results for root mean square velocity and defect number are calculated as a function of particle resolution and represented in Fig. 6.3a. As shown in this figure, the case with the total number of $\approx 2.5 \times 10^5$ particles exhibits the desired accuracy which is selected as a reference particle resolution. This resolution corresponds to the initial particle distance $\Delta x = 0.02m$, and the time step size is determined according to the CFL condition. With the aforementioned particle configuration, average computation time required for one time step iteration is $\approx 0.5s$ on an Nvidia Quadro RTX 5000 GPU.

To test the accuracy of the current numerical scheme, we performed a quantitative and qualitative verification test studies and compared the results with the data from the literature. The parameters used are tabulated in the last column of Tab.7.2. For the quantitative verification, the normalized velocity- velocity correlation calculated with SPH and the numerical results of Thampi et al. (2013) are demonstrated in Fig. 6.3b showing that our results perfectly match with the numerical data of Thampi *et al.* . Furthuremore, we performed a qualitative comparison between SPH results and the results of Thampi et al. (2014a) for the vorticity contours. A good agrrement

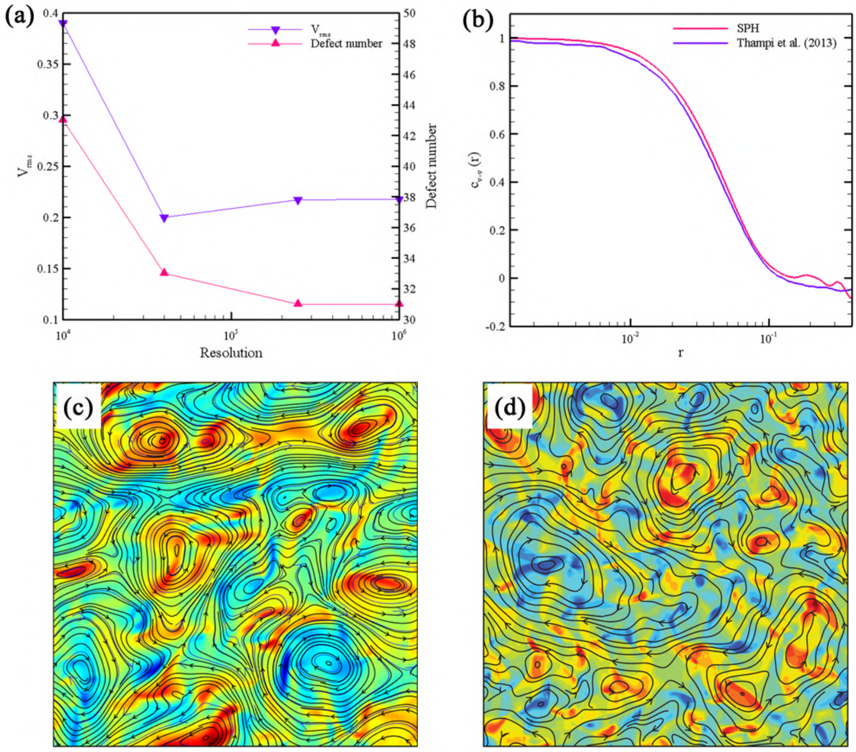

Figure 6.3 **Particle resolution independency and verification of the SPH code.** (a) Resolution independency test is performed for four different particle sizes. (b) Quantitative comparison of the current SPH method with the results of Thampi et al. (2013). Qualitative comparision of vorticity contours between (c) current SPH and (d) results of Thampi et al. (2014a) (Adapted with permission from EPL publishing group).

is observed between our results (Fig. 6.3c) and data of Thampi *et al.* (Fig. 6.3d).

6.4 Results

The coupled governing equations introduced in chapter 2 are solved using the SPH method. The parameters used are provided in the Tab.7.2, unless stated otherwise. These values lie within the ranges that were reported by Chandragiri, Doostmohammadi, Yeomans & Thampi (2020); Plan, Yeomans & Doostmohammadi (2021); Santhosh, Nejad, Doostmohammadi, Yeomans & Thampi (2020a). Furthermore, these values of the parameters satisfy the small order of Reynolds number condition which was reported by researchers (Nejad, Doostmohammadi & Yeomans, 2021). Zero initial velocity is used with a slightly perturbed nematic orientation as the initial condition and the quantitative results are taken at the statistically steady

Table 6.2 The parameters used in the simulations. Values are taken from Thampi et al. (2014a).

Parameter	value	value (verification test)
Γ	$0.4(Pa^{-1}s^{-1})$	$0.0136(Pa^{-1}s^{-1})$
λ	0.7	0.7
A, B and C	1, 1 and $0(Pa)$	0, 375 and $-375(Pa)$
K	$0.02(N)$	$1(pN)$
μ	$2/3(Pa.s)$	$0.5(Pa.s)$
ρ	$1(kgm^{-3})$	$1(kgm^{-3})$
ζ	$0.023(Pa)$	$0.0125(Pa)$

state.

As discussed earlier, there is no source of external energy in active fluids, and energy is injected by the particles themselves. Since nematic fluids are inherently unstable (Edwards & Yeomans, 2009), as the time progress, these instabilities reveal themselves in the form of vorticity. In Fig. 8.2, vorticity contours as well as streamlines are shown inside the computational domain for two different positive and negative activities at $\mu = 0.1 pas.s$. As can be seen in these figures, turbulent-like flow is created because of the existence of vortices inside the domain which consequently occurs due to the presence of activity that destroys the long-range nematic ordering. Particle alignments are calculated and shown in Fig. 8.2-c. In this figure, the orientation of the nematic director is observed clearly and it is seen that the variation of vorticity depends on the nematic directors.

It is common to use the kinetic energy per mass densityin Fourier mode, $E(w)$, to analyze the structure of the turbulent flow (Pope & Pope, 2000):

$$E(w) = \tfrac{1}{2}\langle \hat{u}_i(w)\hat{u}_i(w)\rangle, \tag{6.1}$$

where angular brackets $\langle . \rangle$ is the spatial average. In classic turbulent flow, a universal scaling was suggested by Kolmogorov, Levin, Hunt, Phillips & Williams (1991) as $E(w) \approx w^{-5/3}$, where $w = 2\pi/l$ is the wavenumber. In the active fluid, however, in the absence of an external source, energy is injected by the active term. Many researchers have tried to study the kinetic energy in the active fluid. Most recently, Alert et al. (2020a) proposed a universal scaling for the active nematics, yet disregarding the topological defects. In the present study, kinetic energy is calculated for different resolutions, and the results are presented in Fig. 7.7. In the active fluids, the energy is injected at the wide ranges of length scales, and then, it

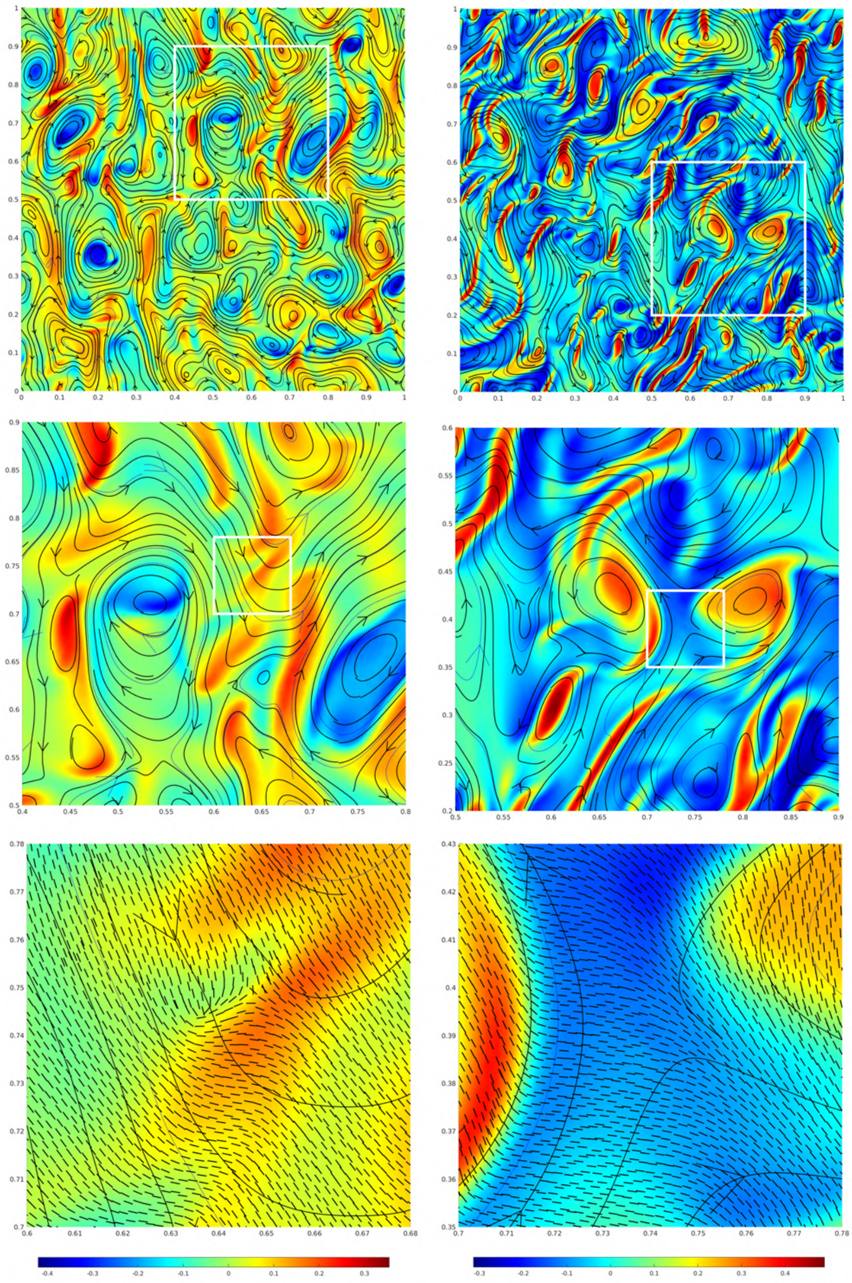

Figure 6.4 **Vorticity contour and streamlines.** Results are corresponding to $\zeta = 0.03$ (left column) and $\zeta = -0.03$ (right column) at three different length scales. Lower subfigures corresponds to close up views and nematic directors are also shown only in last row. All results are taken at physical time, t = 500s.

is cascaded towards the small scales and finally is dissipated due to the viscosity. It is also seen that the scaling is the same for all resolutions at sufficiently large scales. By decreasing the length scale (which is equivalent to an increase in wavenumber), this relation changes such that at the intermediate scales, it becomes w^{-4}. It should be noted that the very small scales requires higher resolutions, which will be investigated in our future studies. Nevertheless, with the current resolution, the calculated energy spectrum is in a good agreement with the results of previous studies (see for example figure 4 of Alert et al. (2020a)). In passing, it is worthy to state that the curve in Fig. 7.7 is obtained for the case with small Reynolds number where inertial effects are negligible. We will shown in the next chapter that the inertia forces notably alter the characteristic of kinetic energy spectrum.

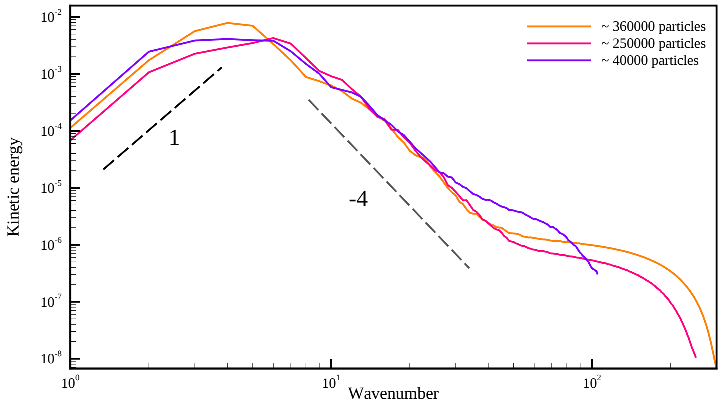

Figure 6.5 **Spectrum of kinetic energy for different particle resolutions.** Dashed-line with +1 and -4 slopes are presented to compare the SPH results with the universal scaling suggested by Alert et al. (2020a).

Referring back to Fig. 7.7, one can see that the vortices with various scales exist in the domain. However, it is conventional to select a specific length scale and calculate the important parameters based on it. To study the length scale of the problem, one can use velocity (vorticity)-velocity (vorticity) correlation curve inside the domain. The normalized correlation function of property $f(r)$ is defined as (Pope & Pope, 2000):

$$C_{f-f}(r) = \frac{\langle f(r).f(0) \rangle}{f(0)^2}, \tag{6.2}$$

where r is the spatial position from the point of interest, $r = 0$. In the current study $r = 0$ is located at the center of the domain and r is selected to vary along the horizontal center-line direction. This function is calculated for the vorticity and is shown in Fig. 6.6. Although similar behavior is observed between our computed correlation and those reported by Thampi et al. (2014b), to further reveal the high fidelity of the proposed SPH model, in this study a same simulation is also performed using the OpenFOAM and the results are comparatively provided in Fig. 6.6. As the distance between the point of interest and its all neighbours within the entire flow domain increases, the correlation function tends to become zero, indicating the absence of correlation between two positions spaced far apart, which is also in the agreement with the result of OpenFOAM.

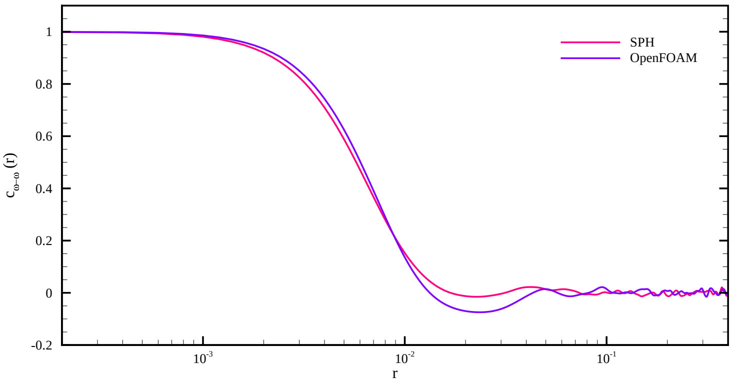

Figure 6.6 **Vorticity-vorticity correlation.** Results are obtained by SPH and OpenFOAM.

Length scale (l) of active nematics flow can be calculated quantitatively using the correlation function such that $C_{f-f}(l) = 0$ (or in some studies two-tenths of the maximum correlation value (Thampi et al., 2013)) which is the point where the sign of the statistically large distributed vortices is being changed. It is also possible to define the characteristic length scale based on the active fluid properties. As proposed by Hemingway, Mishra, Marchetti & Fielding (2016), the characteristic length scale can be calculated as $l_Q \approx \sqrt{K/\zeta}$. Also, the characteristic velocity is defined as $v_Q \approx l_Q\zeta/\Gamma$. Consequently, the Reynolds number (Re) is defined as $\mathrm{Re} = \rho v_Q l_Q/\mu$. Adopting these scales, the Reynolds number of $\mathrm{Re} \approx 0.075$ is determined for our simulations.

As mentioned earlier, in the study of Alert et al. (2020a), the defect formation was neglected, which plays an important role in the nematic flow. Thus, herein, we focused on the defect formation in our simulation. The large-scale presentation of the nematic directors is shown in Fig. 6.7-a and -b for positive and negative activities, respectively. The topological defects are the important characteristics of active nematics. These defects are the points where there are mismatches between the director of neighboring particles. There are mainly two kinds of defects in the active nematics, positive half and negative half, which are shown by red and blue symbols, respectively in Fig. 6.7. In order to detect these defects in the flow, every single particle is selected and alignments of its surrounding particles are compared with each other. If the surrounding particles alignments are similar to what is shown in Fig. 6.7-c, that particle is labeled as a defect point. The negative half defect has a symmetric structure, so it is balanced inside the flow, whereas the positive half does not have a balanced structure which makes it motile (Doostmohammadi et al., 2018). Because of this motility, when these defects are created in pairs, +1/2 pairs move away from each other. Generally speaking, there is a cycle in active nematic flow that describes its behavior; instabilities in the flow field lead to the formation of local wall structures in the nematic director field. Walls are the lines that surround a nematic region and separate these regions from each other, and they are the points where the topological defects are being created by active stress. Due to the gradients in the nematic field around the defects, these defects move and annihilate and restore the nematic order, which again triggers the instability, and this cycle repeats (Thampi & Yeomans, 2016).

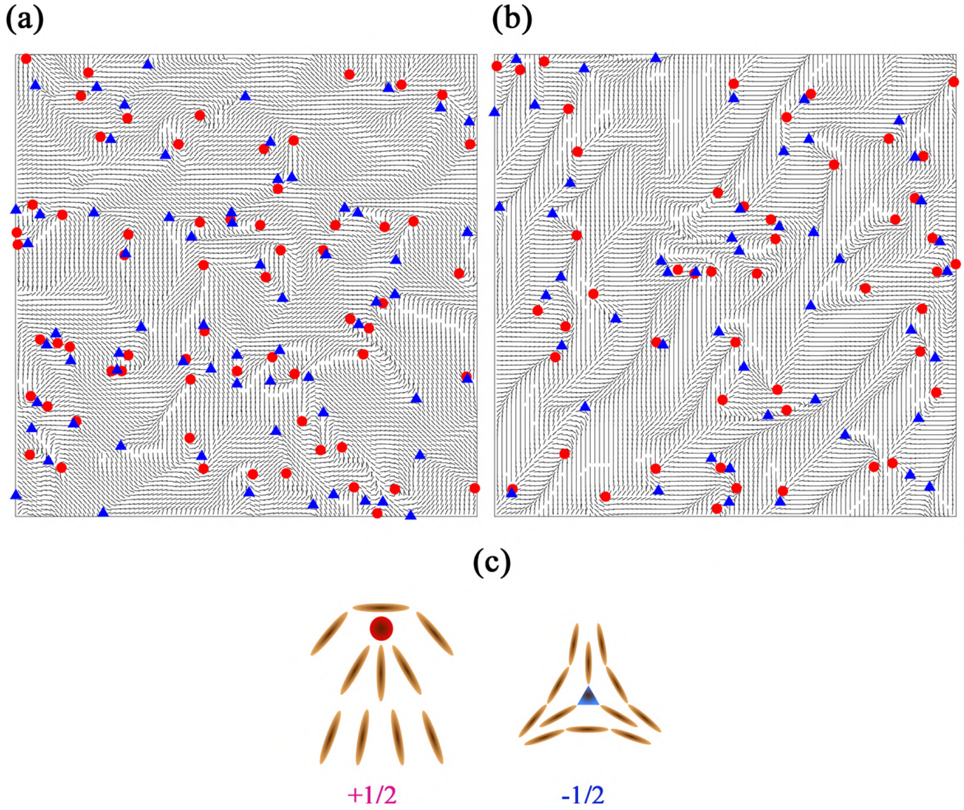

Figure 6.7 **Particle alignment and topological defects.** Results are corresponding to $\zeta = 0.023$ (a) and $\zeta = -0.023$ (b). A comet-like, $+1/2$, and a trefoil-like, $-1/2$ defects are shown in red filled circles and blue filled triangles respectively. Schematic representation of defects (c).

As stated above, active walls are the places of defect formation, thus it would be beneficial to plot and discuss it in detail. In order to demonstrate the walls inside the domain, it is proper to plot the contour of the nematic order (q), as shown in Fig. 6.8. This value varies between 0 and 1, while the most of domain has the value of $q \approx 1$ which is shown by the dark red color. Along the nematic walls, on the other hand, q gets a smaller value, which is colored by light red in Fig. 6.8. It is important to note that, as mentioned earlier, all the defects are located on the wall where $q \neq 1$.

Since the activity induces energy into the nematic flow and influences its characteristics, it is important to evaluate its effect on the flow. To define the characteristic

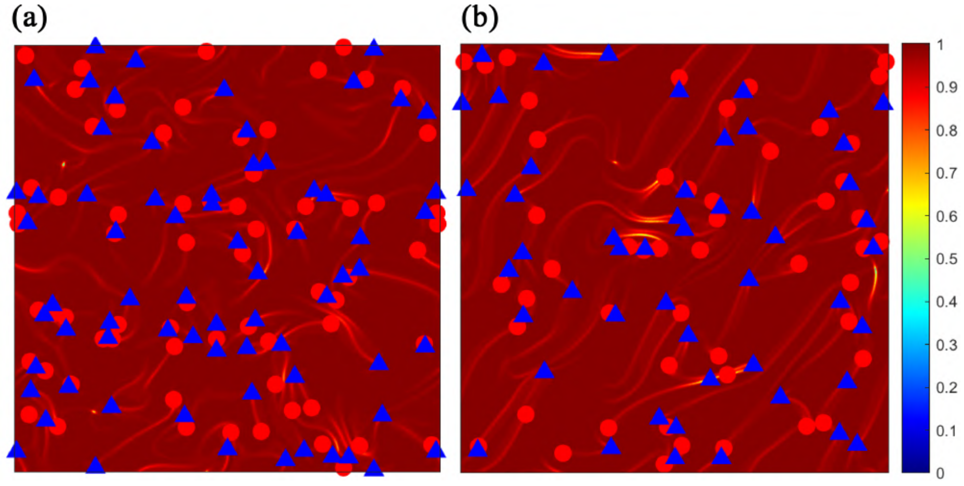

Figure 6.8 **Contour of the nematic order.** Results are corresponding to $\zeta = 0.023$ (a) and $\zeta = -0.023$ (b).

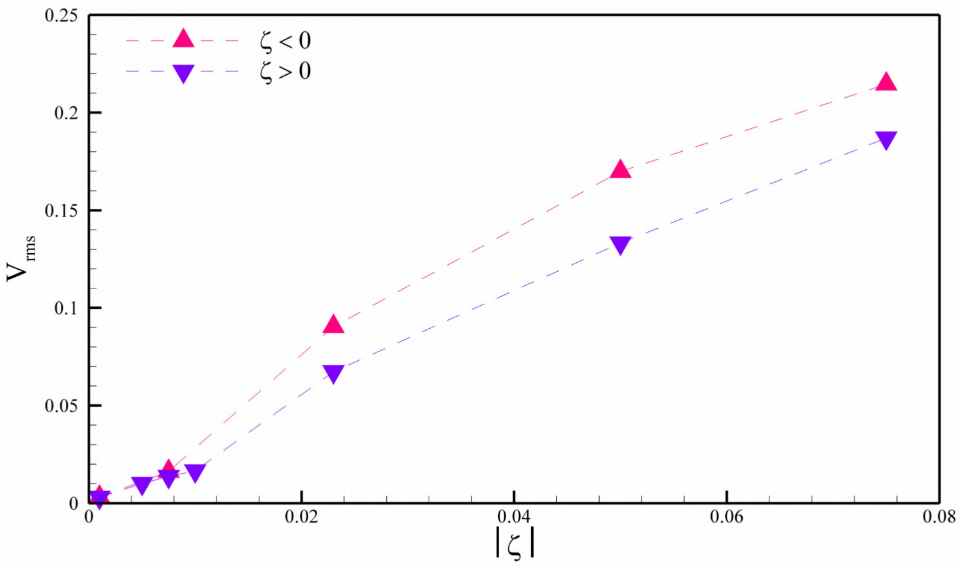

Figure 6.9 **Effect of activity on the root mean square of velocity for extensile and contractile suspensions.** The root mean square of the velocity increases by increase in the absolute value of the activity parameter.

velocity in turbulent-like flow, it is common to use the root mean square of velocity (V_{rms}), which, as an averaging term, includes both positive and negative velocity fluctuations. This property is calculated under the effect of various amounts of activity and demonstrated in Fig. 6.9 for extensile ($\zeta > 0$) and contractile ($\zeta < 0$) suspensions. As it is seen in this figure, both extensile and contractile nematics behave similarly, which means that the increase in the absolute value of activity elevates the value of V_{rms}. It should be noted that the dependency of V_{rms} on the activity is stronger for contractile than for the extensile, hence $\zeta < 0$ stays above the $\zeta > 0$ curve. Moreover, it is seen that these graphs increase monotonically with respect to activity.

The dependency of V_{rms} on the activity is directly related to the velocity jets induced in nematics by defects in the nematic flow. The average flow induced by the defects is calculated for +1/2 defects and shown in Fig. 6.10. Typically +1/2 defects are associated with a vortex dipole as shown in this figure. This defect is self-propelled in the direction shown by the arrow. The flow pattern presented in Fig. 6.10 is consistent with that obtained by an analytical solution using Green's function (Giomi, 2015).

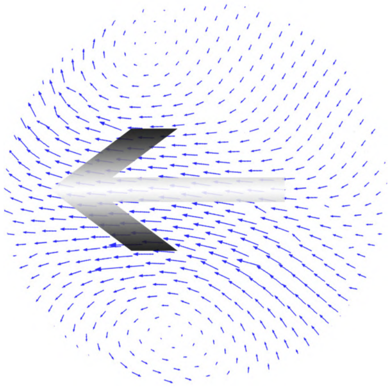

Figure 6.10 **Average +1/2 defect flow.** Results is taken at $\zeta = 0.05$. The comet-like, +1/2 defect results in the pair of vortices.

As mentioned before, the important advantages of SPH over other numerical methods is its Lagrangian nature. With this feature, one can track every single nematic particle inside the flow and evaluate the variation of its properties during the simulation. To exploit this feature, we took five nematic particles from different initial positions and track their trajectories during the simulation. Pathlines of these particles are shown in Fig. 6.11 for four different activities, $\zeta = -0.001, \pm 0.023$, and -0.25. Initial positions are encircled and each point in pathlines represents a particle position in a specific time step. As expected, by increasing the absolute value of activity, lengths of pathlines increase. This happens due to the high energy injection at higher activities. Nematic particles consume this energy to move faster and consequently further. At the smaller values of activity, however, viscous term dominates the flow and dissipates the input energy. As a result, the pathlines of the nematic particles are shorter for the smaller values of activity. Interestingly, the pathline for the $\zeta = -0.023$ is longer than of $\zeta = 0.023$ which was previously observed in Fig. 6.9 which explains the difference between the V_{rms} curves for extensile and contractile suspensions. This shows that the contractile ($\zeta < 0$) suspension converts more input energy into kinetic energy which leads to a larger velocity and displacement.

In order to track the large groups of particles, we divided the domain into four regions and colored the particles inside of each region to distinguish the particles during the simulation. This leads to the mixing of the particles as shown in Fig. 6.12. It should

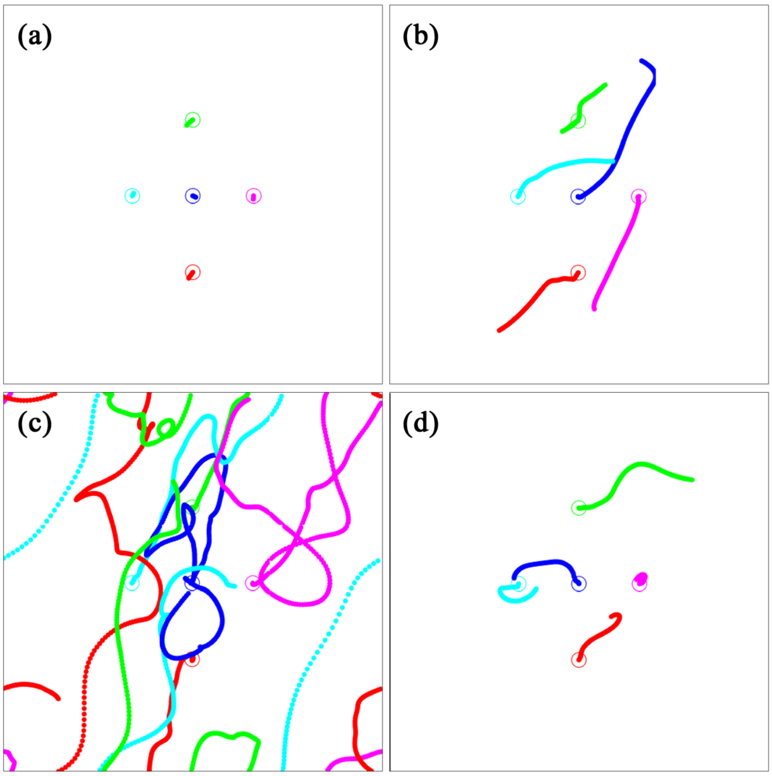

Figure 6.11 **Nematic particles pathline.** Results are taken at the same physical time for $\zeta = -0.001$ (a), $\zeta = -0.023$ (b), $\zeta = -0.25$ (c), and $\zeta = 0.023$ (d).

be emphasized that the particles inside the whole domain have identical nematic and hydrodynamical properties and their color only represents their initial position. As demonstrated in Fig. 6.13, while advancing in time, the four regions start to blend with each other, and by increasing time adequately, a uniform distribution of particles from all regions is obtained, which demonstrates the uniform mixing of the nematic particles. It can be inferred that the particles are free to move in any direction, but their mutual interactions dictate which direction they move in. Moreover, the dynamics are in fact deterministic, the seemingly-randomness comes from the fact that the system is chaotic. Figure 6.13 also demonstrates the effect of activity strength on the mixing behavior of active nematics. $t_1 = 45 < t_2 = 252 < t_3 = 500$ Sec. are the real physical times at which snapshots of the particle positions are taken. As expected, the case with the higher value of the activity reaches complete mixing faster whereas those with the lower values of activity need a comparatively longer duration. The comparison of the first and the second row of Fig. 6.13 indicates the high capability of contractile nematics for the mixing. Thus, for the mixing purpose, contractile nematics perform better than the extensile one and the operation speed can be hastened by increasing the activity.

Thus far, we have focused on the effect of activity on the active nematic flow characteristics. As described in chapter 2, in the formulation of the nematodynamics,

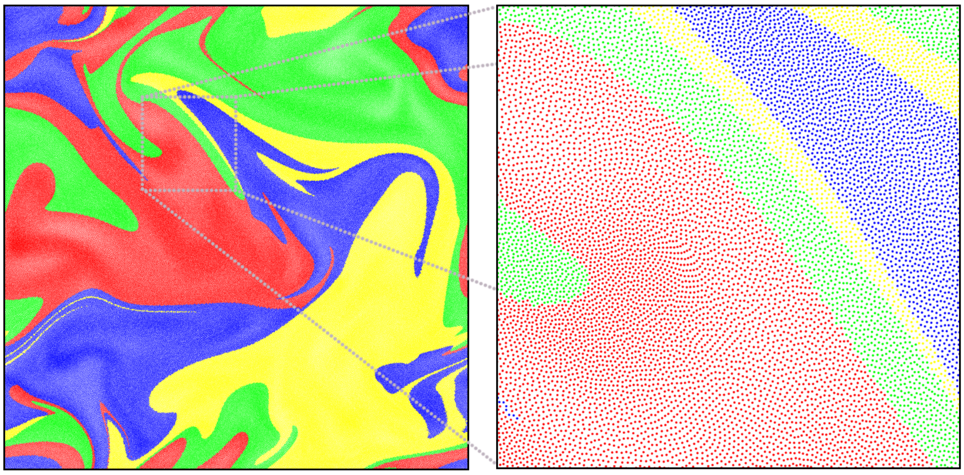

Figure 6.12 **Particle representation of mixing in the active nematics.** Results correspond to $\zeta = 0.023$ and $K = 0.1$ at $t = 500s$. The selected section is magnified and demonstrated in the inset.

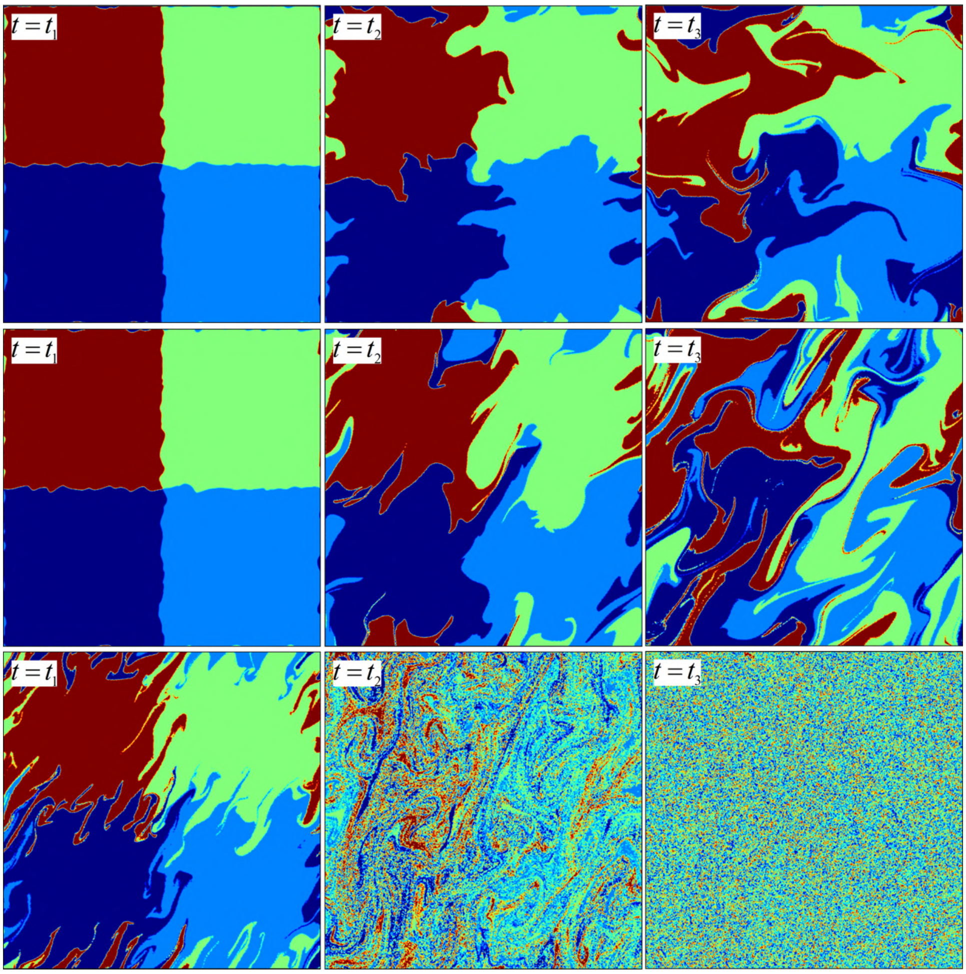

Figure 6.13 **Effect of activity parameter on the mixing.** Comparison of mixing for $\zeta = 0.023$ (first row), $\zeta = -0.023$ (second row), and $\zeta = -0.25$ (last row). Each column corresponds to the identical physical time with $t_1 < t_2 < t_3$.

elastic constant, K was introduced, which plays an important role in the molecular field tensor, $\mathbf{H}$. Figure 6.14-a demonstrates the variation of the flow field with K. As can be seen from this figure, the increase in the value of K augments the vortex sizes, which is compatible with the relation $\sqrt{K/\zeta}$ describing the length scale of the nematic flow. Physically, this trend can be investigated considering the energy consumption in active nematics. The injected energy by activity is consumed for the creation of topological defects but at the expense of free energy. Consequently, as shown in Fig. 6.14-b, defect number strongly depends on the value of K and decreases with an increase in K. Moreover, as discussed earlier, there is a coupling between defects and fluid instabilities by creation and annihilation cycle of topological defects. These instabilities, on the other hand, are the reason of the vortex creation. By decreasing the defect number, instabilities become weaker and a few vortices are created in the flow with the larger size hence covering the whole domain. Similarly, lower values of K result in higher instability in which the flow is much more chaotic. This behavior is demonstrated in Fig. 6.14-c which shows the snapshots of the flow mixing for different values of K. It should be noted that all of the snapshots are taken at the same physical time, $t = 500$. Interfaces between different colors exhibit the instability of the flow. As shown in this figure, the interface at $K = 0.1$ is smoother in comparison with the flow at $K = 0.02$, which justifies the inverse effect of K on the instability of the flow. Thus, to increase the mixing efficiency, it is suggested to use the smaller value of K. .

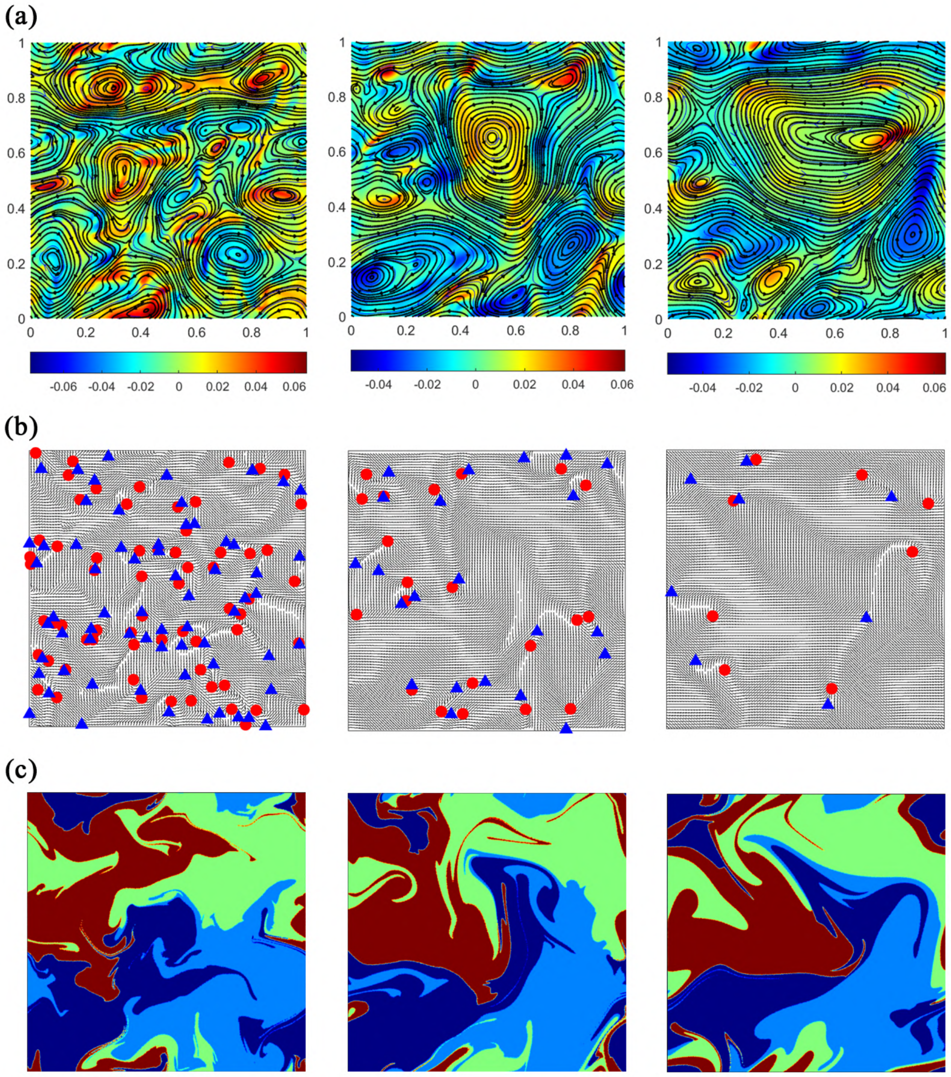

Figure 6.14 **Effect of elastic constant on the flow, defects and mixing.** (a) Contours of vorticity and streamlines, (b) topological defects and nematic ordering, and (c) mixing. First, second and third columns represent $K = 0.02$, $K = 0.05$, and $K = 0.1$, respectively.

7. Nematic order condensation and topological defects in inertial active nematics

7.1 Introduction

As with the Giomi (2015)'s theoretical and numerical analyses, the majority of the previous studies have considered the micro-scale active turbulence, e.g. in cellular monolayers, bacterial suspensions and subcellular filaments-motor protein mixtures, where the Reynolds number is negligible ($\mathrm{Re} \approx 0$), and viscous dissipation completely dominates over any inertial effects (Alert et al., 2022). However, in many other realizations of active matter, for example swimming organisms in environmental flows (Houghton, Koseff, Monismith & Dabiri, 2018) and artificial active spinner suspensions (Kokot, Das, Winkler, Gompper, Aranson & Snezhko, 2017), the inertial effect becomes significant, and the Reynolds numbers are non-zero (Klotsa, 2019).

Table 7.1 Values of Reynolds number based on different length scales.

$\nu/K\Gamma$	Active length scale (Re)	Taylor length scale ($\mathrm{Re_T}$)	integral length scale ($\mathrm{Re_I}$)
125	0.03	0.0002	0.005
12.5	0.7	0.0023	0.03
1.25	250	8.2227	191

Recent studies have begun to reveal interesting impacts of inertia on self-propulsion of active particles and inertial effects on active turbulence (Chatterjee, Rana,

---

This chapter is a slightly modified version of "Nematic order condensation and topological defects in inertial active nematics" published in "Physical Review E" by "R. Saghatchi, M. Yildiz, and A. Doostmohammadi"

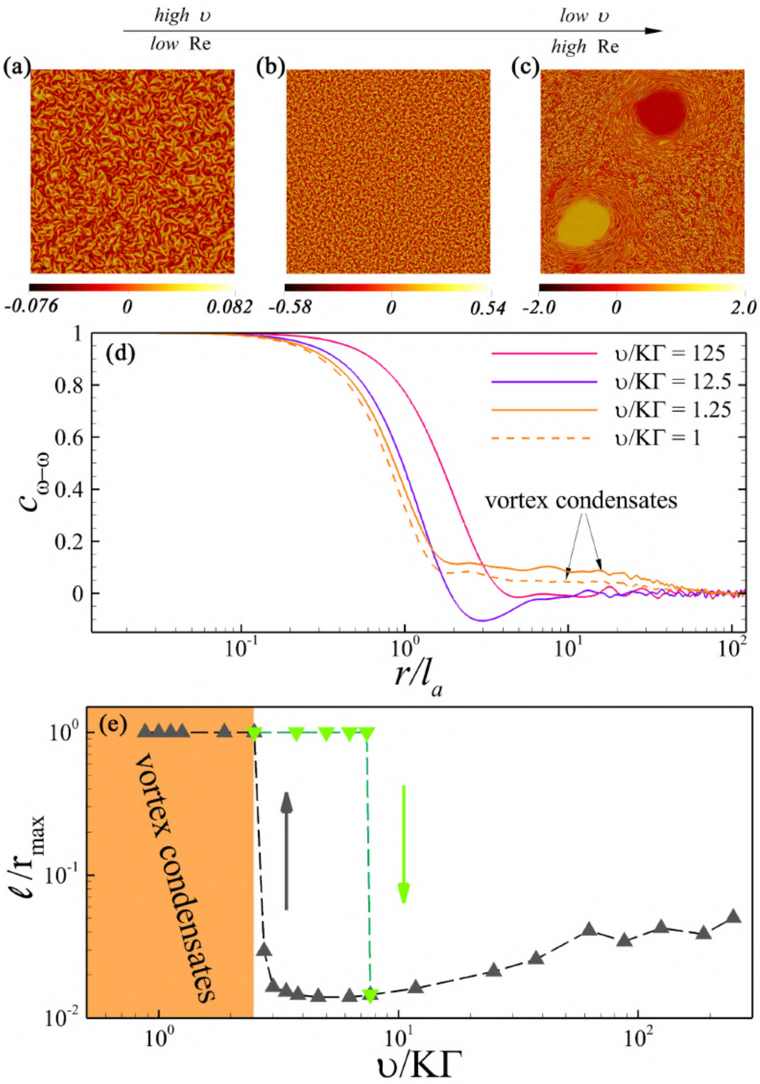

Figure 7.1 **Active turbulence and vortex-condensates**. Snapshots of the flow vortices for incrementally decreasing viscosities: vorticity contours for (a) $\nu/K\Gamma = 125$ with Re ~ 0.03 (equivalent to $Re_{\mathrm{T}} = 0.0002$ using the Taylor microscale and $Re_{\mathrm{I}} = 0.005$ using the integral scale to define the Reynolds number), (b) $\nu/K\Gamma = 12.5$ with Re ~ 0.7 (equivalent to $Re_{\mathrm{T}} = 0.0023$ using the Taylor microscale and $Re_{\mathrm{I}} = 0.03$ using the integral scale), and (c) $\nu/K\Gamma = 1.25$ with Re ~ 250 (equivalent to $Re_{\mathrm{T}} = 8.2227$ using the Taylor microscale and $Re_{\mathrm{I}} = 191$ using the integral scale). (d) Effect of viscosity on vorticity-vorticity correlations $C_{\omega-\omega}(r)$. The distance r is normalized by the active length scale $l_a = \sqrt{K/\zeta}$. (e) Characteristic vorticity length scale as a function of viscosity. Upon decreasing viscosity, after an initial decrease in the size of vortices, condensates spanning the entire system are formed. The length scale (ℓ) equals to the length r at which $C_{\omega-\omega}(r) = 0$. Green data points represent an incremental increase in viscosity and show the presence of a hysteresis loop, indicating a discontinuous transition to the vortex-condensate state.

Simha, Perlekar & Ramaswamy, 2021; Hamel, Fisch, Combettes, Dupuis-Williams & Baroud, 2011; Khair & Chisholm, 2014; Koch & Wilczek, 2021; Linkmann, Boffetta, Marchetti & Eckhardt, 2019; Löwen, 2020; Scholz, Jahanshahi, Ldov & Löwen, 2018; Wang & Ardekani, 2012). It is shown that increasing the inertia of active particles can result in a transition from active turbulence to flocking in polar active matter (Chatterjee et al., 2021). Moreover, using a one-fluid model of an active matter with hyper viscosity, or a piece-wise constant viscosity, it was found that above a certain Reynolds number active matter can manifest vortex-condensate formation (Linkmann et al., 2019; Linkmann, Marchetti, Boffetta & Eckhardt, 2020) in analogy with the condensates in classical driven 2D turbulence, where inverse energy cascade results in the accumulation of energy at larger scales and condensate formation (Boffetta & Ecke, 2012). More recently, it was shown how the interplay of advective inertia and friction can affect transitions between active turbulence, inertial regime, and tamed inertial active turbulence in active nematic systems (Koch & Wilczek, 2021). While these studies have provided important insights into the flow features of dense active matter in the presence of inertia, less is known about how inertial effects combined with activity impact the orientational organization of active elongated particles. In particular, singularities in the orientation field, known as topological defects, are increasingly emerging as important centers of self-organization in biological systems (Maroudas-Sacks, Garion, Shani-Zerbib, Livshits, Braun & Keren, 2021), with potential biological functionalities (Doostmohammadi & Ladoux, 2022; Kawaguchi, Kageyama & Sano, 2017; Meacock et al., 2021; Saw, Doostmohammadi, Nier, Kocgozlu, Thampi, Toyama, Marcq, Lim, Yeomans & Ladoux, 2017) and how their dynamics are affected by inertial effects is not yet explored.

Here, we report on the numerical investigation of the flow and nematic features of inertial active matter. In order to investigate the fundamental impact of the fluid inertia on the active flow behavior, a continuum model of active nematics is employed. We start by showing the emergence of vortex condensates and then examine its impact on the orientational order and defect density. We then show that not only the defect density, but also the flow around defects get altered within the condensate state and finally show how these combined changes in flow, director, and defect patterns affect energetic features of the active turbulence.

7.2 Problem statement

To solve the coupled governing equations OpenFOAM package is used. The simulation domain consists of a 2D square of size 200 × 200, which is discretized using

Table 7.2 Values of model parameters employed in the numerical simulation, unless stated otherwise.

Parameter	value
Γ	$0.4(mN^{-1}s^{-1})$
λ	0.7
A	$1(Nm^{-1})$
K	$0.02(Nm)$
ζ	$0.03(Nm^{-1})$
ρ	$1(Ns^2m^{-3})$
ν	$[0.01, 0.1, 1.0](m^2s^{-1})$

the Cartesian grid with two different resolutions, 1024×1024, and 2048×2048, and the time step size is controlled through the CFL condition (Courant et al., 1928; Ferziger et al., 2002). Gauss Linear discretization (Moukalled et al., 2016) is used for gradient, divergence and laplacian terms, and the PISO algorithm (Versteeg & Malalasekera, 2007) is utilized for the velocity- pressure coupling. The time marching is performed based on the Euler scheme (Ferziger et al., 2002). Periodic boundary condition is enforced on the boundaries. Unless otherwise stated, the parameters used in simulations are according to Tab.7.2. Since in this study we are mainly interested in the impact of varying the viscosity and activity of the system, dimensionless viscosity $\nu/K\Gamma$ and dimensionless activity ζ/A, are defined. Moreover, Reynolds number is defined as $\mathrm{Re} = l_a V_{\mathrm{rms}}/\nu$, where $l_a = \sqrt{K/\zeta}$ is the active length scale (Giomi, 2015) and V_{rms} is the emergent root-mean-square velocity of the system that varies for different activity and viscosity values. In order to compare the values of the Reynolds number with the studies of vortex condensate formation in classic turbulence (Boffetta & Ecke, 2012; Gallet & Young, 2013), the corresponding values of Reynolds numbers are also reported based on the Taylor microscale and the integral scale (Pope & Pope, 2000) (Table 7.1 and Fig. 7.1). The Reynolds number based on the Taylor microscale is calculated using $\mathrm{Re}_{\mathrm{T}} = \lambda V'_{\mathrm{rms}}/\nu$, where, $\lambda = V'_{\mathrm{rms}}\sqrt{15\nu/\epsilon}$ is the Taylor microscale with $\epsilon = 2\nu < E_{ij}E_{ij} >$ denoting the kinetic energy dissipation rate and E_{ij} represents the strain rate tensor. V'_{rms} is the rms of the fluctuating component of the velocity. The Reynolds number based on the integral scale (Re_{I}) is calculated using $\mathrm{Re}_{\mathrm{I}} = L_{\mathrm{I}}V_{\mathrm{I}}/\nu$, where the integral length scale L_{I} and integral velocity scale V_{I} are defined as $L_{\mathrm{I}} = \int_0^\infty k^{-1}E_k\,dk \Big/ \int_0^\infty E_k\,dk$, and $V_{\mathrm{I}} = \sqrt{2\kappa}$, respectively (Pope & Pope, 2000; Urzay et al., 2017). Here, $E_k = \frac{1}{2}\langle \hat{u}_i(k)\hat{u}_i(k)\rangle$ is the kinetic energy spectrum, k is the wave number, and $\kappa = \langle u_{ij}u_{ij}/2\rangle$ is the spatially averaged kinetic energy.

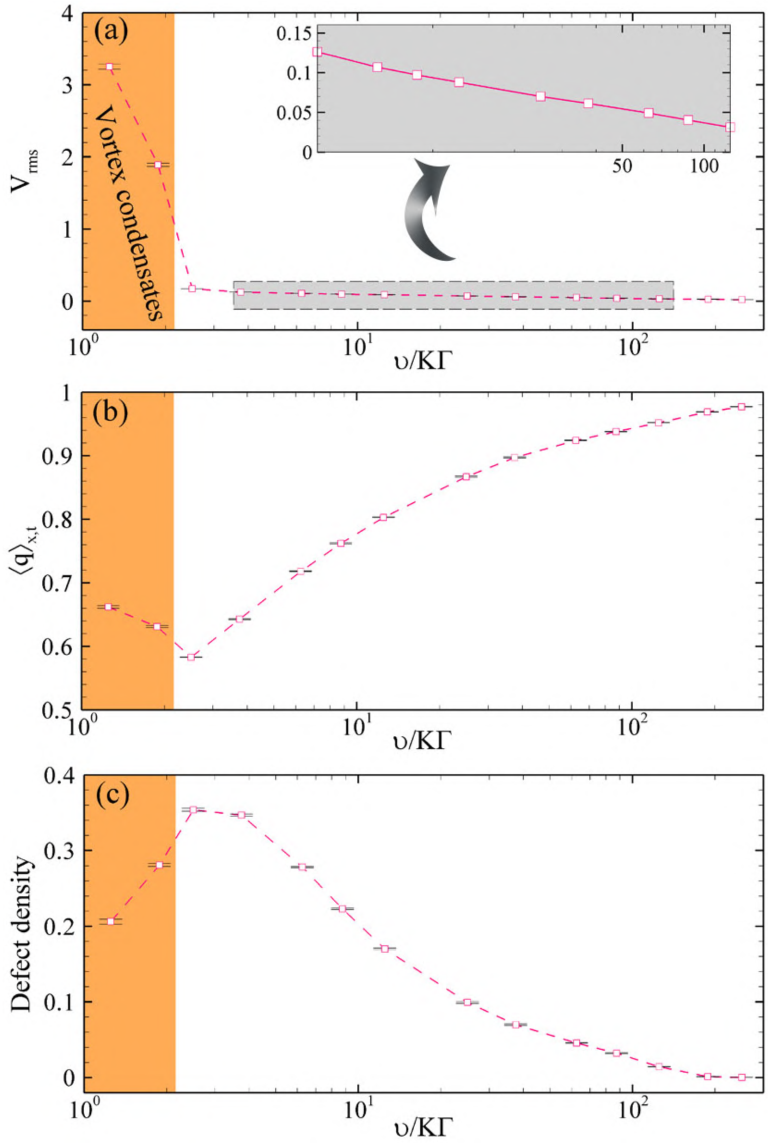

Figure 7.2 **Quantification of viscosity impact on flow and orientation properties of active nematics.** Effect of viscosity on (a) rms-velocity V_{rms}, (b) magnitude of the nematic order, and (c), defect number, before and after the transition to the vortex-condensate state. Inset in sub-figure (a) shows the semi-log plots of the rms-velocity as a function of the logarithm of viscosity, highlighting its logarithmic decay with viscosity.

We begin by qualitatively assessing the impact of increasing the inertia of the active fluid on the flow patterns by incrementally reducing the kinematic viscosity coefficient. Figure 7.1 demonstrates the vorticity contours for three representative viscosities. Upon reducing the viscosity, the size of the vortices becomes smaller, and the strength of vortices is enhanced (Fig. 7.1a,b). Similar to the classical turbulence by reducing the viscosity, and thus increasing Reynolds number, large eddies become unstable and begin to break up, transferring their energy to comparatively smaller eddies (Boffetta & Ecke, 2012). Moreover, in agreement with the reverse cascade dynamics in 2D classical turbulence, a further increase in the Reynolds number results in the accumulation of energy from smaller scales towards the larger scales leading to the emergence of a vortex condensate in the form of two large counter-rotating vortices that span the entire system (Fig. 7.1c). It is important to note, however, that in comparison to the classical inertial turbulence that is driven by external forcing (Boffetta & Ecke, 2012), the transition to vortex-condensate here is driven by active stress generation. The formation of vortex-condensates can best be represented quantitatively through measuring the vorticity-vorticity correlation function $C_{\omega-\omega}(r) = \langle \omega(r).\omega(0) \rangle / \langle \omega(0)^2 \rangle$, where $\omega = \partial_x u_y - \partial_y u_x$ (Fig. 7.1d). Before and after the emergence of the condensate, different characteristic length scales of decay are exhibited: before the emergence of the condensate, by increasing the Reynolds number, the correlation length decreases, while after the emergence of the vortex condensate, the characteristic length scale is set by the system size that encompasses the two giant vortices (Fig. 7.1d,e).

Similar flow patterns of vortex condensate formation were reported earlier based on the one-fluid model of active polar matter with both hyper-viscosity and piece-wise constant viscosity, where it was demonstrated that a discontinuous, subcritical phase transition governs the emergence of the vortex condensate state (Linkmann et al., 2019,2). By performing the hysteresis analysis, we confirmed that the crossover to the condensate state in inertial active nematics also shows a hysteresis effect, indicating a discontinuous transition to the vortex-condensate state in active nematics (Fig. 7.1e).

It is further shown recently that in active nematics although the energy budget associated with advective inertia could be smaller compared to active and dissipative energies, the effect can accumulate over time leading to large-scale flow patterns (Koch & Wilczek, 2021).

In addition to the change in the size of the flow patterns, condensate formation is accompanied by a significant increase in the strength of the flow. This can be quantified by measuring the averaged rms-velocity V_{rms} of the entire system after reaching a statistical steady-state, which shows up to an order of magnitude enhancement in the velocity upon transition to the vortex-condensate state (Fig. 7.2a). Moreover, a closer look at the variation of the velocity beyond the transition point into the vortex-condensate state reveals a logarithmic decay of the rms-velocity with viscosity, as exemplified by the semi-log plot in the inset of Fig. 7.2a.

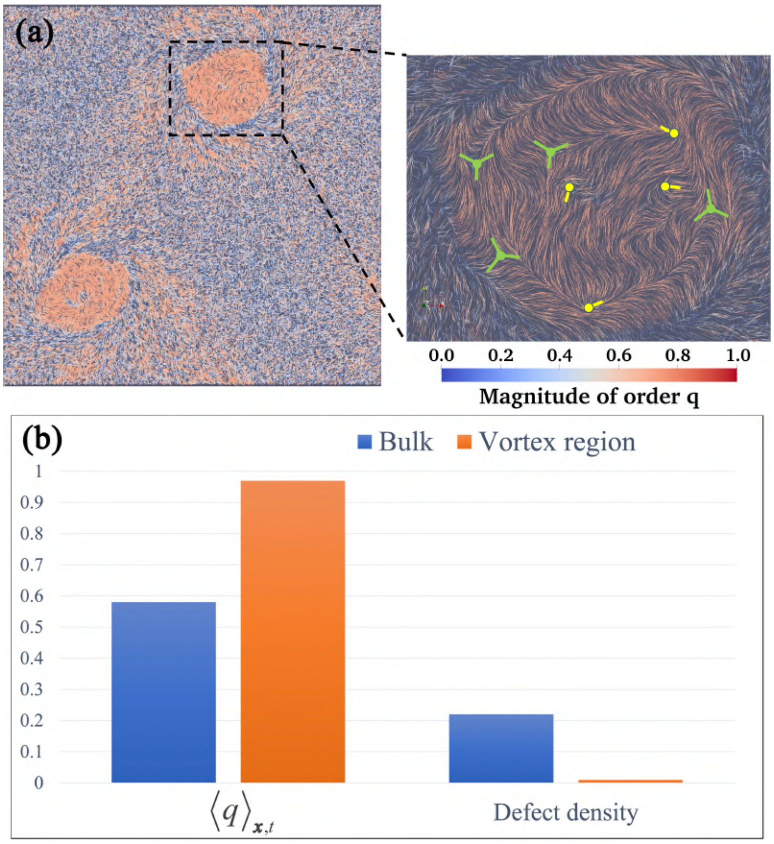

Figure 7.3 **Nematic order condensation**. (a) snapshots of director field and topological defects for vortex condensates case. Colormap indicates the magnitude of the nematic order q, and $+1/2$ and $-1/2$ topological defects are marked by yellow comets and green triangles, respectively.(b) Averaged values of the magnitude of order $\langle q \rangle_{\mathbf{x},t}$, and defect density calculated separately inside giant vortices and the bulk of the system excluding the giant vortices.

We next asked what would the consequences of such drastic changes in the strength and patterns of the flow be on the orientation field of the active nematic particles. To test this, the magnitude of the nematic order averaged over time and space $\langle q \rangle_{\mathbf{x},t}$ was measured for incrementally decreasing values of viscosity (Fig. 7.2b). Interestingly, the initial melting of the nematic order before the condensate formation is followed by an increase in orientational ordering within the vortex-condensate state. This is further accompanied by changes in topological defects density within the system, which after an initial increase with decreasing viscosity, begins to fall as the vortex-condensate is established (Fig. 7.2c). A closer look at the director field associated with the vortex-condensate state reveals the underlying mechanism for such changes in the nematic order and topological defect density: once the vortex-condensate forms, within the two giant vortices, a nearly perfect nematic order is established that is only disrupted by few topological defects (Fig. 7.3a), while the bulk of the system is characterized by disordered domain laden with a high density of the topological defects. As a result of this *order condensation* within the giant vortices, the magnitude of the order increases within the condensate phase, which is accompanied by a drop in the total defect density.

To explain the reason for the reduction/increase in defects population/orientational order at the condensate state, we quantified the nematic order within and outside of the vortex condensate region, showing clearly that the emergence of giant vortices is accompanied by the enhancement of the order and thus fewer defects within the condensates (Fig. 7.3b).

The mechanism for this can be demonstrated in a simplified form by approximating a giant vortex as an ideal Rankine vortex with the velocity profile in the polar coordinate $(u_r = 0, u_\theta, u_z = 0)$, with:

$$u_\theta = \frac{\Lambda}{2\pi} \begin{cases} r/a^2, & r \leq a \\ 1/r, & r > a \end{cases} \tag{7.1}$$

where Λ is the strength of the circulation of Rankine vortex and a is the vortex core size. This results in finite vorticity $\omega_z = \Lambda/(\pi a^2)$ and solid body rotation in the core region. An approximately constant vorticity across the giant vortex region is evident from the snapshots of the vortex-condensate (Fig. 7.1c). Previous works have established that ‘walls’ of large nematic distortion and topological defects are typically formed in the regions between separate vortices (Giomi, 2015; Thampi & Yeomans, 2016). Therefore, here, as a result of the constant vorticity and an approximate solid body rotation within the giant vortex there is only a weak destabilizing effect from variations in vorticity to frustrate the nematic order and as such higher order is expected within the vortex condensates.

As such, the orientational order and topological defects display different features within the giant vortices and the bulk of the system in the condensate phase. To gain further insights into the potential impact of varying viscosity and also the distinction between the bulk and the vortex region, we measured the average flow around topological defects. It is well-established that in active turbulence with negligible inertia, comet-shaped $+1/2$ defects show propulsive motion within the system, as evident from the average flow at the highest value of the viscosity, which is consistent with analytical predictions using Green’s function and experimental measurements in dense cellular systems (Giomi, 2015; Meacock et al., 2021; Saw et al., 2017) (Fig. 7.4a). Upon decreasing the viscosity the flow field around the defects keeps its shape, however, the size of the flow vortices around the defect is reduced and the flow strength at the defect core is enhanced (Fig. 7.4b). This means that at lower viscosities the speed of the propulsion of $+1/2$ defects increases, while their higher density leads to a more effective screening of their associated flows due

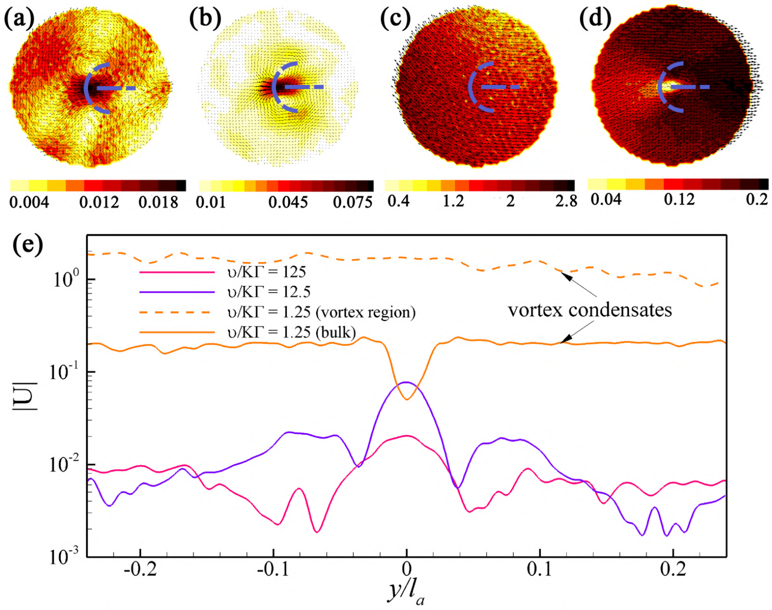

Figure 7.4 **Viscosity impact on the flow field of topological defects.** Velocity field and contours of velocity magnitude for the average defect flow at (a) $\nu/K\Gamma = 125$ and (b) $\nu/K\Gamma = 12.5$. (c) and (d) show the average defect flow for the vortex-condensate state at $\nu/K\Gamma = 1.25$, calculated separately for (c) defects inside giant vortices and (d) the bulk of the system excluding the giant vortices. In (a)-(d) blue dashed line schematically show the alignment of the $+1/2$ defect with respect to the averaged flows. (e) Velocity profile around defects showing the magnitude of velocity along a vertical axis passing through the center of defects in (a), (b), (c) and (d).

to the stronger interactions with other defects.

Further decrease in viscosity and the emergence of the vortex-condensate, however, completely alters flow features of the $+1/2$ topological defects: within the giant vortices the defects move along their comet head and rotate around the vortex center as characterized by the tilted averaged velocity field (Fig. 7.4c). Remarkably, within the bulk of the condensate phase, the magnitude of the velocity also drops at the defect core and the average flow of the $+1/2$ defects points along the defect tail indicating that the defects align anti-parallel to the flow direction (Fig. 7.4d). This is because within the bulk, the strong shear flow between the two giant vortices aligns $+1/2$ defects anti-parallel to the strong flow and the defects are advected by the strong flow between the two vortices. As such within the condensate phase, the propulsive nature of the $+1/2$ defects is suppressed by the flow field established through vortex-condensate and defects have negligible impact on the flow field, contrary to the active turbulence state where the propulsive nature of the $+1/2$ is an indispensable determinant of the flow structure within the system (Giomi, 2015; Thampi, Doostmohammadi, Golestanian & Yeomans, 2015). The flow characteristics around defects can be further quantified by calculating the decay of the velocity magnitude away from the defect core, which clearly demonstrates the alterations to the flow scale with decreasing viscosity and with the emergence of the vortex-condensate phase (Fig. 7.4e).

It is noteworthy that the emergence of the vortex-condensate depends not only on viscosity, but also on the activity of the particles. To show this, Fig. 7.5 illustrates the stability diagram of the vortex-condensate formation in the viscosity-activity phase space. As evident from the figure, even at moderately high viscosities, vortex-condensate can form for strong enough activities. Only at significantly high viscosity, where the inertial effects are completely suppressed by the viscous dissipation and the convective inter-scale transfer is insignificant, no vortex-condensate is observed. Moreover, the emergence of the vortex-condensate is only observed for extensile (pusher) particles and even for high values of contractile activity and strong inertia the active turbulence is established and we could not find any condensate state. We conjecture that the observed difference between the extensile and contractile systems can be associated with the difference in the response of the collection of extensile and contractile active particles to the flow gradients: extensile particles collectively align to the shear flows established by their self-generated active stresses, which leads to the local ordering of extensile active systems, as shown previously (Santhosh, Nejad, Doostmohammadi, Yeomans & Thampi, 2020b; Thampi et al., 2015). On the other hand, contractile activity destroys such an ordering. This effect is best evident from previous studies on active nematics that show combined effects of activity and flow alignment lead to renormalization of the molecular field, as shown in the context of intrinsic free energy of active nematics (Thampi et al., 2015): for non-zero and positive values of the flow-aligning parameter λ, contractile $\zeta < 0$ and extensile activities $\zeta > 0$ have the opposite impact on the effective free energy of the system. As such, contractile activity increases the energetic cost of the breakdown of nematic order, while extensile activity enhances it.

To test this conjecture directly in our simulations, we explored cases with contractile activity ($\zeta < 0$) and negative values of the flow-aligning parameter ($\lambda < 0$). The results confirm that it is possible to obtain a vortex-condensate state for contractile activities when the flow-aligning parameter is negative and emphasize that the sign of the product $\zeta\lambda$ is the determining factor (Fig. 7.6). Furthermore, for $\lambda = 0$ there was no vortex-condensate state for neither contractile nor extensile activity.

Having established the impact of viscosity reduction on the flow and director field of active nematics, we next turn to the energetic features of the flow. This is best represented by the kinetic energy spectrum $E_k = \frac{1}{2}\langle \hat{u}_i(k)\hat{u}_i(k)\rangle$, which measures the kinetic energy associated with differing scales characterized by the wavenumber k.

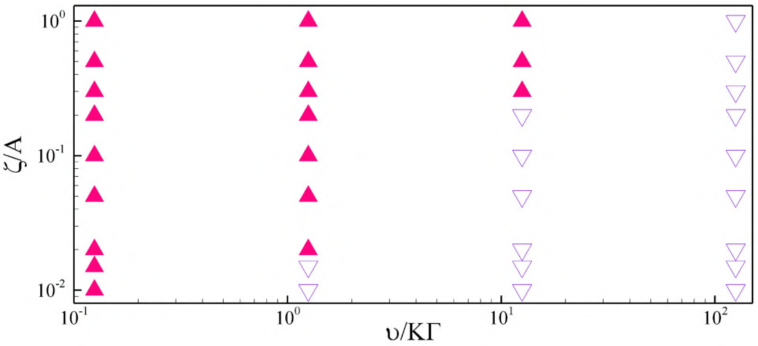

Figure 7.5 **Stability diagram for the vortex-condensate formation in active nematics.** Effect of viscosity and activity on the vortex condensation formation are shown. Filled points represent the vortex condense state.

A numerical study of the simplified active nematics, which neglects order variation and thus topological defects, suggested a universal scaling of the kinetic energy, $E_k \sim k^{-1}$ at small wavenumbers (Alert, Joanny & Casademunt, 2020b). While such a k^{-1} scaling is recently observed in a numerical study of active *polar* fluid in certain parameter regimes (Chatterjee et al., 2021), numerical simulations of the full active nematics did not find such universal behavior (Amiri, Mueller & Doostmohammadi, 2021; Krajnik, Kos & Ravnik, 2020; Urzay et al., 2017). Most recently, a combined theoretical and experimental study showed different scaling regimes depending on the external or internal dissipation mechanisms for microtubule-kinesin motor mixtures at oil-water interface, which represent a realization of two-dimensional active nematic material (Martínez-Prat, Alert, Meng, Ignés-Mullol, Joanny, Casademunt, Golestanian & Sagués, 2021).

Let us first consider the vortex-condensate case that appears at low viscosities, corresponding to high Reynolds numbers. In agreement with classical 2D turbulence within the inertial range the power spectrum shows Kolmogorov scaling with a power-law decay with the exponent $-5/3$ (Boffetta & Ecke, 2012) (Fig. 7.7; *orange line*). This indicates that at low viscosities, the vortex-condensate generated by local energy injection in active nematics shares similar scaling behavior as driven inertial turbulence. Incremental reduction of inertial effects by successively increasing the viscosity, however, completely alters the scaling behavior of the active nematic turbulence. At small wavenumbers, corresponding to large scales, the kinetic energy shows again a power-law behavior with a non-universal viscosity-dependent exponent (Fig. 7.7; *purple and magenta lines*). The transfer of energy to smaller scales (larger wavenumbers), however, does not follow a universal power-law decay, as has been suggested by analytical and numerical studies of active nematics that neglect topological defects (Alert et al., 2020b; Giomi, 2015). Instead, representing the energy spectrum on a semi-log plot reveals a viscosity-dependent exponential

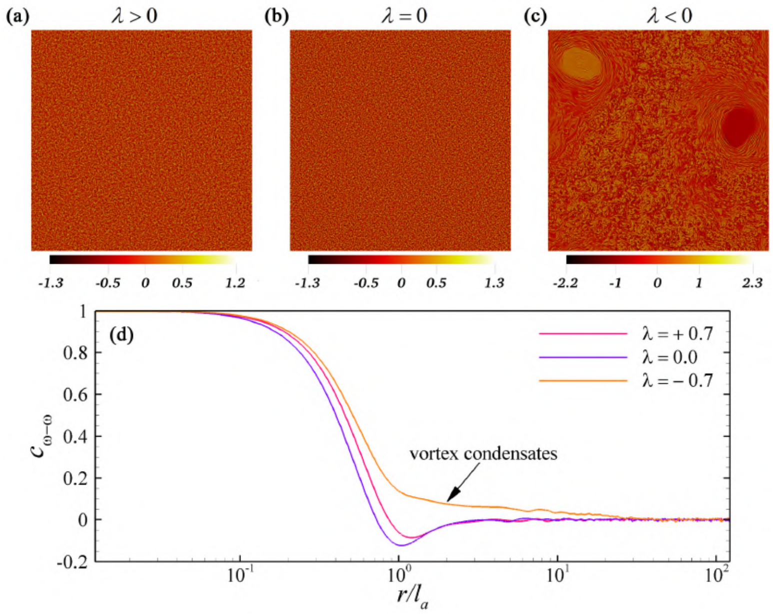

Figure 7.6 **Active turbulence and vortex-condensates for contractile activity ($\zeta/A = -0.03$) at $\nu/K\Gamma = 1.25$.** Snapshots of the flow vortices for positive, zero, and negative tumbling parameter: vorticity contours for (a) $\lambda = +0.7$, (b) $\lambda = 0$, and (c) $\lambda = -0.7$. (d) Effect of tumbling parameter on vorticity-vorticity correlations.

decay of the energy with wavenumber, that is due to the dominating effect of viscous dissipation with reducing the inertia. This is important, because existence of universal scaling laws for active turbulence, that are independent of activity and viscosity, have been suggested based on power-law decay of energy spectrum with the wavenumber as $\sim k^{-4}$ (Alert et al., 2020b). The large-scale numerical simulations conducted here that account for topological defects in the system do not show any indication of such universal scaling laws and rather suggest a dissipation dominant exponential regime at low Reynolds numbers, calling for further studies in this direction.

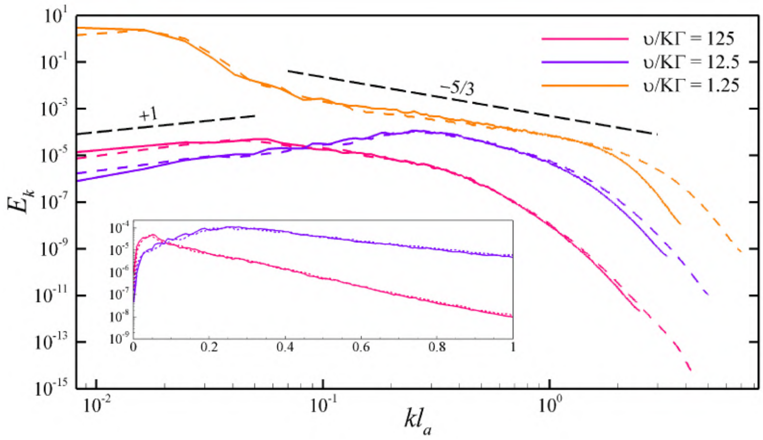

Figure 7.7 **Kinetic-energy spectra.** The wavenumber is non-dimensionalized by the active length scale $l_a = \sqrt{K/\zeta}$. Solid- and dashed- lines, respectively represent 1024×1024 and 2048×2048 grid resolutions. While within the vortex-condensate state a power-law decay is observed, lower viscosities manifest exponential decay with the wavenumber (semi-log plots in the inset).

8. Vibration induced by active nematics

8.1 Introduction

Due to the continuous energy injection of the constituent active particles, chaotic nature in the active fluid emerges, which is known as active turbulence (Alert et al., 2022; Bratanov et al., 2015; Doostmohammadi et al., 2017; Urzay et al., 2017; Wensink et al., 2012). In such a chaotic flow, kinetic energy of micro-scale elements is transferred to a passive body immersed in the active fluid such that the body experiences a mechanical force on its boundaries. If the exerted energy is sufficiently high, the body could undergoes deformation (Paoluzzi, Di Leonardo, Marchetti & Angelani, 2016), translation (Wu, Lv, Zhao & Ai, 2018), rotation (Angelani, Di Leonardo & Ruocco, 2009), or their combination.

Considering the induced motion of passive immersed bodies, a question may arise such that if the active flow is also capable of generating vibrational motion due to its chaotic and turbulent nature. As such, it should be possible to induce a constructive oscillatory motion on a flexible body possibly made of a piezoelectric material that can be used as a sensor to extract the physical properties of active fluid.

Generally, the behavior of active nematics is affected mainly by fluid activity and elastic constant. In our recent unpublished work, we also showed that viscosity has a significant role by introducing the inertia effect to the active nematics system. The measurement of these parameters is experimentally challenging (Frishman & Keren, 2021), and often, the secondary properties are used to extract these main parame-

---

This chapter is a slightly modified version of "Vibration induced by active nematics" submitted to "Journal of Fluid Mechanics" by "R. Saghatchi, and M. Yildiz"

Table 8.1 The discretization schemes that are used in this study (Moukalled et al., 2016).

Term	Scheme
Time integration	Euler
$\boldsymbol{\nabla}()$	Least squares
$\boldsymbol{\nabla}.()$ (advection term)	Gauss linear (upwind)
$\boldsymbol{\nabla}^2()$	Gauss linear

ters. Currently, the most common method to assess the activity is to measure the ATP, the motor cluster, microtubules, or polyethylene-glycol concentrations (Doostmohammadi et al., 2018; Henkin, DeCamp, Chen, Sanchez & Dogic, 2014), among others. Researchers have been working on numerical procedures such as machine learning algorithm (Colen, Han, Zhang, Redford, Lemma, Morgan, Ruijgrok, Adkins, Bryant, Dogic, Gardel, de Pablo & Vitelli, 2021) to find an alternative approach to measure the physical properties directly.

Considering the aforementioned issues, we placed a cantilever beam in active nematics and numerically analyzed the induced vibration. We used a continuum model for the active nematics and combined it with a fluid-structure interaction (FSI) solver to calculate the imposed force on the beam, and consequently, analyze its motion. We investigated the effects of vorticity and velocity field on the beam oscillation. Then, we demonstrated the effect of three critical parameters, including fluid activity, viscosity, and its elastic constant on the beam peak frequency and proposed a mathematical relationship that makes direct measurement feasible for the future practical utilization.

8.2 Problem statement

In this study, a 2D continuum approach is implemented for modeling the nematic phase. In addition to the fluid phase, we are going to solve the governing equations for the solid part. The model for the solid phase is introduced in Appendix B. The discretization schemes for each separate term in the governing equations are summarized in table 8.1. Pressure and velocity coupling throughout the fluid domain is carried out by PISO algorithm (Versteeg & Malalasekera, 2007). Solution domain consists of a square region with a cantilever beam located at the middle point of

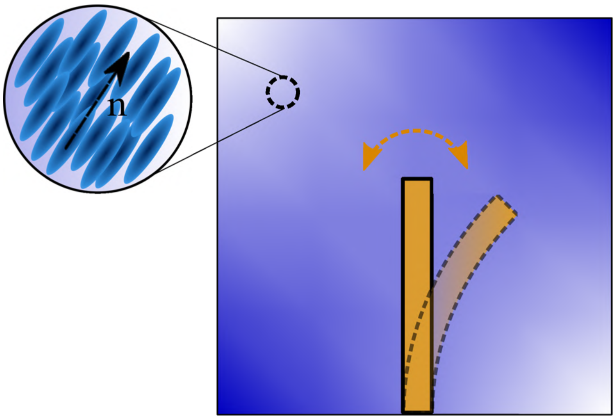

Figure 8.1 **Schematic representation of problem.** Physical domain includes a cantilever beam inside active nematics. Nematic particles and the orientation vector are represented in the inset.

Table 8.2 Values used in the numerical simulations , unless stated otherwise..

Fluid		Solid	
Parameter	Value	Parameter	Value
ρ	$1(Ns^2m^{-4})$	ρ_s	$1(Ns^2m^{-4})$
λ	0.7	E	$0.1 \times 10^6(Nm^{-2})$
Γ	$0.0136(m^2N^{-1}s^{-1})$	ν	0.3
K	$0.003(N)$	l/w	0.05
A	$1(Nm^{-2})$		
ζ	$0.03(Nm^{-2})$		

the bottom boundary (see Fig. 8.1). No-slip boundary condition is applied on all boundaries including the fluid-solid interface, while the zero-gradient condition is used for $\mathbf{Q}$. The structured Cartesian grid with 256×256 is used to discretize the domain and the CFL condition is enforced to control the solution time-step size. Initially, zero velocity field is applied with uniform nematic orientation $\mathbf{n}$ in the horizontal direction with a slight perturbation, and the results are evaluated at the time step at which steady state is statistically attained.

The main parameters used in this study are tabulated in table 8.2. In this table, E and ν, respectively, represent the elastic modulus and Poisson's ratio, and l/w is the length- to- thickness ratio of the beam. Based on the values in the table 8.2, we define natural frequency of transverse vibration of a cantilever beam as $\omega = (\beta l)^2\sqrt{\frac{EI}{\rho_s A l^4}}$, where $\beta l = 1.875104$, I is the area moment of inertia, A represents the cross section area, and l is the beam length (Rao, 2011). Consequently, dimensionless time and frequency become $t\omega$ and $(t\omega)^{-1}$, respectively. Since the activity and viscosity are the important parameters in our study, we define dimensionless activity and viscosity as ζ/A and $\mu\Gamma$, respectively.

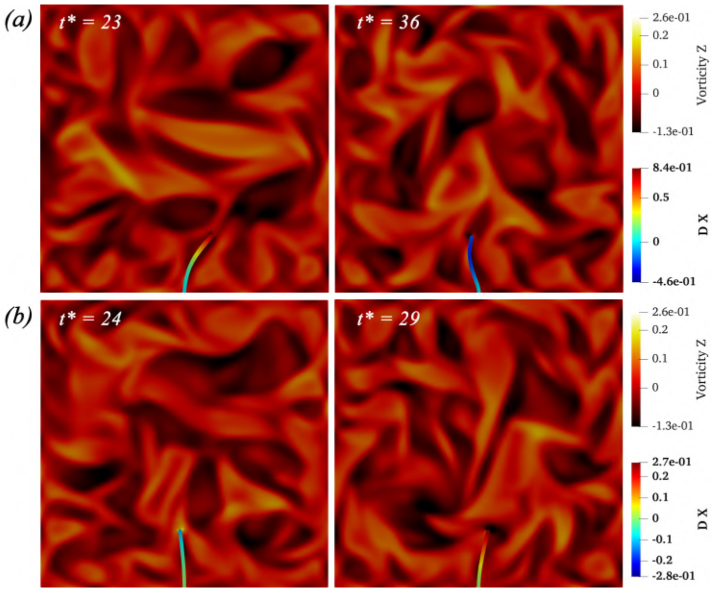

Figure 8.2 **Vorticity and the beam displacement contours at the different times ($t^* \approx t\omega \times 10^{-2}$).** Results are shown for a beam with high elastic modulus (a), and low elastic modulus (b), correspond with $E = 0.01KPa$ and $E = 1.0KPa$, respectively.

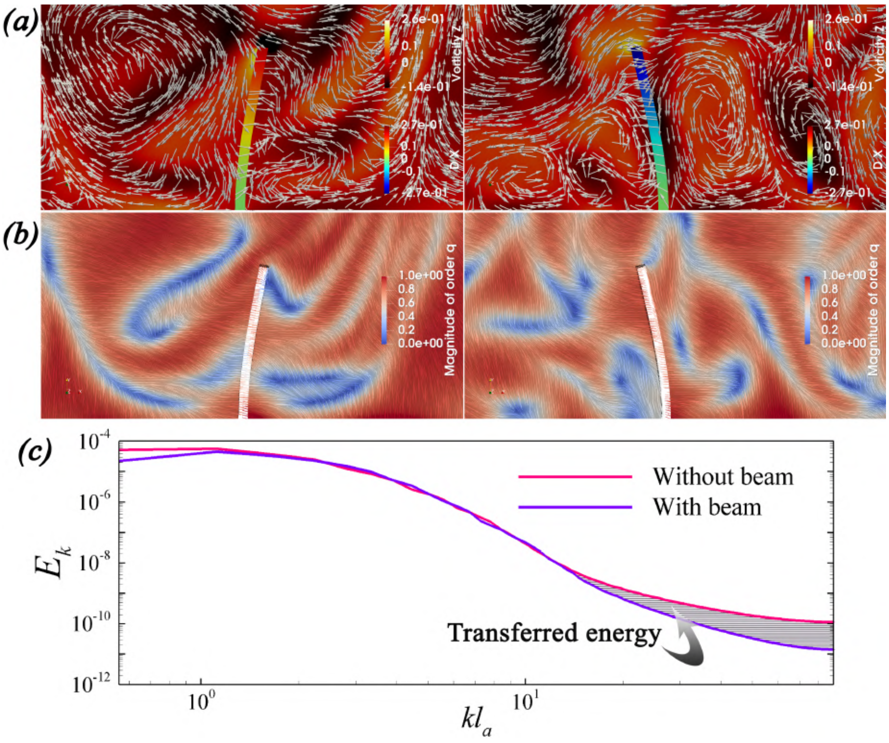

Figure 8.3 **Flow and energy of the active nematics in the domain.** Flow and nematics characteristics in the domain close to the beam at $t\omega \approx 37 \times 10^{-2}$ (left column) and $t\omega \approx 81 \times 10^{-2}$ (right column). (a) vorticity, beam displacement, and the velocity vectors. (b) nematics director and their order of magnitude. (c) Effect of beam presence on the kinetic-energy spectrum. The beam absorbs the kinetic energy of the low-scale vortices and consumes it for vibrational motion.

8.3 Results

We begin with the qualitative representation of the beam motion and flow field in the physical domain. We take $\zeta = 0.01$ and $K = 0.05$, and the simulations are performed for the beams with two different values of elastic modulus, i.e., $E = 0.01KPa$ and $E = 1.0KPa$ (Fig. 8.2). Beam with lower elastic modulus imitated the soft material such as biological tissue, which can easily bend under the effect of active stress. The beam bending is related to the flow dynamics, as shown in Fig. 8.3-a. In this sub-figure, velocity vectors are shown in vicinity of the beam. Clearly, magnitude of beam deformation and its orientation are controlled by the dominant direction of velocity vectors. If two vortices appear on different sides of the beam, the strongest one determines the bending direction as shown in Fig. 8.3-a. To further elaborate, when the strongest vortex (or vortices) travels inside the domain and moves towards the beam, it exerts forces on the beam and deforms it in the same direction. From energy perspective, fluid elements inside these vortices posses a high amount of kinetic energy. If these kinetic energies that are transferred to the beam elements are high enough to surpass the beam's elastic potential energy and inertial force, the beam deforms and deflects. Thus, as the exerted force is more concentrated towards the beam tip, beam deflection is expected to be higher. Vortices are being moved in the domain due to the interactions of defects and the change in the director field (Fig. 8.3-b). Furthermore, continuous energy injection creates new vortices, their size are being changed continuously by the energy cascading and they are finally dissipated by the viscous force. As a consequence of these periodic processes, a random excitation is imposed on the beam, leading to random vibration.

The kinetic energy spectra can best represent quantitative features of the energy transfer to the beam, which characterizes the associated kinetic energy $E_k = \frac{1}{2}\langle \hat{u}_i(k)\hat{u}_i(k)\rangle$ at different scales. Figure 8.3-c illustrates the kinetic energy spectrum for the wavenumber k, considering either the presence or the absence of the beam. Characteristic length scale $l_a = \sqrt{K/\zeta}$ is used to normalize the wave number. As inferred from this figure, energy at higher ranges of wavenumbers is considerably lower when the beam is placed in the system. It shows that the beam takes fluid energy mainly at high wavenumbers corresponding to the small-scale vortices and consumes this energy for its oscillatory motion.

As mentioned above, fluid physical properties such as activity and viscosity could affect the beam vibration. We first investigate the beam vibration under the different values of activity parameters, ζ to verify this claim. The value of $E = 0.1MPa$

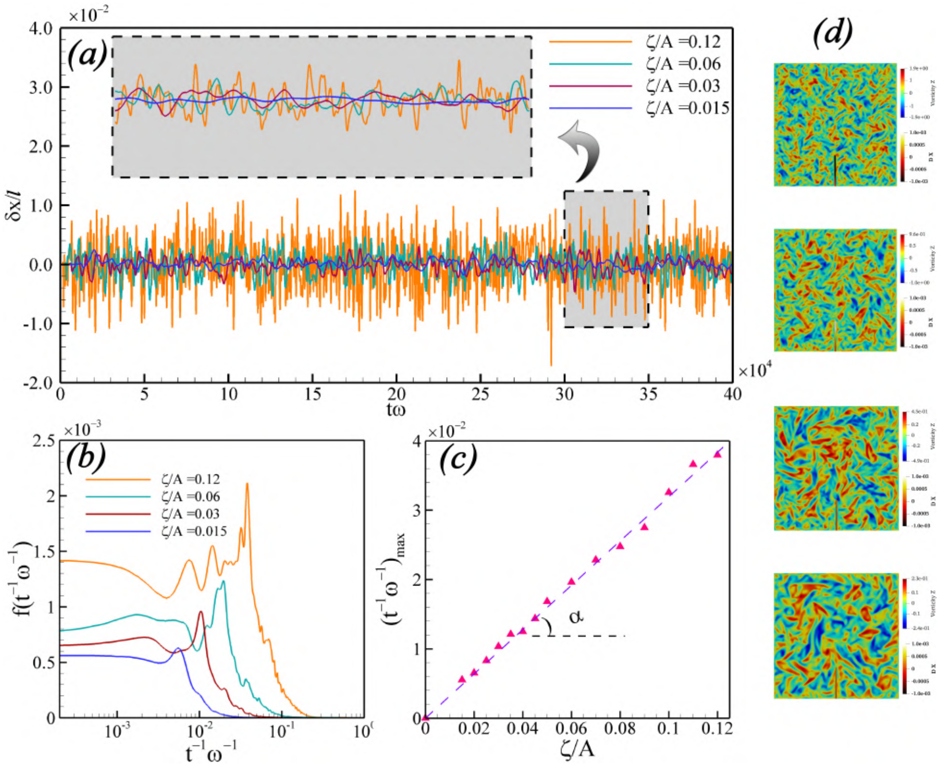

Figure 8.4 **Results for a cantilever beam within the fluid with different activities:** (a) Time history of the beam's normalized deflection (the inset magnifies the small spam of the vibration history); (b) Fourier Spectrum; (c) frequency versus activity (linear relation is seen and demonstrated with a dashed line representing the regression analysis). (d) represents the vorticity and beam deflection contours for $\zeta/A = 0.12$, 0.06, 0.03, and 0.015 from top to bottom row.

is taken for the beam elastic modulus to represent an actual piezoelectric transducer (Elvin, Elvin & Senderos, 2018). Beam tip displacement is monitored during the simulation and plotted as a function of dimensionless time, as shown in Fig. 8.4-a. This figure also presents the impact of activity on the vibrational motion of the beam. It is observed that a rise in the activity parameter increases the displacement amplitude. Physically, enhancing the activity is equivalent to injecting a higher amount of energy into the fluid elements. Consequently, when transferred to the beam, this energy could deflect the beam more and lead to a higher amount of displacement.

To scrutinize the activity influence on the vibration frequency, we performed the FFT[1] analysis to convert the displacement from a time domain to the frequency domain (Moin, 2010). Due to the non-deterministic nature of the excitation, multiple frequency peaks exist in the FFT curve. Since the maximum frequency peak is of

---

[1] Fast Fourier Transform

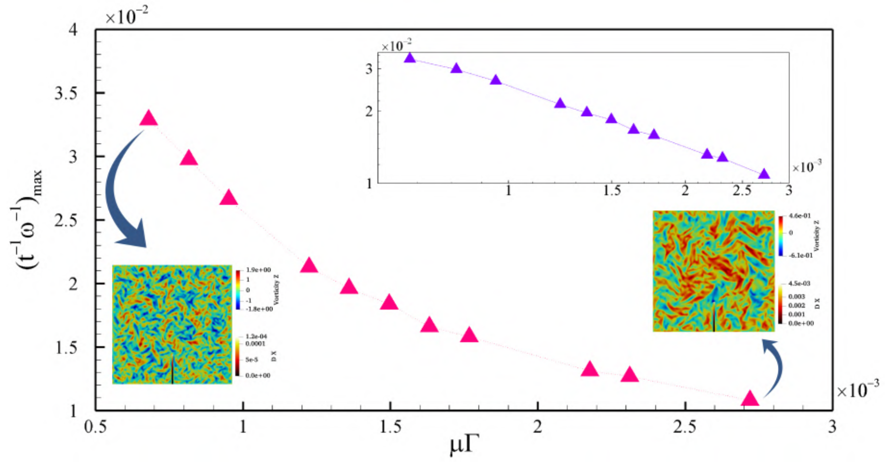

Figure 8.5 **Effect of viscosity on the beam peak frequency.** Inset shows the same data in the log-log scale, indicating the reciprocal relationship between viscosity and the peak frequency. The effect of viscosity on the size of vortices is also shown for two different viscosity values.

interest, an AMF[2] is used to smooth out the FFT curve and remove the unnecessary noises (Smith & others, 1997), and the resultant curves are given in Fig. 8.4-b. As shown in this figure, the activity parameter alters the maximum or peak frequency such that the peak frequency shifts towards a higher value with the increase in activity. To obtain a possible correlation between the peak frequency and the activity parameter, we performed the simulation for various values of activity parameters and presented the results in Fig. 8.4-c. Interestingly, a linear correlation is observed for the peak frequency- activity parameter. The dashed line in this figure is the linear regression resulting from these correlation, showing an apparent linear relationship between peak frequency and activity. Qualitatively, recalling that a higher value of activity parameter is equivalent to higher energy injection into active nematic system. This increases the energy of small-scale vortices thereby hindering their dissipation by viscous forces, and also breaks large vortices into smaller ones with reduced energies, which is referred to as energy cascading mechanism, (Fig. 8.4-d). Essentially, the higher the activity or energy injection, the smaller the size of vortices. Vortices with smaller sizes can move quickly and with higher frequency in the domain. These small yet strong vortices continuously collide with the beam and result in high beam vibration frequency. Experimentally, the slope of the peak frequency- activity curve (α in Fig. 8.4-c) is obtainable through calibrating the piezoelectric transducer whereby it becomes possible to measure the fluid activity parameter.

It is also worthwhile to check the dependency of the peak frequency on the bulk

---

[2] Average Moving Filter

viscosity μ of the active fluid as well. Figure 8.5 demonstrates the variation of peak frequency as a function of dimensionless viscosity. As shown in this figure, the viscosity has an inverse and approximately reciprocal relationships with the peak frequency. A log-log diagram is also presented as an inset of this figure to illustrate this behavior better meaning that the peak frequency can be expressed by $\approx f(1/\mu)$ function. This behaviour can physically be explained considering the energy cascading mechanism. Namely, the larger the viscosity is, the higher frictional force, which can dissipate the energy of small-scale vortices. Remembering the role of small-scale vortices in the beam oscillatory movement, an increase in the viscosity reduces peak frequency. Meanwhile, active nematics with lower viscosity fail to provide a substantial frictional mechanism to dissipate the energy of small-scales vortices, resulting in an increase in the imposed energy to the beam.

It is worth noting that the numerical investigation is also performed to examine the impact of the elastic constant K of active fluid on the beam frequency; however, no significant effect is observed. Recalling the characteristic length scale in active nematics, i.e. $l_a = \sqrt{K/\zeta}$, one may expect that the variation in elastic constant K should change the length scale and vortices sizes. Referring to discussion provided to understand the correlation between the activity/viscosity and peak frequency, this variation should also lead to changes in the peak frequency. However, in the case of elastic constant, it should be noted that K is also responsible for penalizing gradients in the nematic orientation, hence for the free energy ($\mathcal{F}$). Consequently, the balance between the $\mathcal{F}$ and vortex size determines the resultant frequency, which undergoes insignificant change with the variation in K, as our results show. In other words, the elastic constant does not participate in either injection or dissipation of the energy to/from the small scale vortices, where both of them are responsible for determination of the system's time scale, hence the beam frequency.

9. Conclusion

The work presented in this thesis spans several topics in complex soft matter physics and stages of developing and using computational tools. Two different numerical methods, i.e., smoothed particle hydrodynamics and finite volume are used to simulate the emulsions and active nematics flow. Section 9.1 summarizes the main findings. Section 9.2 provides an outlook for continuing the research presented in this thesis.

9.1 Summary

Firstly, in chapter 4, the EHD behavior of a droplet is studied in a highly confined domain. Six different fluid systems are selected corresponding to the different electrical properties. It was shown that in the unbounded domain, ratios of the electrical properties are the main factors in determining the droplet deformation shape and values. By increasing the confinement ratios, the droplet deformation value was changed and in some cases, switched from oblate/prolate shape to prolate/oblate elongation. The dependency of the droplet deformation on the electric force components, including polarization and Coulomb forces, is discussed thoroughly. It was shown that these forces are the main reason for the droplet deformation and their strengths are highly dependent on the confinement ratio. The effect of the pressure force is also considered, and it was shown that its contribution becomes significant at high confinement ratios where it acts in the opposite direction with the electric force, decreasing the deformation value at high confinement ratios. To simplify the analysis, the force ratio was defined and used to show the contribution of each effective force on the droplet deformation. These force ratios are then sketched as a function of confinement ratio for some systems to better understand their effect and simplify their comparison.

Additionally, in chapter 5 the behavior of a double emulsion is studied under the combined effect of the electric field and shear flow. Six different systems are chosen based on electrical properties. Deformation and orientation angles of the core and the shell droplets are calculated under pure shear, pure EHD, and combined EHD-shear flow. Flow streamline patterns are utilized to discuss the results. It is shown that the flow vortex direction depends on the conductivity and permittivity ratios. Electric force components are calculated on the interfaces and their effects on the double emulsion dynamics are discussed comprehensively. In addition to the EHD forces, hydrodynamics forces are also computed within the the entire flow domain. It is pointed out that in the double emulsion with a viscosity ratio of unity, pressure has a significant contribution to hydrodynamic forces. The effects of capillary, electrical capillary numbers, and core to shell radius ratio on the double emulsion dynamics are investigated as well. It is indicated that the deformation of core/shell droplet increases/decreases with an increase in radius ratio. Double emulsion exhibits relatively complex behavior in response to the variation of capillary and electrical capillary numbers which has been explained considering the interaction of hydrodynamics and EHD forces. Finally, the breakup phenomenon is elaborated in double emulsions and the necessary condition for the breakup is explained. Different breakup patterns are identified in the double emulsion for the specific electrical properties.

Secondly, in chapter 6 the weakly compressible smoothed particle hydrodynamics method is used to simulate the active nematic fluid. The simulations are performed with the presented GPU-based algorithm on the CUDA C++ programming language using an object-oriented approach. Ghost periodic boundary condition is introduced and applied to all boundaries to imposed the periodic boundary condition. Since the nematic fluid is composed of nematic particles, collective movement of SPH particles is perfectly mimicked the movement of the nematic particles. Fluid flow characteristics, including vortex structures and streamlines, are exhibited, and the turbulent-like behavior of the nematic fluid is presented qualitatively. To scrutinize the turbulent characteristics, the relation between the kinetic energy and wavenumber is evaluated. Vorticity- vorticity correlation is calculated, and the characteristic length scale is defined based on it. Nematic orders and director is calculated and used to detect the topological defects. Positive half and negative half defects are discussed in detail. Results are presented for the effects of two important parameters, activity and elastic constant. The effect of activity on the velocity root mean square is evaluated, and it is seen that by increasing the absolute value of the activity, the velocity root mean square increases as well, while its effect is strong for negative activities. To exploit the SPH capabilities, pathlines and mixing of nematic particles are described qualitatively. It was shown that the length of pathlines is proportional to the activity. The effect of the elastic constant is also calculated, and it is shown that higher values of elastic constant exhibit larger vortex length scales and smaller defect numbers, and inferior mixing. It was shown that the activity and elastic constant behave oppositely in the creation of chaotic flow, which initiates from the energy minimization.

In chapter 7 we provided finely-resolved simulations of the active nematohydrodynamic equations in the presence of progressively increasing inertial effects. By incrementally reducing the fluid viscosity, we quantified the variations of emergent system properties, including velocity, orientational order, and density of topological defects. At sufficiently small values of viscosity the system manifests reverse energy cascade and formation of vortex condensate, as well as the Kolmogorov scaling in the decay of the kinetic energy, similar to classical driven turbulence, albeit at significantly lower Reynolds numbers, $Re_\mathrm{I} \sim O(10^2)$ (defined based on the integral scale), and due to the local energy injection by activity, rather than any external forcing. We provided a phase diagram of the vortex-condensate formation in the activity-viscosity phase space, emphasizing the synergistic impacts of active stresses and fluid inertia. Our results further showed that vortex-condensate formation is accompanied by significant modifications of the orientational features of the system, leading to order condensation and a drop in the defect density. Analyzing the defect within the condensate state, further demonstrated a significant deviation in the flow field around the topological defects. Importantly, we showed that the condensate-formation in inertial active nematics depends strongly on the flow-aligning behavior of the active particles and the extensile or contractile stresses that they generate. Our results further revealed that in the non-condensate regime, the averaged velocity of the entire system shows logarithmic decay with the fluid viscosity. Additionally, within this regime, we showed that the kinetic energy spectrum lacks any universal scaling. Indeed, the results, even at a highly viscous regime, indicated an exponential - rather than algebraic - decay of the energy spectrum with the wavenumber. The results presented in this study demonstrate the important interplay between the active stress generation and fluid inertia in active fluids.

Finally, in chapter 8, we presented a numerical method to solve the continuum model of active nematics which is combined with an FSI solver to simulate the vibration induced by active turbulence. For this purpose, we placed a cantilever beam inside the active nematics and investigated the effect of important active fluid parameters such as activity, viscosity and elastic constant on the beam oscillatory motion. We provided qualitative data, including vorticity field and nematic ordering to investigate the beam dynamics. Our results showed that vortex formation that initiates from the symmetry breaking in the nematic ordering, plays a dominant role in beam deflection. We also indicated that the size, strength and position of vortices determine the direction and magnitude of beam deflection. Using the kinetic energy spectrum, we demonstrated that the small-scale vortices play the primary role in the beam oscillatory motion by transferring the kinetic energy between active fluid and beam. We quantified the beam oscillation using FFT analysis on the beam tip displacement data and calculate the beam peak frequency. Our results showed that the activity and beam peak frequency are linearly correlated. The physical phenomena behind this correlation is explained through considering the nematic activity (which influences the energy injection into the system) and its role on reducing the size of vortices. Our results further revealed the reciprocal relationship between viscosity and beam peak frequency, which steams from the fact that viscosity dissipates the energy of small-scale vortices. Finally, we analyzed the impact of the elastic constant of active nematics on the beam peak frequency and show that its effect is insignificant. The results presented in this chapter propose a potential novel method to measure the critical parameters of active nematics that play a significant role in determining its flow behavior using the beam peak frequency concept. This method can be an alternative to the current challenging measurement techniques that determine the activity, for example, by measuring secondary parameters such as ATP, the motor cluster, microtubules, or polyethylene-glycol concentration (Doostmohammadi et al., 2018; Henkin et al., 2014).

9.2 Outlook

This thesis presented emulsion dynamics under the effects of electric field and shear flow, active nematics simulation, the impact of inertial force on the nematic flow, and structure interaction with the active nematics. While several physics were explored, there are still many interesting open research subjects. The discussion can be from either computational aspect and application to physics.

Computational aspect
Here, we used CUDA parallelization platform for the SPH algorithm. As shown in chapter 6, parallelization has led to a significant speed-up. However, the current code can be much faster by applying further optimizations regarding the solution and parallelization algorithms. One suggestion could be the development of an efficient linear system solver in CUDA. The standard OpenFOAM uses OpenMP

for the parallelization. It would be much more effective if a GPU solver is used. Moreover, it would be intriguing to extend all simulations into 3D to be much more realistic.

Applications

As discussed in chapter 2, throughout this thesis, all fluids are supposed to be Newtonian ones. It would be interesting to extend the results to non-Newtonian fluids and see the effects specifically for the emulsion dynamics. In chapters 4 and 5, we considered the same viscosity and density for all liquids and focused mainly on the electrical properties instead. Thus it would be beneficial to take different hydrodynamical properties for droplets and ambient liquids. As mentioned in 5, core and medium fluids are identical are identical in the double emulsion following the studies done by Abbasi et al. (2019); Opalski et al. (2020); Song & Shum (2012); Tsukada et al. (1997). Extending the simulation to three-phase is useful by considering the different properties of the core and medium fluids.

In chapter 6, we developed the SPH solver for the active nematics and showed some potential capabilities of SPH such as mixing. Using SPH, complex and deformable domains, mixtures, and multiphase interfaces can also be modeled with relative ease, unlike the Eulerian approach. This attribute of the SPH method is particularly appealing for modeling mixing behavior in active nematics as well as nematic flow with material interfaces and interface motion (e.g., bacterial growth), which can be the subject of the future direction of the current research. As shown in chapter 7, we investigate the effect of inertia on active nematics. Fluid inertia is expected to play a role in the collective organization of larger swimming organisms (Klotsa, 2019) such as marine zooplanktons, Copepods, and brine shrimp (*Artemia salina*) that are commonly encountered in environmental fluids (Houghton et al., 2018; Katija & Dabiri, 2009; van Duren & Videler, 2003). It would be interesting to scrutinize these problems and see the effect of activity on such physics. Finally, the FSI model in the active fluid can have alternative potential applications such as energy harvesting and biological applications, which might be the subject of future studies.

Appendices

Appendix A

Derivation of Beris-Edwards model

The advection part of the nematodynamic equation for $\mathbf{Q}$ can be derived by taking the material time derivative of the director field $\hat{n}$, which can be shown to be of the form, $\mathrm{D}\hat{n}/\mathrm{D}t = \hat{n}\cdot\mathbf{\Omega} = \hat{n}\cdot(\boldsymbol{\nabla}\mathbf{u}-\mathbf{E})$, where $\mathbf{\Omega} = \frac{1}{2}\left[(\boldsymbol{\nabla}\vec{u})^{\dagger} - \boldsymbol{\nabla}\vec{u}\right]$ and $\mathbf{E} = \frac{1}{2}\left[\boldsymbol{\nabla}\vec{u} + (\boldsymbol{\nabla}\vec{u})^{\dagger}\right]$ are the vorticity and the rate of strain tensors, respectively. The dag superscript ($\dagger$), ($\cdot$) and $\boldsymbol{\nabla}$ respectively represent the transpose, inner dot product and the Nabla operators. Additionally, $\mathrm{D}/\mathrm{D}t$ represents the material time derivative which can be written as $\mathrm{D}/\mathrm{D}t = \partial/\partial t + \mathbf{u}\cdot\boldsymbol{\nabla}$. Recalling the definition of $\mathbf{Q} = \frac{d}{d-1}q\left(\hat{n}\hat{n} - \frac{\mathbf{I}}{d}\right)$ or $\mathbf{Q} = \frac{1}{\lambda}\left(\hat{n}\hat{n} - \frac{\mathbf{I}}{d}\right)$ with $\lambda = \frac{q(d-1)}{d}$ representing the scalar part, one can rearrange $\hat{n}$ based on $\mathbf{Q}$ as $\hat{n}\hat{n} = \lambda\mathbf{Q} + \frac{\mathbf{I}}{d}$, recalling the time derivative of $\hat{n}$ in index notation, $\dot{n_m} = \Omega_{ml}n_l$, and $\dot{n_m n_s} = \Omega_{ml}n_l n_s + \Omega_{sl}n_m n_l$. Using $n_l n_s = \lambda Q_{ls} + \frac{\delta_{ls}}{d}$, then it is possible to write the time derivative of $\mathbf{Q}$ as follows:

$$\text{(1)} \qquad \lambda \mathrm{D}Q_{ms}/\mathrm{D}t = \Omega_{ml}(\lambda Q_{ls} + \frac{\delta_{ls}}{d}) + \Omega_{sl}(\lambda Q_{ml} + \frac{\delta_{ml}}{d}).$$

Every second order tensor (T_{ij}) can be decomposed into symmetric and skew parts by $T_{ij} = \frac{1}{2}\left[(\boldsymbol{\nabla}T_{ij})^{\dagger} + \boldsymbol{\nabla}T_{ij}\right] + \left[(\boldsymbol{\nabla}T_{ij})^{\dagger} - \boldsymbol{\nabla}T_{ij}\right]$. If T_{ij} is substituted with velocity, then the symmetric part and skew part would be the rate of strain and vorticity tensors, respectively. Then (1) becomes:

$$\text{(2)} \qquad \lambda \mathrm{D}Q_{ms}/\mathrm{D}t = (v_{m,l} - E_{ml})(\lambda Q_{ls} + \frac{\delta_{ls}}{d}) + (v_{s,l} - E_{sl})(\lambda Q_{ml} + \frac{\delta_{ml}}{d}),$$

where $v_{i,j}$ is the index notation representation of velocity gradient. By doing mathematical manipulations, material time derivative of $\mathbf{Q}$ can be written as:

(3)
$$\lambda \mathrm{D}Q_{ms}/\mathrm{D}t = (E_{ml} + \Omega_{ml})(\lambda Q_{ls} + \frac{\delta_{ls}}{d}) + (E_{sl} - \Omega_{sl})(\lambda Q_{ml} + \frac{\delta_{ml}}{d}) - 2E(\lambda Q_{ms} + \frac{\delta_{ms}}{d}).$$

It can be shown that $Q_{kl}v_{k,l} = E/\lambda$, hence,

$$(4)$$

$$\mathrm{D}Q_{ms}/\mathrm{D}t = (E_{ml} + \Omega_{ml})(\lambda Q_{ls} + \frac{\delta_{ls}}{d\lambda}) + (E_{sl} - \Omega_{sl})(\lambda Q_{ml} + \frac{\delta_{ml}}{d\lambda}) - 2Q_{kl}v_{k,l}(\lambda Q_{ms} + \frac{\delta_{ms}}{d}).$$

In addition to the terms derived above, it is also essential to include the relaxation to free energy term using the thermodynamics of the nematic liquid crystal and constructing the Beris-Edward model.

Appendix B

Governing equations of the solid phase

The solid part of the model is governed by the following equation:

$$\rho(\frac{\partial \vec{v}}{\partial t} + (\vec{v} \cdot \boldsymbol{\nabla})\vec{v}) = \boldsymbol{\nabla} \cdot \sigma_{\mathbf{s}}, \tag{5}$$

where σ_s denotes the Cauchy stress tensor and $\vec{v}$ represents the displacement vector. Assuming linear geometry and elastic material, Hookean tensor is defined as $\sigma_s = 2G\epsilon + (\kappa - \frac{2}{3}G)Tr[\epsilon]\mathbf{I}$, where G and κ stand for the shear and bulk modulus, respectively, and $\epsilon = \frac{1}{2}\left[\boldsymbol{\nabla}\vec{v} + (\boldsymbol{\nabla}\vec{v})^{\dagger}\right]$ is the displacement gradient tensor.

To solve the governing equations numerically, OpenFOAM is used along with the solids4foam toolbox (Cardiff, Karač, Jaeger, Jasak, Nagy, Ivanković & Tuković, 2018) which is responsible for the coupling of fluid part with solid part and perform the FSI analysis where both packages employ the FVM.

Utilizing the partitioned approach, the whole computational domain is decomposed into two regions (fluid and solid) using the Dirichlet-Neumann procedure. As such, fluid and solid models are solved separately. The velocity at the fluid-solid interface is used as boundary condition in the solution of fluid domain, while the solid part uses the exerted force by the fluid on the interface. Consequently, these two solutions are coupled by dynamic (continuity of force) and kinematic (continuity of displacement and velocity) conditions on the fluid-solid interface by Dirichlet-Neumann coupling scheme and utilizing the Aitken adaptive under-relaxation procedure (Tuković, Karač, Cardiff, Jasak & Ivanković, 2018).

BIBLIOGRAPHY

Abbasi, M. S., Song, R., Kim, H., & Lee, J. (2019). Multimodal breakup of a double emulsion droplet under an electric field. *Soft Matter*, *15*, 2292–2300.

Aditi Simha, R. & Ramaswamy, S. (2002). Hydrodynamic fluctuations and instabilities in ordered suspensions of self-propelled particles. *Phys. Rev. Lett.*, *89*, 058101.

Alert, R., Casademunt, J., & Joanny, J.-F. (2022). Active turbulence. *Annual Review of Condensed Matter Physics*, *13*(1), 143–170.

Alert, R., Joanny, J. F., & Casademunt, J. (2020a). Universal scaling of active nematic turbulence. *Nat. Phys.*, *16*, 682–688.

Alert, R., Joanny, J. F., & Casademunt, J. (2020b). Universal scaling of active nematic turbulence. *Nat. Phys.*, *16*, 682–688.

Allan, R. S., Mason, S. G., & Marion, L. E. (1962). Particle behaviour in shear and electric fields i. deformation and burst of fluid drops. *Proceedings of the Royal Society of London. Series A. Mathematical and Physical Sciences*, *267*(1328), 45–61.

Altun, E., Ekren, N., Kuruca, S. E., & Gunduz, O. (2019). Cell studies on electrohydrodynamic (ehd)-3d-bioprinted bacterial cellulose \polycaprolactone scaffolds for tissue engineering. *Materials Letters*, *234*, 163 – 167.

Amiri, A., Mueller, R., & Doostmohammadi, A. (2021). Half-integer and full-integer topological defects in polar active matter: Emergence, crossover, and coexistence.

Angelani, L., Di Leonardo, R., & Ruocco, G. (2009). Self-starting micromotors in a bacterial bath. *Phys. Rev. Lett.*, *102*, 048104.

Bartolo, D. & Aarts, D. G. (2012). Microfluidics and soft matter: small is useful. *Soft Matter*, *8*(41), 10530–10535.

Becco, C., Vandewalle, N., Delcourt, J., & Poncin, P. (2006). Experimental evidences of a structural and dynamical transition in fish school. *Physica A: Statistical Mechanics and its Applications*, *367*(C), 487–493.

Behjatian, A. & Esmaeeli, A. (2013). Electrohydrodynamics of a liquid column under a transverse electric field in confined domains. *International Journal of Multiphase Flow*, *48*, 71 – 81.

Beris, A. N. & Edwards, B. J. (1994). *Thermodynamics of Flowing Systems*. Oxford University Press.

Bialek, W., Cavagna, A., Giardina, I., Mora, T., Silvestri, E., Viale, M., & Walczak, A. M. (2012). Statistical mechanics for natural flocks of birds. *Proceedings of the National Academy of Sciences*, *109*(13), 4786–4791.

Blanch-Mercader, C. & Casademunt, J. (2017). Hydrodynamic instabilities, waves and turbulence in spreading epithelia. *Soft Matter*, *13*, 6913–6928.

Boffetta, G. & Ecke, R. E. (2012). Two-dimensional turbulence. *Annual Review of Fluid Mechanics*, *44*(1), 427–451.

Borthakur, M. P., Nath, B., & Biswas, G. (2021). Dynamics of a compound droplet under the combined influence of electric field and shear flow. *Phys. Rev. Fluids*, *6*, 023603.

Brackbill, J., Kothe, D., & Zemach, C. (1992). A continuum method for modeling surface tension. *Journal of Computational Physics*, *100*(2), 335 – 354.

Bratanov, V., Jenko, F., & Frey, E. (2015). New class of turbulence in active fluids. *PNAS*, *112*, 15048.

Bruijn, de, R. (1989). *Deformation and breakup of drops in simple shear flows*. PhD thesis, TUE, Department of Applied Physics.

Cardiff, P., Karač, A., Jaeger, P. D., Jasak, H., Nagy, J., Ivanković, A., & Tuković, (2018). An open-source finite volume toolbox for solid mechanics and fluid-solid interaction simulations.

Carenza, L. N., Gonnella, G., Lamura, A., Negro, G., & Tiribocchi, A. (2019). Lattice boltzmann methods and active fluids. *Eur. Phys. J. E*, *42*.

Castellanos, A. (1998). *Electrohydrodynamics*, volume 380. Springer Science & Business Media.

Chandra, R., Dagum, L., Kohr, D., Menon, R., Maydan, D., & McDonald, J. (2001). *Parallel programming in OpenMP*. Morgan kaufmann.

Chandragiri, S., Doostmohammadi, A., Yeomans, J. M., & Thampi, S. P. (2020). Flow states and transitions of an active nematic in a three-dimensional channel. *Phys. Rev. Lett.*, *125*, 148002.

Chatterjee, R., Rana, N., Simha, R. A., Perlekar, P., & Ramaswamy, S. (2021). Inertia drives a flocking phase transition in viscous active fluids. *Physical Review X*, *11*(3), 031063.

Chen, S., Tan, W. S., Bin Juhari, M. A., Shi, Q., Cheng, X. S., Chan, W. L., & Song, J. (2020). Freeform 3d printing of soft matters: recent advances in technology for biomedical engineering. *Biomedical Engineering Letters*, *10*(4), 453–479.

Chen, Y., Liu, X., & Shi, M. (2013). Hydrodynamics of double emulsion droplet in shear flow. *Applied Physics Letters*, *102*(5), 051609.

Chinyoka, T., Renardy, Y., Renardy, M., & Khismatullin, D. (2005). Two-dimensional study of drop deformation under simple shear for oldroyd-b liquids. *Journal of Non-Newtonian Fluid Mechanics*, *130*(1), 45 – 56.

Chorin, A. J. (1968). Numerical solution of the navier-stokes equations. *Mathematics of computation*, *22*(104), 745–762.

Colen, J., Han, M., Zhang, R., Redford, S. A., Lemma, L. M., Morgan, L., Ruijgrok, P. V., Adkins, R., Bryant, Z., Dogic, Z., Gardel, M. L., de Pablo, J. J., & Vitelli, V. (2021). Machine learning active-nematic hydrodynamics. *Proceedings of the National Academy of Sciences*, *118*(10), e2016708118.

Courant, R., Friedrichs, K., & Lewy, H. (1928). Über die partiellen differenzengleichungen der mathematischen physik. *Mathematische annalen*, *100*(1), 32–74.

Cummins, S. J. & Rudman, M. (1999). An sph projection method. *Journal of computational physics*, *152*(2), 584–607.

Dai, Z., Wang, F., Huang, Y., Song, K., & Iio, A. (2016). Sph-based numerical modeling for the post-failure behavior of the landslides triggered by the 2016 kumamoto earthquake. *Geoenvironmental Disasters*, *3*(1), 1–14.

Das, D. & Saintillan, D. (2021). A three-dimensional small-deformation theory for electrohydrodynamics of dielectric drops. *Journal of Fluid Mechanics*, *914*, A22.

De Gennes, P.-G. & Prost, J. (1995). *The physics of liquid crystals*. Oxford university press.

Deshpande, S. S., Anumolu, L., & Trujillo, M. F. (2012). Evaluating the performance of the two-phase flow solver interFoam. *Computational science & discovery*, *5*(1), 014016.

Dhariwala, B., Hunt, E., & Boland, T. (2004). Rapid prototyping of tissue-engineering constructs, using photopolymerizable hydrogels and stereolithography. *Tissue engineering*, *10*(9-10), 1316–1322.

Doostmohammadi, A., Ignés-Mullol, J., Yeomans, J. M., & Sagués, F. (2018). Active nematics. *Nat. Commun.*, *9*(1), 3246.

Doostmohammadi, A. & Ladoux, B. (2022). Physics of liquid crystals in cell biology. *Trends in Cell Biology*, *32*(2), 140–150.

Doostmohammadi, A., Shendruk, T. N., Thijssen, K., & Yeomans, J. M. (2017). Onset of meso-scale turbulence in active nematics. *Nature communications*, *8*(1), 1–7.

Doostmohammadi, A., Thampi, S. P., Saw, T. B., Lim, C. T., Ladoux, B., & Yeomans, J. M. (2015). Celebrating Soft Matter's 10th anniversary: Cell division: a source of active stress in cellular monolayers. *Soft Matter*, *11*, 7328.

Duclos, G., Adkins, R., Banerjee, D., Peterson, M. S. E., Varghese, M., Kolvin, I., Baskaran, A., Pelcovits, R. A., Powers, T. R., Baskaran, A., Toschi, F., Hagan, M. F., Streichan, S. J., Vitelli, V., Beller, D. A., & Dogic, Z. (2020). Topological structure and dynamics of three-dimensional active nematics. *Science*, *367*(6482), 1120–1124.

Edwards, S. A. & Yeomans, J. M. (2009). Spontaneous flow states in active nematics: A unified picture. *EPL (Europhysics Letters)*, *85*(1), 18008.

Elvin, N., Elvin, A., & Senderos, B. Z. (2018). Capacitance changes in thin piezoelectric transducers embedded in isotropic host materials. *Journal of Intelligent Material Systems and Structures*, *29*(5), 816–829.

Eringen, A. C. (1980). *Mechanics of continua /2nd edition/.*

Eringen, A. C. & Maugin, G. A. (2012). *Electrodynamics of continua II: fluids and complex media.* Springer Science & Business Media.

Esmaeeli, A. & Behjatian, A. (2012). Electrohydrodynamics of a liquid drop in confined domains. *Phys. Rev. E*, *86*, 036310.

Fang, J., Varbanescu, A. L., & Sips, H. (2011). A comprehensive performance comparison of cuda and opencl. In *2011 International Conference on Parallel Processing*, (pp. 216–225).

Feng, J. Q. & Scott, T. C. (1996). A computational analysis of electrohydrodynamics of a leaky dielectric drop in an electric field. *Journal of Fluid Mechanics*, *311*, 289–326.

Feng, S., Shirani, E., & Inglis, D. W. (2019). Droplets for sampling and transport of chemical signals in biosensing: a review. *Biosensors*, *9*(2), 80.

Ferziger, J. H., Perić, M., & Street, R. L. (2002). *Computational methods for fluid dynamics*, volume 3. Springer.

Fielding, S. M., Marenduzzo, D., & Cates, M. E. (2011). Nonlinear dynamics and rheology of active fluids: Simulations in two dimensions. *Phys. Rev. E*, *83*, 041910.

Fink, G., Hamidović, M., Springer, A., Wille, R., & Haselmayr, W. (2020). Design and realization of flexible droplet-based lab-on-a-chip devices. *Elektrotech. Informationstech*, *137*, 1–8.

Friedel, G. (1922). Les états mésomorphes de la matière. In *Annales de physique*, volume 9, (pp. 273–474).

Frishman, A. & Keren, K. (2021). Learning active nematics one step at a time. *Proceedings of the National Academy of Sciences*, *118*(12), e2102169118.

Funfschilling, D., Debas, H., Li, H.-Z., & Mason, T. G. (2009). Flow-field dynamics during droplet formation by dripping in hydrodynamic-focusing microfluidics. *Phys. Rev. E*, *80*, 015301.

Gallet, B. & Young, W. R. (2013). A two-dimensional vortex condensate at high reynolds number. *Journal of Fluid Mechanics*, *715*, 359–388.

Gao, T., Blackwell, R., Glaser, M. A., Betterton, M. D., & Shelley, M. J. (2015). Multiscale modeling and simulation of microtubule–motor-protein assemblies. *Phys. Rev. E*, *92*, 062709.

Ghazanfarian, J., Saghatchi, R., & Gorji-Bandpy, M. (2015). Turbulent fluid-structure interaction of water-entry/exit of a rotating circular cylinder using sph method. *International Journal of Modern Physics C*, *26*(08), 1550088.

Ghazanfarian, J., Saghatchi, R., & Gorji-Bandpy, M. (2016). Sph simulation of turbulent flow past a high-frequency in-line oscillating cylinder near free-surface. *International Journal of Modern Physics C*, *27*(12), 1650152.

Gingold, R. A. & Monaghan, J. J. (1977). Smoothed particle hydrodynamics: theory and application to non-spherical stars. *Monthly notices of the royal astronomical society*, *181*(3), 375–389.

Giomi, L. (2015). Geometry and topology of turbulence in active nematics. *Phys. Rev. X*, *5*, 031003.

Green, S. (2007). CUDA Particles. *NVIDIA Whitepaper*, (June).

Gropp, W., Lusk, E., & Skjellum, A. (1999). *Using MPI: portable parallel programming with the message-passing interface*, volume 1. MIT press.

Group, K. O. W. et al. (2008). The opencl specification. *Version*, *1*(29), 8.

Hamel, A., Fisch, C., Combettes, L., Dupuis-Williams, P., & Baroud, C. N. (2011). Transitions between three swimming gaits in paramecium escape. *Proceedings of the National Academy of Sciences*, *108*(18), 7290–7295.

Hardoüin, J., Hughes, R., Doostmohammadi, A., Laurent, J., Lopez-Leon, T., Yeomans, J. M., Ignés-Mullol, J., & Sagués, F. (2019). Reconfigurable flows and defect landscape of confined active nematics. *Communications Physics*, *2*(1), 1–9.

Hemingway, E. J., Mishra, P., Marchetti, M. C., & Fielding, S. M. (2016). Correlation lengths in hydrodynamic models of active nematics. *Soft Matter*, *12*, 7943–7952.

Henkin, G., DeCamp, S. J., Chen, D. T. N., Sanchez, T., & Dogic, Z. (2014). Tunable dynamics of microtubule-based active isotropic gels. *Philosophical Transactions of the Royal Society A: Mathematical, Physical and Engineering Sciences*, *372*(2029), 20140142.

Houghton, I. A., Koseff, J. R., Monismith, S. G., & Dabiri, J. O. (2018). Vertically migrating swimmers generate aggregation-scale eddies in a stratified column. *Nat.*, *556*(7702), 497–500.

Hua, H., Shin, J., & Kim, J. (2014). Dynamics of a compound droplet in shear flow. *International Journal of Heat and Fluid Flow*, *50*, 63 – 71.

Hudson, S. D. (2010). Poiseuille flow and drop circulation in microchannels. *Rheologica acta*, *49*(3), 237–243.

Hunt, T. P., Issadore, D., Brown, K. A., Lee, H., & Westervelt, R. M. (2009). *Integrated circuit/microfluidic chips for dielectric manipulation.* Caister Academic

Press.

Katija, K. & Dabiri, J. O. (2009). A viscosity-enhanced mechanism for biogenic ocean mixing. *Nature*, *460*(7255), 624–626.

Kawaguchi, K., Kageyama, R., & Sano, M. (2017). Topological defects control collective dynamics in neural progenitor cell cultures. *Nature*, *545*, 327–331.

Khair, A. S. & Chisholm, N. G. (2014). Expansions at small reynolds numbers for the locomotion of a spherical squirmer. *Physics of Fluids*, *26*(1), 011902.

Klotsa, D. (2019). As above, so below, and also in between: mesoscale active matter in fluids. *Soft matter*, *15*(44), 8946–8950.

Koch, C.-M. & Wilczek, M. (2021). Role of advective inertia in active nematic turbulence. *Physical Review Letters*, *127*(26), 268005.

Kokot, G., Das, S., Winkler, R. G., Gompper, G., Aranson, I. S., & Snezhko, A. (2017). Active turbulence in a gas of self-assembled spinners. *Proceedings of the National Academy of Sciences*, *114*(49), 12870–12875.

Kolmogorov, A. N., Levin, V., Hunt, J. C. R., Phillips, O. M., & Williams, D. (1991). The local structure of turbulence in incompressible viscous fluid for very large reynolds numbers. *Proceedings of the Royal Society of London. Series A: Mathematical and Physical Sciences*, *434*(1890), 9–13.

Krajnik, Ž., Kos, Ž., & Ravnik, M. (2020). Spectral energy analysis of bulk three-dimensional active nematic turbulence. *Soft Matter*, *16*, 9059–9068.

Kupershtokh, A. & Medvedev, D. (2006). Lattice boltzmann equation method in electrohydrodynamic problems. *Journal of Electrostatics*, *64*(7), 581 – 585. Fifth International Electrohydrodynamics (EHD) Workshop and Fourth Conference of the Société Française d'Electrostatique (SFE).

Lauga, E. & Powers, T. R. (2009). The hydrodynamics of swimming microorganisms. *Reports on Progress in Physics*, *72*(9), 096601.

Lauricella, M., Melchionna, S., Montessori, A., Pisignano, D., Pontrelli, G., & Succi, S. (2018). Entropic lattice boltzmann model for charged leaky dielectric multiphase fluids in electrified jets. *Phys. Rev. E*, *97*, 033308.

Lee, C.-Y., Chang, C.-L., Wang, Y.-N., & Fu, L.-M. (2011). Microfluidic mixing: A review. *International Journal of Molecular Sciences*, *12*(5), 3263–3287.

Lighthill, M. J. (1952). On the squirming motion of nearly spherical deformable bodies through liquids at very small reynolds numbers. *Communications on Pure and Applied Mathematics*, *5*(2), 109–118.

Linkmann, M., Boffetta, G., Marchetti, M. C., & Eckhardt, B. (2019). Phase transition to large scale coherent structures in two-dimensional active matter turbulence. *Physical review letters*, *122*(21), 214503.

Linkmann, M., Marchetti, M. C., Boffetta, G., & Eckhardt, B. (2020). Condensate formation and multiscale dynamics in two-dimensional active suspensions. *Phys. Rev. E*, *101*, 022609.

Liu, J., Tian, L., Qiao, Y., Zhou, S., Patil, A. J., Wang, K., Li, M., & Mann, S. (2020). Hydrogel-immobilized coacervate droplets as modular microreactor assemblies. *Angewandte Chemie International Edition*, *59*(17), 6853–6859.

Löwen, H. (2020). Inertial effects of self-propelled particles: From active brownian to active langevin motion. *The Journal of chemical physics*, *152*(4), 040901.

Lucy, L. B. (1977). A numerical approach to the testing of the fission hypothesis. *The astronomical journal*, *82*, 1013–1024.

Luo, Z. Y., He, L., & Bai, B. F. (2015). Deformation of spherical compound capsules in simple shear flow. *Journal of Fluid Mechanics*, *775*, 77–104.

Majidi, C. (2019). Soft-matter engineering for soft robotics. *Advanced Materials Technologies*, *4*(2), 1800477.

Marchetti, M. C., Joanny, J. F., Ramaswamy, S., Liverpool, T. B., Prost, J., Rao, M., & Simha, R. A. (2013). Hydrodynamics of soft active matter. *Rev. Mod. Phys.*, *85*, 1143–1189.

Marenduzzo, D., Orlandini, E., Cates, M. E., & Yeomans, J. M. (2007a). Steady-state hydrodynamic instabilities of active liquid crystals: Hybrid lattice boltzmann simulations. *Phys. Rev. E*, *76*, 031921.

Marenduzzo, D., Orlandini, E., Cates, M. E., & Yeomans, J. M. (2007b). Steady-state hydrodynamic instabilities of active liquid crystals: Hybrid lattice boltzmann simulations. *Phys. Rev. E*, *76*, 031921.

Maroudas-Sacks, Y., Garion, L., Shani-Zerbib, L., Livshits, A., Braun, E., & Keren, K. (2021). Topological defects in the nematic order of actin fibres as organization centres of hydra morphogenesis. *Nature Physics*, *17*(2), 251–259.

Martínez-Prat, B., Alert, R., Meng, F., Ignés-Mullol, J., Joanny, J.-F., Casademunt, J., Golestanian, R., & Sagués, F. (2021). Scaling regimes of active turbulence with external dissipation. *Physical Review X*, *11*(3), 031065.

Martínez-Prat, B., Ignés-Mullol, J., Casademunt, J., & Sagués, F. (2019). Selection mechanism at the onset of active turbulence. *Nature Physics*, *15*(4), 362–366.

Meacock, O. J., Doostmohammadi, A., Foster, K. R., Yeomans, J. M., & Durham, W. M. (2021). Bacteria solve the problem of crowding by moving slowly. *Nature Physics*, *17*(2), 205–210.

Mitov, M. (2014). Liquid-crystal science from 1888 to 1922: Building a revolution. *ChemPhysChem*, *15*(7), 1245–1250.

Mohammadi, K., Movahhedy, M. R., & Khodaygan, S. (2019). A multiphysics model for analysis of droplet formation in electrohydrodynamic 3d printing process. *Journal of Aerosol Science*, *135*, 72 – 85.

Moin, P. (2010). *Fundamentals of engineering numerical analysis*. Cambridge University Press.

Monaghan, J. J. (1994). Simulating free surface flows with sph. *Journal of computational physics*, *110*(2), 399–406.

Morris, J. P. (2000). Simulating surface tension with smoothed particle hydrodynamics. *International Journal of Numerical Methods in Fluids*, *33*(3), 333–353.

Morris, J. P., Fox, P. J., & Zhu, Y. (1997). Modeling low reynolds number incompressible flows using sph. *Journal of Computational Physics*, *136*(1), 214–226.

Moukalled, F., Mangani, L., Darwish, M., et al. (2016). *The finite volume method in computational fluid dynamics*, volume 113. Springer.

Mählmann, S. & Papageorgiou, D. T. (2009). Numerical study of electric field effects on the deformation of two-dimensional liquid drops in simple shear flow at arbitrary reynolds number. *Journal of Fluid Mechanics*, *626*, 367–393.

Nejad, M. R., Doostmohammadi, A., & Yeomans, J. M. (2021). Memory effects, arches and polar defect ordering at the cross-over from wet to dry active nematics. *Soft Matter*, *17*, 2500–2511.

Opalski, A. S., Makuch, K., Derzsi, L., & Garstecki, P. (2020). Split or slip – passive generation of monodisperse double emulsions with cores of varying viscosity in microfluidic tandem step emulsification system. *RSC Adv.*, *10*, 23058–23065.

OpenFOAM, C. (2011). Openfoam programmer's guide. *OpenFOAM Foundation*, *2*(0).

Ozbulut, M., Ramezanzadeh, S., Yildiz, M., & Goren, O. (2020). Modelling of wave generation in a numerical tank by SPH method. *Journal of Ocean Engineering and Marine Energy*, *6*(2), 121–136.

Ozbulut, M., Tofighi, N., Goren, O., & Yildiz, M. (2017). Investigation of Wave Characteristics in Oscillatory Motion of Partially Filled Rectangular Tanks. *Journal of Fluids Engineering*, *140*(4).

Ozbulut, M., Yildiz, M., & Goren, O. (2014a). A numerical investigation into the correction algorithms for sph method in modeling violent free surface flows. *International Journal of Mechanical Sciences*, *79*, 56 – 65.

Ozbulut, M., Yildiz, M., & Goren, O. (2014b). A numerical investigation into the correction algorithms for sph method in modeling violent free surface flows. *International Journal of Mechanical Sciences*, *79*, 56–65.

Pacheco, P. (1997). *Parallel programming with MPI*. Morgan Kaufmann.

Pang, Y., Zhou, Q., Wang, X., Lei, Y., Ren, Y., Li, M., Wang, J., & Liu, Z. (2020). Droplets generation under different flow rates in t-junction microchannel with a neck. *AIChE Journal*, *66*(10), e16290.

Paoluzzi, M., Di Leonardo, R., Marchetti, M. C., & Angelani, L. (2016). Shape and displacement fluctuations in soft vesicles filled by active particles. *Scientific reports*, *6*(1), 1–10.

Patankar, S. V. (2018). *Numerical heat transfer and fluid flow*. CRC press.

Paximada, P., Howarth, M., & Dubey, B. N. (2021). Double emulsions fortified with plant and milk proteins as fat replacers in cheese. *Journal of Food Engineering*, *288*, 110229.

Plan, E. L. C. V. M., Yeomans, J. M., & Doostmohammadi, A. (2021). Activity pulses induce spontaneous flow reversals in viscoelastic environments. *Journal of The Royal Society Interface*, *18*(177), 20210100.

Pontrelli, G., Carr, E. J., Tiribocchi, A., & Succi, S. (2020). Modeling drug delivery from multiple emulsions. *Phys. Rev. E*, *102*, 023114.

Pope, S. B. & Pope, S. B. (2000). *Turbulent flows*. Cambridge university press.

Prost, J., Jülicher, F., & Joanny, J. F. (2015). Active gel physics. *Nat. Phys.*, *11*, 111–117.

Raghuraman, B., Tirmizi, N., & Wiencek, J. (1994). Emulsion liquid membranes for wastewater treatment: Equilibrium models for some typical metal-extractant systems. *Environmental Science & Technology*, *28*(6), 1090–1098. PMID: 22176234.

Ramaswamy, S. (2010a). The mechanics and statistics of active matter. *Annl. Rev. Cond. Mat. Phys.*, *1*, 323–345.

Ramaswamy, S. (2010b). The mechanics and statistics of active matter. *Annual Review of Condensed Matter Physics*, *1*(1), 323–345.

Rao, S. S. (2011). Mechanical vibrations.[sl].

Reich, F. A., Rickert, W., & Müller, W. H. (2018). An investigation into electromagnetic force models: differences in global and local effects demonstrated by selected problems. *Continuum Mechanics and Thermodynamics*, *30*, 233–266.

Reinitzer, F. (1888). Beiträge zur kenntniss des cholesterins. *Monatshefte für Chemie und verwandte Teile anderer Wissenschaften*, *9*(1), 421–441.

Riley, E. E., Das, D., & Lauga, E. (2018). Swimming of peritrichous bacteria is enabled by an elastohydrodynamic instability. *Scientific reports*, *8*(1), 1–7.

Roghair, I., Musterd, M., van den Ende, D., Kleijn, C., Kreutzer, M., & Mugele, F. (2015). A numerical technique to simulate display pixels based on electrowetting. *Microfluidics and Nanofluidics*, *19*(2), 465 – 482.

Saghatchi, R., Ghazanfarian, J., & Gorji-Bandpy, M. (2014). Numerical Simulation of Water-Entry and Sedimentation of an Elliptic Cylinder Using Smoothed-Particle Hydrodynamics Method. *Journal of Offshore Mechanics and Arctic Engineering*, *136*(3).

Saintillan, D. (2018). Rheology of active fluids. *Annual Review of Fluid Mechanics*, *50*(1), 563–592.

Sanchez, T., Chen, D. T., DeCamp, S. J., Heymann, M., & Dogic, Z. (2012). Spontaneous motion in hierarchically assembled active matter. *Nature*, *491*(7424), 431–434.

Sanders, J. & Kandrot, E. (2010). *CUDA by example: an introduction to general-purpose GPU programming.* Addison-Wesley Professional.

Santhosh, S., Nejad, M. R., Doostmohammadi, A., Yeomans, J. M., & Thampi, S. P. (2020a). Activity induced nematic order in isotropic liquid crystals. *Journal of Statistical Physics*, *180*(1), 699–709.

Santhosh, S., Nejad, M. R., Doostmohammadi, A., Yeomans, J. M., & Thampi, S. P. (2020b). Activity induced nematic order in isotropic liquid crystals. *Journal of Statistical Physics*, *180*(1), 699–709.

Santra, S., Das, S., & Chakraborty, S. (2020). Electrically modulated dynamics of a compound droplet in a confined microfluidic environment. *Journal of Fluid Mechanics*, *882*, A23.

Santra, S., Jana, A., & Chakraborty, S. (2020). Electric field modulated deformation dynamics of a compound drop in the presence of confined shear flow. *Physics of Fluids*, *32*(12), 122006.

Santra, S., Mandal, S., & Chakraborty, S. (2018). Electrohydrodynamics of confined two-dimensional liquid droplets in uniform electric field. *Physics of Fluids*, *30*(6), 062003.

Saville, D. A. (1997). Electrohydrodynamics: The taylor-melcher leaky dielectric model. *Annual Review of Fluid Mechanics*, *29*(1), 27–64.

Saw, T. B., Doostmohammadi, A., Nier, V., Kocgozlu, L., Thampi, S., Toyama, Y., Marcq, P., Lim, C. T., Yeomans, J. M., & Ladoux, B. (2017). Topological defects in epithelia govern cell death and extrusion. *Nature*, *544*, 212–216.

Scholz, C., Jahanshahi, S., Ldov, A., & Löwen, H. (2018). Inertial delay of self-propelled particles. *Nature communications*, *9*(1), 1–9.

Shadloo, M. S., Rahmat, A., & Yildiz, M. (2013). A smoothed particle hydrodynamics study on the electrohydrodynamic deformation of a droplet suspended in a neutrally buoyant newtonian fluid. *Computational Mechanics*, *52*(3), 693–707.

Shadloo, M. S., Zainali, A., Sadek, S. H., & Yildiz, M. (2011). Improved incompressible smoothed particle hydrodynamics method for simulating flow around bluff bodies. *Computer Methods in Applied Mechanics and Engineering*, *200*(9), 1008–1020.

Shendruk, T. N., Doostmohammadi, A., Thijssen, K., & Yeomans, J. M. (2017). Dancing disclinations in confined active nematics. *Soft Matter*, *13*, 3853–3862.

Sheth, K. S. & Pozrikidis, C. (1995). Effects of inertia on the deformation of liquid drops in simple shear flow. *Computers & Fluids*, *24*(2), 101 – 119.

Simha, R. A. & Ramaswamy, S. (2002). Hydrodynamic fluctuations and instabilities in ordered suspensions of self-propelled particles. *Physical review letters*, *89*(5), 058101.

Smith, S. W. et al. (1997). *The scientist and engineer's guide to digital signal processing*. California Technical Pub. San Diego, California.

Song, Y. & Shum, H. C. (2012). Monodisperse w/w/w double emulsion induced by phase separation. *Langmuir*, *28*(33), 12054–12059. PMID: 22849828.

Spasic, A. M., Jovanovic, J. M., Manojlovic, V., & Jovanovic, M. (2016). Breaking of double emulsions based on electrohydrodynamics principles. *Journal of Colloid and Interface Science*, *479*, 165 – 172.

Tarnowska, M., Briançon, S., Resende de Azevedo, J., Chevalier, Y., Arquier, D., Barratier, C., & Bolzinger, M.-A. (2020). The effect of vehicle on skin absorption of mg2+ and ca2+ from thermal spring water. *International Journal of Cosmetic Science*, *42*(3), 248–258.

Taylor, G. I. (1964). Disintegration of water drops in an electric field. *Proceedings of the Royal Society of London. Series A. Mathematical and Physical Sciences*, *280*(1382), 383–397.

Taylor, G. I., McEwan, A. D., & de Jong, L. N. J. (1966). Studies in electrohydrodynamics. i. the circulation produced in a drop by an electric field. *Proceedings of the Royal Society of London. Series A. Mathematical and Physical Sciences*, *291*(1425), 159–166.

Thampi, S. & Yeomans, J. (2016). Active turbulence in active nematics. *The European Physical Journal Special Topics*, *225*(4), 651–662.

Thampi, S. P., Doostmohammadi, A., Golestanian, R., & Yeomans, J. M. (2015). Intrinsic free energy in active nematics. *EPL (Europhysics Letters)*, *112*(2), 28004.

Thampi, S. P., Golestanian, R., & Yeomans, J. M. (2013). Velocity correlations in an active nematic. *Phys. Rev. Lett.*, *111*, 118101.

Thampi, S. P., Golestanian, R., & Yeomans, J. M. (2014a). Instabilities and topological defects in active nematics. *EPL (Europhysics Letters)*, *105*(1), 18001.

Thampi, S. P., Golestanian, R., & Yeomans, J. M. (2014b). Vorticity, defects and correlations in active turbulence. *Philosophical Transactions of the Royal Society A: Mathematical, Physical and Engineering Sciences*, *372*(2029), 20130366.

Thijssen, K., Metselaar, L., Yeomans, J. M., & Doostmohammadi, A. (2020). Active nematics with anisotropic friction: the decisive role of the flow aligning parameter. *Soft Matter*, *16*, 2065–2074.

Tofighi, N. & Yildiz, M. (2013). Numerical simulation of single droplet dynamics in three-phase flows using ISPH. *Computers and Mathematics with Applications*, *66*(4), 525–536.

Tsukada, T., Mayama, J., Sato, M., & Hozawa, M. (1997). Theoretical and experimental studies on the behavior of a compound drop under a uniform dc electric field. *Journal of Chemical Engineering of Japan*, *30*(2), 215–222.

Tsukada, T., Yamamoto, Y., Katayama, T., & Hozawa, M. (1994). Effect of an electric field on the behavior of a drop moving in a quiescent liquid. *Journal of Chemical Engineering of Japan*, *27*(5), 662–666.

Tuković, Ž., Karač, A., Cardiff, P., Jasak, H., & Ivanković, A. (2018). Openfoam finite volume solver for fluid-solid interaction. *Transactions of FAMENA*, *42*(3), 1–31.

Turiv, T., Krieger, J., Babakhanova, G., Yu, H., Shiyanovskii, S. V., Wei, Q.-

H., Kim, M.-H., & Lavrentovich, O. D. (2020). Topology control of human fibroblast cells monolayer by liquid crystal elastomer. *Science Advances*, *6*(20), eaaz6485.

Ubbink, O. & Issa, R. (1999). A method for capturing sharp fluid interfaces on arbitrary meshes. *Journal of Computational Physics*, *153*(1), 26–50.

Urzay, J., Doostmohammadi, A., & Yeomans, J. M. (2017). Multi-scale statistics of turbulence motorized by active matter. *J. Fluid Mech.*, *822*, 762.

van Duren, L. A. & Videler, J. J. (2003). Escape from viscosity: the kinematics and hydrodynamics of copepod foraging and escape swimming. *Journal of Experimental Biology*, *206*(2), 269–279.

Versteeg, H. K. & Malalasekera, W. (2007). *An introduction to computational fluid dynamics*. Pearson education.

Vink, R. L. C. (2014). Crossover from a kosterlitz-thouless phase transition to a discontinuous phase transition in two-dimensional liquid crystals. *Phys. Rev. E*, *90*, 062132.

Wang, S. & Ardekani, A. (2012). Inertial squirmer. *Physics of Fluids*, *24*(10), 101902.

Weller, H. G., Tabor, G., Jasak, H., & Fureby, C. (1998). A tensorial approach to computational continuum mechanics using object-oriented techniques. *Computers in Physics*, *12*(6), 620–631.

Wensink, H. H., Dunkel, J., Heidenreich, S., Drescher, K., Goldstein, R. E., Löwen, H., & Yeomans, J. M. (2012). Meso-scale turbulence in living fluids. *PNAS*, *109*, 14308–14313.

Wu, J.-C., Lv, K., Zhao, W.-W., & Ai, B.-Q. (2018). Transport of active particles induced by wedge-shaped barriers in straight channels with hard and soft walls. *Chaos: An Interdisciplinary Journal of Nonlinear Science*, *28*(12), 123102.

Xia, Y. (2019). Electrohydrodynamic droplet injection method into model oil. *AIP Advances*, *9*(10), 105309.

Yang, C.-G., Xu, Z.-R., & Wang, J.-H. (2010). Manipulation of droplets in microfluidic systems. *TrAC Trends in Analytical Chemistry*, *29*(2), 141–157.

Zainali, A., Tofighi, N., Shadloo, M., & Yildiz, M. (2013a). Numerical investigation of newtonian and non-newtonian multiphase flows using isph method. *Computer Methods in Applied Mechanics and Engineering*, *254*, 99 – 113.

Zainali, A., Tofighi, N., Shadloo, M., & Yildiz, M. (2013b). Numerical investigation of newtonian and non-newtonian multiphase flows using isph method. *Computer Methods in Applied Mechanics and Engineering*, *254*, 99–113.

Zanini, L., Zaltron, A., Turato, E., Zamboni, R., & Sada, C. (2022). Opto-microfluidic integration of the bradford protein assay in lithium niobate lab-on-a-chip. *Sensors*, *22*(3).

Zhang, J. & Kwok, D. Y. (2005). A 2d lattice boltzmann study on electrohydrodynamic drop deformation with the leaky dielectric theory. *Journal of Computational Physics*, *206*(1), 150 – 161.